Probing The Dynamics of Biomolecules Using EPR Spectroscopy and Electron Spin Labels

Shutian Lu

A dissertation

submitted in partial fulfillment of the

requirements for the degree of

Doctor of Philosophy

University of Washington

2023

Reading Committee:

Stefan Stoll, Chair

Anne B. McCoy

Bruce H. Robinson

Program Authorized to Offer Degree:

Chemistry

University of Washington

Abstract

Probing The Dynamics of Biomolecules Using EPR Spectroscopy and Electron Spin Labels

Shutian Lu

Chair of the Supervisory Committee:
Stefan Stoll
Department of Chemistry

This thesis presents two applications of using electron spin probes along with electron paramagnetic resonance (EPR) spectroscopy experiments for studying the dynamics of biological molecules in different motion regimes. Chapter 1 introduces the physical origin of the magnetic signal originated from the spin probes. Chapter 2 presents a novel solution-state EPR assay developed using spin-labeled nucleic acid aptamers. The assay was demonstrated by measuring and fitting the spin label mobility change upon protein–aptamer binding, followed by a discussion of integrating this assay with diamond nitrogen vacancy centers for a potential quantum protein sensor. Chapter 3 presents an instrumentation project, in which a customized rapid freeze-quench (RFQ) device was constructed for discover the temporal resolution of maltose binding protein conformational change along with double electron-electron resonance (DEER) spectroscopy.

DEDICATION

匆匆美梦奈何天

TABLE OF CONTENTS

LIST OF ABBREVIATIONS

CW : Continuous Wave

DEER : Double Electron Electron Resonance

EPR : Electron Paramagnetic Resonance

MBP : Maltose Binding Protein

RFQ : Rapid Freeze Quench

SDSL : Site-Directed Spin Labeling

SOMAmer : Slow Off-rate Modified Aptamer

TEMPO : 2,2,6,6-Tetramethyl-piperidin-1-oxyl

ACKNOWLEDGMENTS

First, I would like to thank my advisor Stefan Stoll for all the training and science experience I received in the past five years. I would also like to thank my committee members–Professor Anne McCoy, Professor Bruce Robinson and Professor Kai-Mei Fu for their time and attention. I would also like to acknowledge my collaborators from SomaLogic: Catherine R. Fowler, Brian Ream, Sheela M. Waugh, Theresa M. Russell, John C. Rohloff, Larry Gold, Jason P. Cleveland for providing all the materials and discussion.

I could not make through the program without my fellow group mates: Dr. Donald Mannikko, Dr. Lizzy Canarie, Dr. Sarah Sweger and Rachelle Stowell. I will cherish the memory of each one of you and carry it with me. I would also like to give special thanks to two postdoctoral researchers, Dr. Maxx H. Tessmer and Dr. Eric G. B. Evans. My graduate school experience would have been different without the training and inspirations from these two excellent scientists. I would also acknowledge the support from these great scholars–Dr. Jaekyun Jeon, Dr. Thomas Schmidt and Dr. Maria Oranges for discussions on constructing the RFQ device as well as Professor William Atkins, Dr. Michelle Redhair and King Yabut for sharing the stopped-flow instrument.

Lastly, I would like to acknowledge staff members from the Department of Chemistry: Loch Hickok from the stockroom, Bill Beaty, Rachael Huffman, and Kit Sczudlo from the electronic shop, and Brian Wadey and Kevin Soderlund from the machine shop, as well as Diana Knight, Leesa Kurtz, Angela Mullen, Christine Gormley from the administrative office for their help and dedications.

Chapter 1

MAGNETIC PROBES AND EPR EXPERIMENTS

Electron paramagnetic resonance is a powerful and versatile technique. Along side with electron spin labels, the instrument can be used for probing a variety of molecular systems that are interacting on different timescales. This chapter serves as an introduction to spin labels and their magnetic interactions, as well as the background information of EPR experiments. Section 1.1 introduces nitroxide spin labels and their effective Hamiltonian. Section 1.2 discusses the theory underlying solution-state nitroxide lineshape analysis, which is used for data analysis in the project presented in Chapter 2. Section 1.3 is focused on a double electron–electron resonance (DEER) experiment for an application presented in Chapter 3.

1.1 Nitroxide spin labels and their magnetic interactions

Proteins perform critical functions in many biological processes including controlling movement, catalyzing biochemical reactions, and signal transduction. They can also be used as biomarkers for evaluating physiological conditions. Decades of bioengineering studies have developed numerous molecular probes to provide means for direct measurements of biochemical interactions. Electron spin probes or spin labels are one of these probes and can be used for resolve the dynamics of protein structural conversion along with EPR spectroscopy. Several types of spin labels have been developed for different EPR experiments or experiments at different microwave frequencies. The most popular ones include Cu(II) complexes, Gd(III) complex and nitroxide spin labels. In this thesis, the discussion is focused on nitroxide spin labels only.

Nitroxide spin labels are small organic molecules with an unpaired electron residing in the bond between the oxygen and the nitrogen atom. The unpaired electron is often protected by

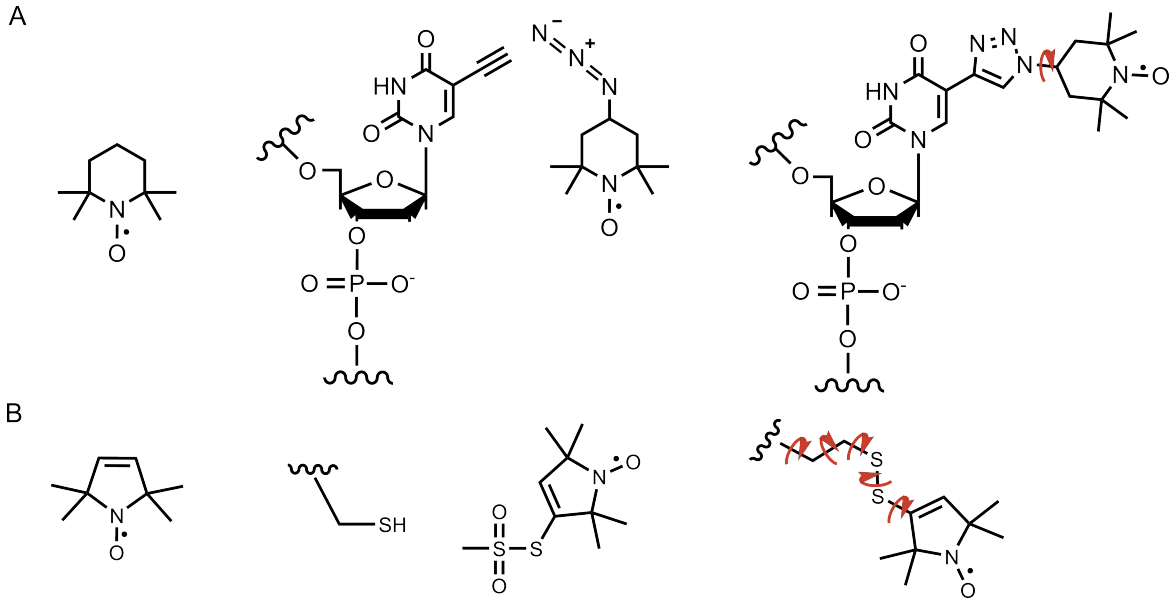

Figure 1.1: Commonly used nitroxides labels and labeling chemistry. A. Left: TEMPO, or (2,2,6,6-tetramethylpiperidin-1-oxyl. Middle: coupling reaction between 4-azido functionalized TEMPO and alkyne–modified uridine. The addition is usually catalyzed by Cu(I).[1] Right: TEMPO-labeled uridine. Red arrow indicates the rotatable bond. B. Left: Pyrroline. Middle: coupling reaction between a cysteine residue and MTSL (1-oxyl-2,2,5,5-tetramethyl-Δ3-pyrroline-3-methyl) methanethiosulfonate. Right: R1 side chain on a peptide backbone with five rotatable bonds.

methyl groups on the carbons adjacent to the nitrogen atom. Nitroxide spin labels are often designed with a functional group for reacting with its counterpart on a protein or a nucleic acid. Two selected examples[61, 119] are shown in Fig. 1.1. Such spin labels can be conjugated to biomoleucules at precise locations with carefully designed mutations in amino acid sequence or nucleic acid sequence. The method is referred to as site-directed spin labeling (SDSL) and has been widely adopted in the community of protein structural studies.

The unpaired electron in the nitroxide makes the molecule a magnetic probe. Electrons are charged particles with an intrinsic spin angular momentum, denoted as $\hat{\boldsymbol{S}}$. Analogous to a rotating point charge, the spin angular momentum generates a magnetic dipole moment $\hat{\boldsymbol{\mu}}$.

The dipole moment and spin angular momentum of an electron are related by

$$\hat{\boldsymbol{\mu}} = -\mu_{\mathrm{B}} \mathrm{g_e} \hat{\mathbf{S}}, \tag{1.1}$$

where μ_{B} is the Bohr magneton, $\mathrm{g_e}$ is a dimensionless factor known as the electron g_{e}-value and $\hat{\boldsymbol{S}}$ is the spin angular momentum vector operator containing $\hat{S}_x$, $\hat{S}_y$ and $\hat{S}_z$. When unpaired electrons are placed in an external magnetic field, often denoted as $\boldsymbol{B}_0$, the magnetic dipole moments align in a parallel or antiparallel fashion to the magnetic field, creating distinct stationary states with different energy values. This phenomenon is known as the electron Zeeman interaction, and the energy of each state can be calculated by diagonalizing the Hamiltonian[143]

$$\hat{\boldsymbol{H}}_{\mathrm{EZI}} = -\hat{\boldsymbol{\mu}} \boldsymbol{B}_0 = \mu_{\mathrm{B}} \boldsymbol{B}_0^{\mathrm{T}} \boldsymbol{g} \hat{\mathbf{S}}, \tag{1.2}$$

where $\boldsymbol{B}_0$ is the external magnetic field and is always aligned with the z-direction of the spin angular momentum $\hat{S}_z$, and $\boldsymbol{g}$ is a 3× matrix with three principal values g_x, g_y, and g_z. The number of split states due to electron Zeeman interaction is $2S+1$. For nitroxides, the single unpaired electron is a $S = 1/2$ system, the electron Zeeman interaction thus creates a two-level system as illustrated in Fig. 1.2 top. The energy difference (ΔE) between the two states can be calculated by equation

$$\Delta E = \mu_{\mathrm{B}} g_{\mathrm{eff}} B_0, \tag{1.3}$$

$$g_{\mathrm{eff}} = |\boldsymbol{n}^{\mathrm{T}} g| \tag{1.4}$$

where g_{eff} is the effective g or the projection of g on the axis along the external magnetic field, $\boldsymbol{n}$ is the unit vector along $\boldsymbol{B}_0$, and the energy difference can be measured by the most basic EPR experiment, the continuous-wave (CW) experiment.

In the CW EPR experiment, the sample is irradiated with microwave of a constant frequency while the magnitude of the external magnetic field is varied. At the field strength where ΔE is equivalent to the microwave irradiation frequency, the electrons in the ground state are ex-

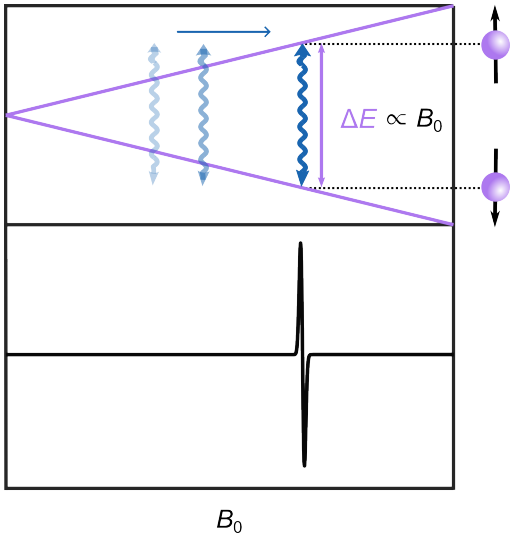

Figure 1.2: Electron Zeeman interaction diagram and CW EPR. Top: Zeeman interaction of a fictitious $S = 1/2$ electron spin system. Purple: the energy differences between the $m_S = +1/2$ and $m_S = -1/2$. Blue curly line: A microwave irradiation of constant frequency with transparency indicating off-resonance. Bottom: A simulated spectrum of with a peak at the resonance field in derivative lineshape.

cited to the excited state, which is known as the resonance phenomenon (Fig. 1.2 bottom). The CW EPR experiment is fundamentally an absorption experiment, but CW EPR spectra are often presented in derivative lineshapes since most CW spectrometers use a field modulation in combination with a lock-in amplifier to improve the signal-to-noise ratio (SNR). The magnetic field corresponding to resonance phenomenon is also referred to as resonance field and can be related to the g-value of an electron spin by equation 1.4. The g-value represents a molecular fingerprint and is often shifted from its free electron value $g_e = 2.0023$ by the magnetic environment around the electron spin.

The electron spin in nitroxides also experiences additional magnetic interactions, resulting in additional features in the CW EPR spectra. The magnetic interactions come from the nuclear spins of nitrogen atom (^{14}N and ^{15}N). Since the natural abundance of ^{15}N is almost negligible (0.368%), the rest of the thesis will be only focused on discussion using ^{14}N nucleus. The

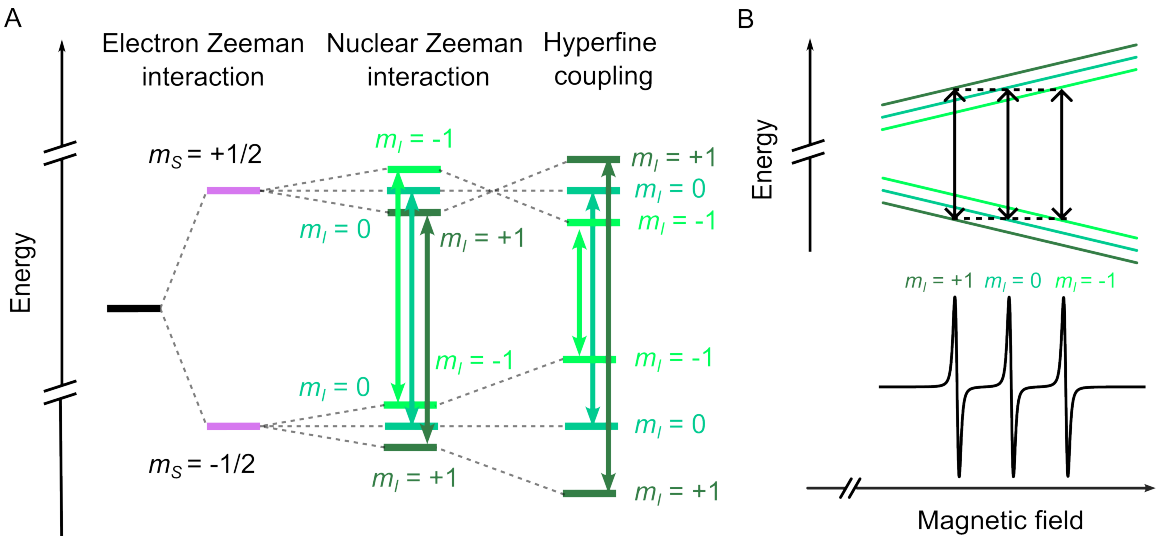

Figure 1.3: Nitroxides hyperfine coupling. A. Electron Zeeman splitting, nuclear Zeeman splitting and hyperfine coupling of a nitroxide ($S = 1/2$ and $I = 1$) at isotropic limit or at a single orientation. B. The CW EPR spectrum showing the three transitions (manifolds).

effective Hamiltonian of a nitroxide include four terms:[17]

$$\hat{\boldsymbol{H}} = \hat{\boldsymbol{H}}_{\mathrm{EZI}} + \hat{\boldsymbol{H}}_{\mathrm{NZI}} + \hat{\boldsymbol{H}}_{\mathrm{HFI}} + \hat{\boldsymbol{H}}_{\mathrm{NQI}}, \tag{1.5}$$

where $\hat{\boldsymbol{H}}_{\mathrm{EZI}}$ is the electron Zeeman interaction, $\hat{\boldsymbol{H}}_{\mathrm{NZI}}$ is the nuclear Zeeman interaction, $\hat{\boldsymbol{H}}_{\mathrm{HFI}}$ is the hyperfine interaction and $\hat{\boldsymbol{H}}_{\mathrm{NQI}}$ is the nuclear quadruple interaction. The nuclear Zeeman interaction is analogous to electron Zeeman interaction and is described by equation

$$\hat{\boldsymbol{H}}_{\mathrm{NZI}} = -\mu_{\mathrm{n}} g_{\mathrm{n}} \boldsymbol{B_0}^{\mathrm{T}} \hat{\boldsymbol{I}}, \tag{1.6}$$

where μ_{n} is the nuclear magneton and g_n the nuclear g-factor, which depends on the physical properties individual nucleus, and $\hat{\boldsymbol{I}}$ represents the spin angular momentum of the nuclear spin ($\hat{I}_x$, $\hat{I}_y$, $\hat{I}_z$). Similarly, the number of split states due to nuclear Zeeman splitting is $2I+1$. The nuclear spins also interact with the electron spin. This hyperfine interaction is described by

$$\hat{\boldsymbol{H}}_{\mathrm{HFI}} = \hat{\boldsymbol{S}}^{\mathrm{T}} \boldsymbol{A} \hat{\boldsymbol{I}}, \tag{1.7}$$

where the hyperfine coupling tensor $\boldsymbol{A}$ is also a 3×3 matrix with three principal values A_x, A_y, and A_z. The effect of the three magnetic interactions in an ^{14}N nitroxide is illustrated in Fig. 1.3A. The three transitions with identical energy differences are further shifted by hyperfine coupling between the electron spin and the nuclear spin, resulting in three transitions with distinct energies. If the hyperfine interaction is isotropic ($A_x = A_y = A_z$), the spectrum features three sharp lines from the $m_I = +1$, $m_I = +0$ and $m_I = -1$ from left to right, respectfully. If the spectral lines are sufficiently narrow, the hyperfine coupling from natural abundance of ^{13}C adjacent to the nitrogen atom will show as satellite peaks; however, for the experiments presented in this thesis, such features were never observed. The hyperfine couplings from ^{1}H on the methyl groups may be resolved but is not observed in the applications discussed in Chapter 2.

The last term in equation 1.5 is the nuclear quadruple interaction. The quadrupole interaction is due to the non-spherical electric charge distribution of the ^{14}N nucleus. The non-uniform electric field gradient is a result of other nuclei and electrons in the molecule. For the two applications presented in this thesis, all experiments are measured at X-band and Q-band frequencies, where the effect of ^{14}N quadruple moment is negligible; therefore, the term is not considered in simulations and discussions.

The magnetic interactions in nitroxides, such as the $\boldsymbol{g}$ and $\boldsymbol{A}$ tensors are often anisotropic. The origin of the g-anisotropy is attributed to the bonding environment. As shown in Fig. 1.4A, the unpaired electron in nitroxides is delocalized in a π^* orbital, consisting of the $2p_z$ atomic orbitals from nitrogen and oxygen atoms. The spin density on the oxygen atom participates in spin-orbit coupling with the orbital angular momenta from the oxygen $2p_x$ and $2p_y$ orbitals. The g_x and g_y values are affected by the local polarity and hydrogen bonding environment oxygen, whereas the g_z usually experiences less deviation. This phenomenon is observed in an application presented in Chapter 2.

At X-band frequencies, the nitroxide g-anisotropy does not affect the lineshapes as significantly as the A-anisotropy does. The anisotropy of the hyperfine interaction is due to the through-space dipolar coupling between the electron and the nucleus. The molecular prin-

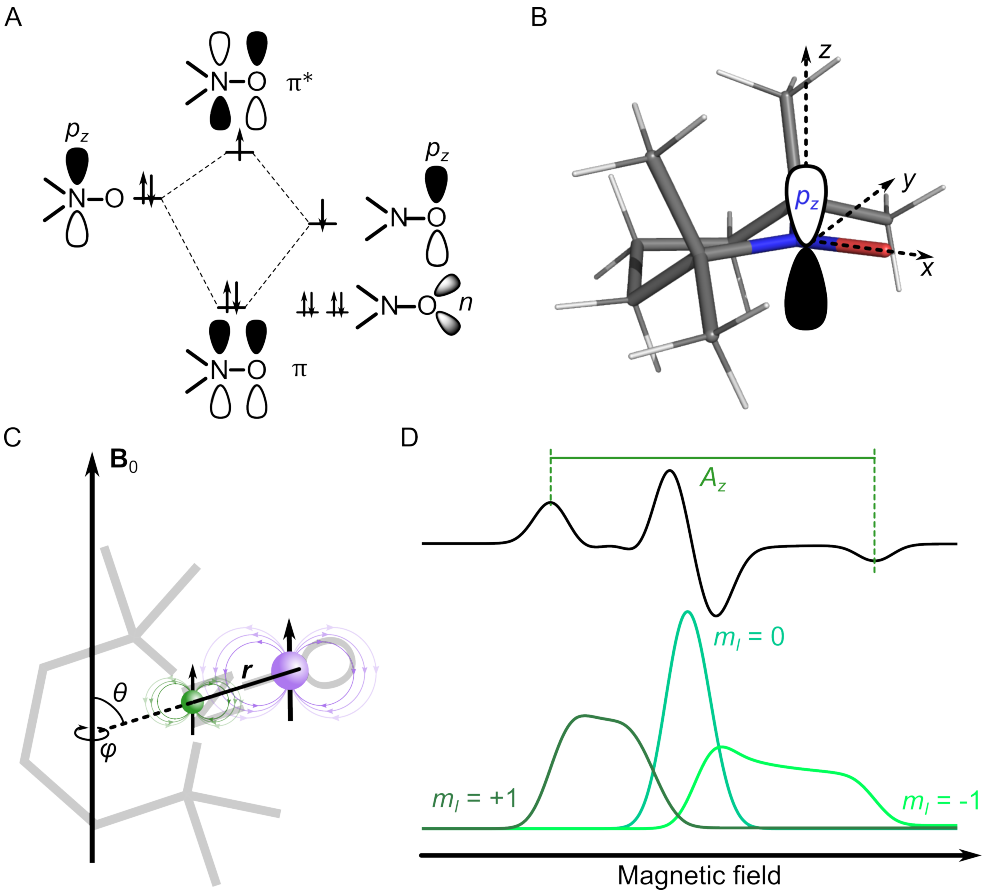

Figure 1.4: Nitroxide bonding environment and molecular orientations. A. Molecular diagram of the NO group on nitroxide. B. The molecular frame on a TEMPO molecule. The $\boldsymbol{g}$-tensor and $\boldsymbol{A}$-tensor are defined with the same principal axes. C. A diagram of the nucleus–electron dipolar hyperfine coupling. The spin–spin vector form an angle θ with the direction of the external magnetic field. D. Top: powder spectrum of TEMPO molecule plotted in derivative lineshape. The largest hyperfine values A_z is indicated by green lines. Botton: Same spectrum plotted in absorption lineshape with three manifolds plotted separately.

cipal axes are defined in Fig. 1.4B, where the N–O bond is defined as the x-axis. To illustrate the orientational effect, it is convenient to rewrite $\boldsymbol{A}$ as the sum of an isotropic component and an orientation-dependent component:[15]

$$\begin{aligned} \boldsymbol{A} &= a_{\mathrm{iso}}\hat{\boldsymbol{S}}^{\mathrm{T}}\hat{\boldsymbol{I}} + \hat{\boldsymbol{S}}^{\mathrm{T}}\boldsymbol{T}\hat{\boldsymbol{I}}, \\ a_{\mathrm{iso}} &= \frac{2\mu_0}{3} g_{\mathrm{e}}\mu_{\mathrm{B}} g_{\mathrm{n}}\mu_{\mathrm{N}}\rho_{\mathrm{N}}^{\alpha-\beta}, \\ \boldsymbol{T} &= \frac{\mu_0}{4\pi} g_{\mathrm{e}}\mu_{\mathrm{B}} g_{\mathrm{n}}\mu_{\mathrm{N}}\left[\frac{3\boldsymbol{r}\cdot\boldsymbol{r}^{\mathrm{T}}}{r^5} - \frac{\mathbf{1}}{r^3}\right]. \end{aligned} \tag{1.8}$$

The a_{iso} term is the isotropic hyperfine coupling or the Fermi contact coupling, where μ_0 is the vacuum permeability and $\rho_{\mathrm{N}}^{\alpha-\beta}$ is the spin density at the nucleus N. The term $\boldsymbol{T}$ describes the dipolar hyperfine coupling between nuclear and electron spins. The dipolar hyperfine coupling depends on the relative orientation of the electron spin and nuclear spin and can be written in an alternative form:

$$\begin{aligned} \boldsymbol{T} &= \frac{\mu_0}{4\pi} g_{\mathrm{e}}\mu_B g_{\mathrm{n}}\mu_N \begin{pmatrix} 1-3{u_x}^2 & -3u_x u_y & -3u_x u_z \\ -3u_x u_y & 1-3{u_y}^2 & -3u_y u_z \\ -3u_x u_z & -3u_y u_z & 1-3{u_z}^2 \end{pmatrix}, \\ \boldsymbol{u} &= \frac{\boldsymbol{r}}{r} = \begin{pmatrix} \sin\theta\cos\phi \\ \sin\theta\sin\phi \\ \cos\theta \end{pmatrix}, \end{aligned} \tag{1.9}$$

where $\boldsymbol{r}$ is the electron-nucleus spin vector, and r being the distance between the two, and ϕ and θ are angles indicated in Fig. 1.4C. The hyperfine anisotropy of nitroxide can be averaged, partially averaged and completely resolved in the EPR spectrum depending on the motional regime, which will be discussed in section 1.2.

1.2 Solution-state EPR and nitroxide lineshape analysis

In solution-state EPR experiment, nitroxide spin labels are sensitive to reorientation and rotational dynamics. With careful lineshape analysis, solution-state EPR spectra can be used for interpreting spin label motion and its local environment. The EPR-observed molecular motion can be classified into four regimes based on the ratio between their rate of rotational motion, measured as the rotational correlation time τ_c, and the spectral linewidth, denoted as $\Delta\omega$ as illustrated in Fig1.5. In an extreme case, the isotropic limit, the anisotropy is fully averaged due to very fast molecular tumbling reorientation, rendering a spectrum that consists of three well resolved lines of essentially equal width (Fig. 1.3B). The other extreme case is the rigid limit, where spin labels are staticrelative to $1/\Delta\omega$, resulting in a range of θ (Fig. 1.4C) and completely resolved anisotropy. The rigid limit may be observed in either frozen solution of spin labels or immobilized spin labels at room temperature. Simulating the lineshapes in the isotropic limit can be performed by solving the nitroxide spin Hamiltonian using only the isotropic components of the $\boldsymbol{g}$ and $\boldsymbol{A}$ matrices, and the rigid limit case can be implemented by using the full $\boldsymbol{g}$ and $\boldsymbol{A}$ matrices and averaging over a complete orientational distribution.

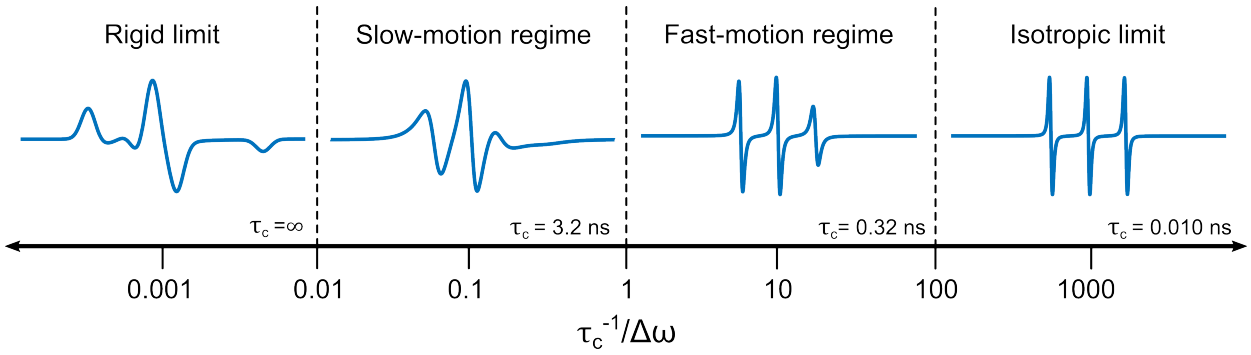

Figure 1.5: Four regimes of EPR-observed spin label rotational motion.

The lineshape analysis of spectra that fall between the two extreme cases, especially spectra in the slow-motion regime, is challenging due to the complexity of dynamics. A common treatment for fitting slow-motion regime spectra is to solve the stochastic Liouville equation

(SLE):

$$\partial_t \rho(\mathbf{\Omega}, t) = -i\hat{H}^{\times}(\mathbf{\Omega})\rho(\mathbf{\Omega}, t) - \Gamma(\mathbf{\Omega})\rho(\mathbf{\Omega}, t), \tag{1.10}$$

where $\hat{H}^{\times}$ is a Hamiltonian commutation superoperator defined by $\hat{H}^{\times}\rho \equiv [\hat{H}, \rho]$, $\rho(\mathbf{\Omega}, t)$ represents the spin density operator with the orientation of the rotating molecule($\mathbf{\Omega}$) at time t, and $\Gamma(\mathbf{\Omega})$ is the diffusion operator representing the dynamics of rotational motion. The SLE equation computes the evolution of spin density matrix under the effect of molecular dynamics implemented as the change of orientation over time. The explicit form of the diffusion operator $\Gamma(\mathbf{\Omega})$ may vary depending on the choice of diffusion model. This work on this thesis is focused on a particular model, the Brownian rotational diffusion model,.[21,79]

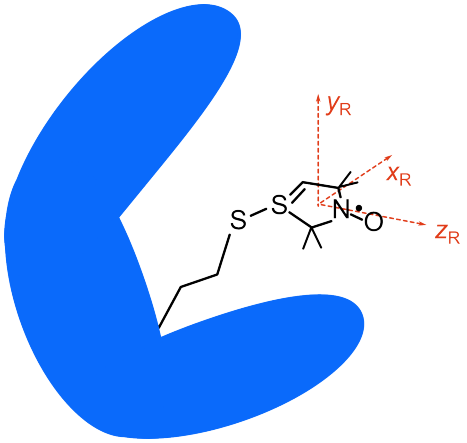

Figure 1.6: Rotational diffusion tensor ($\boldsymbol{R}$) on a spin label conjugated to a protein. The red dotted arrows represent the principal axes of $\boldsymbol{R}$.

Analogous to random walk in translational motion, the Brownian rotational diffusion model steps incremental changes of rotational angles. To implement this method, a rotational diffusion tensor, $\boldsymbol{R}$, with three principal axes as shown in Fig. 1.6 is introduced, and $\Gamma(\mathbf{\Omega})$ takes the explicit form of

$$\Gamma = \sum_{i,j=x,y,z} R_{ij} J_i J_j + \frac{1}{k_B T} \sum_{i,j=x,y,z} R_{ij} J_i (J_j U(\mathbf{\Omega})) \tag{1.11}$$

where J_x, J_y, and J_z are the components of the rotational angular momentum of the molecule, and $U(\mathbf{\Omega})$ describing a potential energy surface. The potential energy surface adds more con-

straints to the diffusion model. Depending on sample conditions and local environment of spin labels, *e.g.* a liquid crystal sample or a spin label at a buried site on a protein, physical constraints may restrict the orientational space accessible for spin label reorientation. The rotational diffusion tensor $\boldsymbol{R}$ can be specified either using diffusion rates in unit of s^{-1} or using the rotational correlation time τ_c. A conceptual approach to interpret τ_c introduced in Fig. 1.5 is the time duration during which a molecular rotates over a fixed angle. In a system where the rotational diffusion tensor is anisotropic, three τ_c values, τ_{c_x}, τ_{c_y}, and τ_{c_z} may be specified to obtain a good fit of a spectrum.

By solving the SLE implemented by using a Brownian diffusion model, practitioners are able to obtain the dynamics of spin label reorienting or rotation in solution environment. The τ_c values are useful in terms of interpreting the dynamics of spin labels and therefore their surroundings. The same simulation method is used for lineshape analysis in Chapter 2 with more details.

1.3 Double electron-electron resonance experiment and protein conformational change

This section introduces another EPR experiment known as the double electron–electron resonance (DEER) spectroscopy. DEER is a pulse EPR experiment, which is a different technique from the CW experiment introduced in section 1.1. In pulse EPR experiments, the continuous microwave irradiation is replaced with short but more high-power pulses of microwave. In most pulse EPR experiments, the detected signal is the total magnetization of a spin ensemble. Figure 1.7 illustrates the simplest pulse experiment, the Hahn echo or spin–echo experiment. The magnetic field of a microwave pulse, denoted as $\boldsymbol{B}_1$, interacts with the magnetic moment of the spins and nutates the spins out of the principal z-direction. The nutation angle is usually 90°($\pi/2$) and 180° (π). The $\pi/2$ pulse nutates the magnetic dipole of spins into the xy-plane and leaves spins precessing in the plane. In molecular ensembles, the spins may consists of subpopulations that are precessing at various frequencies due to the difference in local chemical environment, represented by the colored arrows in Fig. 1.7. The sub-populations can be refocused using π pulse, which flips the spins with respect to z-axis. After another delay time τ, the

magnetization of the precessing spins are refocused to produce what is known as an echo. The refocused magnetization decreases as τ increases as the precessing frequency of all spins sub-populations will change over time due to spin–spin relaxation or decoherence or spin-lattice relaxation. In the Hahn echo experiment, the decay of echo intensity is monitored as a function of increasing length of τ, denoted as $V(2\tau)$.

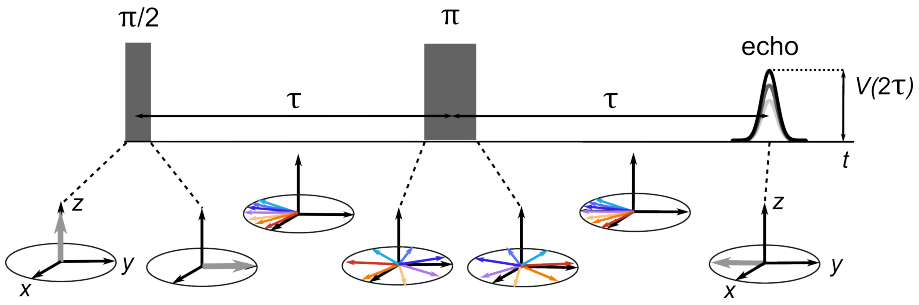

Figure 1.7: Hahn echo/spin echo experiment in EPR. Top: the pulse sequence, consisting of a $\pi/2$ and a π pulses with a inter-pulse delay time τ. An echo is produced after another delay time τ. Botton: magnetization of the spin ensemble. Light gray: the collective magnetization of all spin sub-populations. Colored arrows: spin sub-populations with different precessing frequencies.

A DEER experiment works on the same physical basis. The experiment is primarily used for measuring the distance distribution between two electron spin centers and therefore requires the sample to have two electron spins. The two electron spins are referred as the probe spins (A spins) and pump spins (B spins) based on how they are addressed in a DEER experiment. Similar to the dipolar hyperfine coupling introduced in section 1.1, the two electron spins are magnetically coupled, and the coupling strength is characterized by their dipolar coupling frequency, ω_{AB}. The dipolar coupling frequency is inversely proportional to the spin–spin distance, r^3, and is described by

$$\omega_{AB}(\theta, r) = \frac{\mu_0}{4\pi} \frac{g_A g_B \mu_B^2}{\hbar} \frac{1}{r^3} (1 - 3\cos^2\theta) \tag{1.12}$$

where g_A and g_B are the g-values of the corresponding spins, r is the spin–spin distance and θ is the angle between the inter-spin direction r and the magnetic field. If a selective π pulse

is applied to one spin population in such a system, the precession frequency is shifted by ω_{AB} as illustrated in Fig. 1.8A. The most widely used DEER pulse sequence is the four-pulse DEER, shown in Fig. 1.8B. The signal $\boldsymbol{V}(t)$ is measured from the probe spins while an additional π pulse is applied to the pump spins, the precession frequency of the pump spins are shifted by ω_{AB}, leading to a reduction of spins that can be refocused by the probe pulse. The attenuated echo amplitude depends on the timing of the pump pulse, and the time-domain DEER signal is often oscillatory. A typical application of DEER experiment is to measure the distance between two sites on a biomolecule (Fig. 1.8C, right) by attaching two spin labels via site-directed spin labeling (SDSL). The middle panel in Fig. 1.8C is a simulated DEER trace using the spin–spin distance r from the right panel. The oscillatory signal can be further divided into two parts:

$$V(t) = V_{\text{intra}}(t)\, V_{\text{inter}}(t) \tag{1.13}$$

where the $\boldsymbol{V}_{\text{intra}}(t)$ is the contribution from the pump and probe spins on the same molecule and $\boldsymbol{V}_{\text{inter}}(t)$ (Fig. 1.8C, middle, dashed line) is the contribution from pump spins on other molecules in sample. The $\boldsymbol{V}_{\text{inter}}(t)$ is sometimes referred to as the background signal. Under appropriate assumptions,[68,110] such as dilute spin concentration and no experimental artefacts, $\boldsymbol{V}_{\text{intra}}(t)$ is related to distance distribution $\boldsymbol{P}(r)$ by equation:

$$V_{\text{intra}}(t) = \hat{K} P(r) \tag{1.14}$$

where $\hat{K}(t,r)$ is the kernel operator that integrates signal from pump–probe spin pairs. The inverse problem is ill-posed therefore sensitive to noise and yields large uncertainties in $P(r)$. A variety of data analysis models and complementary software packages have been widely used in the research community, including Tikhonov regularization,[44] neural network,[147] global analysis[19] and others.

The pulse sequence presented in Fig. 1.8 consists of rectangular pulses. Rectangular pulses often have limited bandwidth as well as excitation side bands, causing artefacts such as incom-

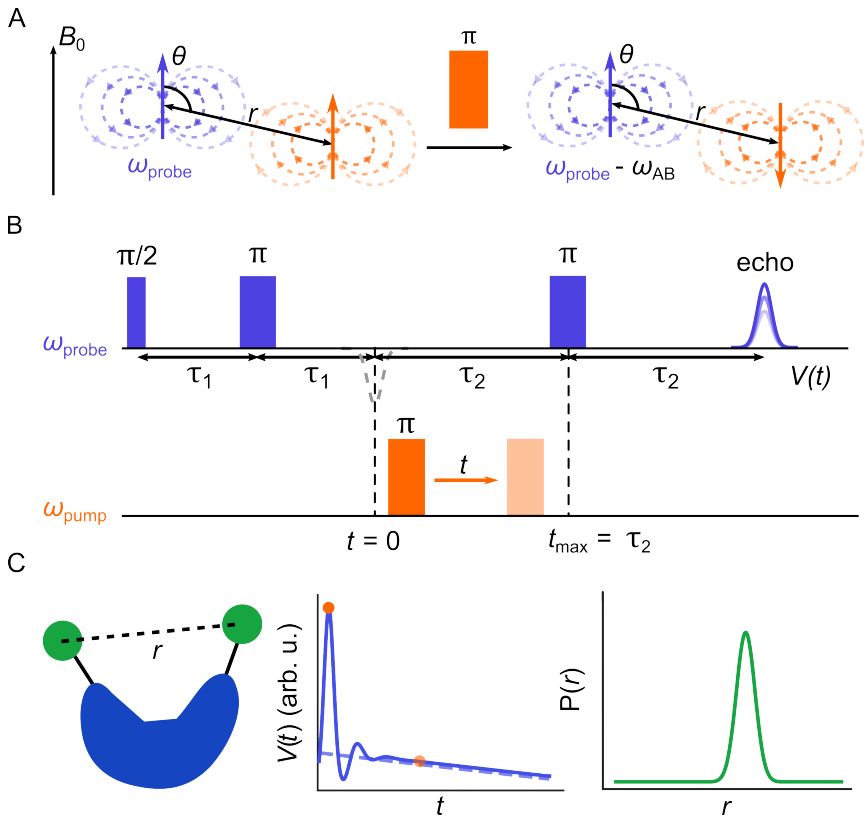

Figure 1.8: Four-pulse DEER experiment. A. Dipolarly coupled probe spins (blue) and pump (orange) spins and the effect of a π pump pulse. B. The pulse sequence. Top: the pulses applied to the probe spins with frequency ω_{probe}. Bottom: the π pulse applied to the pump spins with with frequency ω_{pump}. τ_1: the delay time between the first $\pi/2$ and π probe pulses. τ_2: the delay time between the first echo and the second π probe pulse. t: timing of the pump pulse. $t_{\text{max}} = \tau_2$: the latest moment to apply the pump pulse without having overlap with the last probe pulse. C. Left: a doubly spin-labeled protein with spin–spin distance r. Middle: a simulated time-domain DEER signal based on r (solid line) Dashed line: inter-molecular contribution to the overall signal. Right: a distance distribution, $P(r)$, obtained from $V_{\text{intra}}(t)$.

plete inversion of pump spins and pulse overlaps, respectively.[125] The problems are illustrated in the inversion profile in Fig. 1.9A, where the rectangular pump pulses only inverts a small fraction of spins. Although the excitation bandwidth can be increased by using shorter rectangular pulses, shorter pulses also generate wider sidebands, which then lead to greater degree of pump–probe excitation band overlap. A remedy to remove the sidebands is to use a Gaussian shaped pulse (Fig. 1.9B, green). A Gaussian pulse has an amplitude modulation envelope with a

shape of Gaussian. The frequency-domain profile of a Gaussian pulse does not have sidebands, but the caveat is that Gaussian pulses may result in a narrower excitation bandwidth.[125]

Another set of pulses, known as adiabatic pulses, can be applied to optimize the inversion profile of pump spins.[125,126] Such pulses are designed to achieve a well-defined excitation profile, including a greater width of frequencies. Figure 1.9B shows a case where a Gaussian probe pulse and a hyperbolic secant, or sech/tanh pulse are used in DEER experiment, where the sech/tanh pulse covers a wider range of pump spins without having any overlap with the Gaussian probe pulse. The combination of these two pulses will be used for the application presented in Chapter 3.

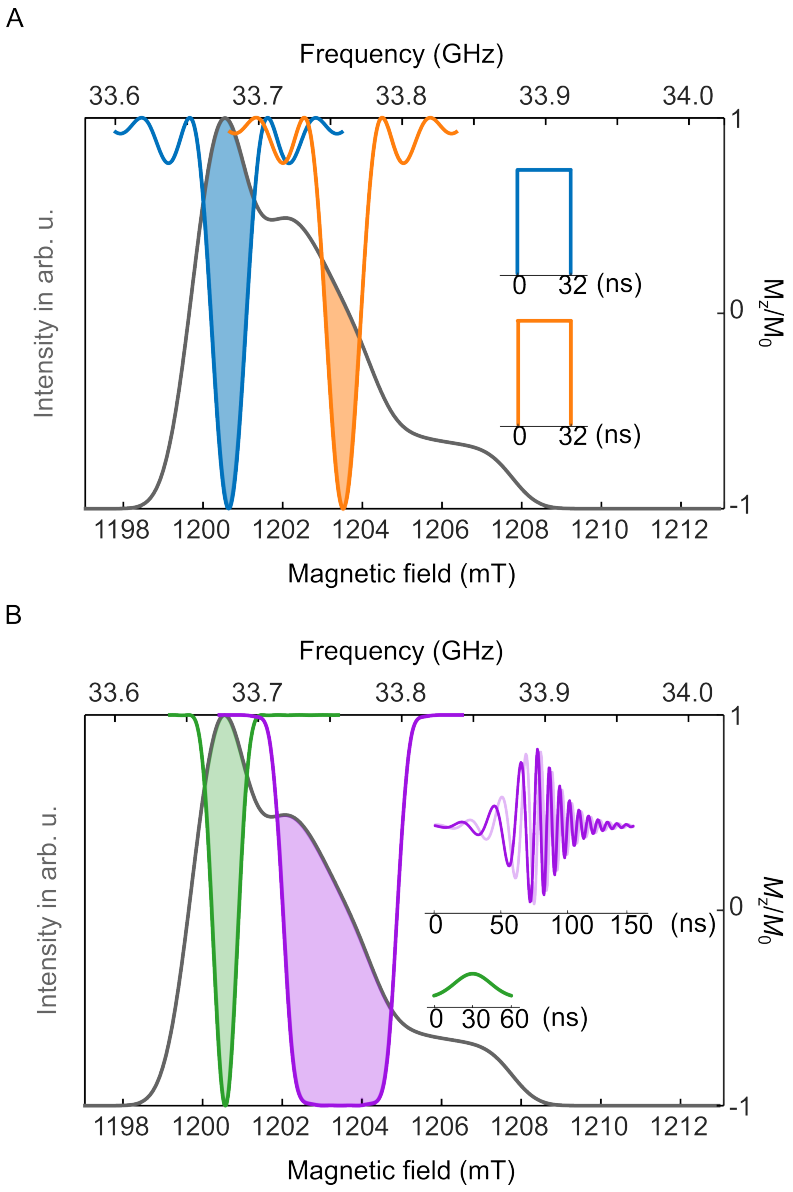

Figure 1.9: Inversion profiles of pulses with different shapes. Gray: nitroxide spectrum in absorption lineshape. The probe pulses are centered at the maximum and the pump pulses are centered 80 MHz higher than the probe pulses. Shaded region: visual representation of the flipping efficiency of the pulses. Inset: the time-domain pulse shape. A. The inversion profile of a 32 ns-long rectangular probe (blue) and a 32 ns-long rectangular pump (orange) pulse. B. The inversion profile of a 60 ns-long Gaussian probe (green) pulse and a 150 ns-long sech/tahn pump (purple) pulse. The transparent lines in the sech/tahn pulse represents signal in the imaginary channel.

Chapter 2

MAGNETICALLY DETECTED PROTEIN BINDING USING SPIN-LABELED SLOW OFF-RATE MODIFIED APTAMERS

Recent developments in aptamer chemistry open up opportunities for new tools for protein biosensing. In this work, we present an approach to use immobilized slow off-rate modified aptamers (SOMAmers) site-specifically labelled with a nitroxide radical via azide–alkyne click chemistry as a means for detecting protein binding. Protein binding induces a change in rotational mobility of the spin label, which is detected via solution-state electron paramagnetic resonance (EPR) spectroscopy. We demonstrate the workflow and test the protocol using the SOMAmer SL5 and its protein target, platelet-derived growth factor B (PDGF-BB). In a complete site scan of the nitroxide over the SOMAmer, we determine the rotational mobility of the spin label in the absence and presence of target protein. Several sites with sufficiently tight affinity and large rotational mobility change upon protein binding are identified. We then model a system where the spin-labeled SOMAmer assay is combined with fluorescence detection via diamond nitrogen–vacancy (NV) center relaxometry. The NV center spin–lattice relaxation time is modulated by the rotational mobility of a proximal spin label and thus responsive to SOMAmer–protein binding. The spin label-mediated assay provides a general approach for transducing protein binding events into magnetically detectable signals.[1]

---

[1]This chapter is revised based on the 2023 publication in *ACS Sensors* by Shutian Lu, Catherine R. Fowler, Brian Ream, Sheela M. Waugh, Theresa M. Russell, John C. Rohloff, Larry Gold, Jason P. Cleveland, and Stefan Stoll, titled "Magnetically Detected Protein Binding Using Spin-Labeled Slow Off-Rate Modified Aptamers.", volume 8, pages 2219–2227, available at https://doi.org/10.1021/acssensors.3c00112. The SOMAmers were synthesized and characterized at SomaLogic, and the EPR experiments were performed at University of Washington.

2.1 Background and motivation

Regular and complete proteomics panels can provide real-time diagnostic insight into human health and enable preventive and early treatments of nascent disease states.[30,152] Such measurements must be reliable and require fast, accurate and accessible multi-protein sensors. Novel designs for such sensors featuring small sample volumes and high sensitivity have become feasible due to the recent developments in aptamer chemistry and quantum technologies.[46,118,123] A special class of DNA aptamers known as slow off-rate modified aptamers (SOMAmers) have been used as molecular binding reagents in a variety of biochemical studies.[33,63,106,149] SOMAmers are selected for tight binding interaction to target proteins and contain a series of nucleobases modified using hydrophobic constituents such as benzene and naphthalene rings.[50] The incorporation of these modifications has been demonstrated to improve the binding specificity and affinity of SOMAmers. With these properties, SOMAmers are reliable agents for capturing traces of specific target proteins.[39,76] In general, the SOMAmers are selected to form tight interactions with their targets with K_{d} values in the range of several nM to pM.[5,38,47,54] Structural information has been obtained from several SOMAmer–protein complexes.[26,48,65,106]

The specificity and affinity of SOMAmer–protein interactions can be fully utilized if they are paired with sensitive detection methods, ideally at the single-molecule level. One option for such a quantum sensor is the negatively charged nitrogen–vacancy (NV) center in diamond. The NV center is a defect color center with a spin-triplet ($S = 1$) ground state localized on the three dangling carbon bonds next to the vacancy. It can be spin polarized via optical pumping and provides a spin-sensitive fluorescence readout. The use of the NV center as a quantum sensor for local magnetic fields is well studied.[6,13,29] Numerous studies have demonstrated the ability of NV centers to detect the presence of proximal spin species, such as proton spins on the diamond surface,[134] proton spins in the solvent[31,80,140] and single electron spin centers in proximal biomolecules.[3,81,83,87,120,121]

There are several challenges that must be overcome in order to integrate SOMAmers and NV

center-mediated detection into a device for protein sensing. One is to develop a biocompatible surface on NV center-hosting diamond for SOMAmer attachment.[148] Another is translating the SOMAmer–protein binding event to a magnetic signal, which then can be detected via differential optical readout of an NV center. To address the second challenge, here we propose a protein binding assay that uses site-directed spin labeling of SOMAmers to generate a magnetic signal from a SOMAmer–protein binding event. Figure 2.1A illustrates the principles of this proposed mechanism. The unbound SOMAmer (apo state) is spin-labeled with a paramagnetic nitroxide radical ($S = 1/2$) at a specific nucleotide and is covalently attached to the diamond surface, proximal to an NV center. The spin label is incorporated at an appropriately chosen solvent-exposed site of the SOMAmer and is therefore rotationally mobile. When a target protein binds to a SOMAmer (holo state), the spin label's rotational mobility is reduced, and its distance to the NV center is possibly shifted. Both the rotational mobility change and the distance change affect the NV center spin–lattice relaxation rate, characterized by the longitudinal relaxation time constant T_1.[8,80,140] This rate can be measured using an optically detected magnetic resonance (ODMR) approach.[16,55,130,140]

For this detection mechanism to work, the spin-labeled SOMAmer must satisfy several prerequisites. First, the incorporation of the spin label must not degrade the SOMAmer–protein binding affinity; second, the spin label must undergo a significant rotational mobility or distance change upon protein binding; third, the rotational mobility or distance change must be on a scale that sensitively affects the NV center longitudinal relaxation rate. To identify sites that optimally satisfy these requirements, a complete scan of all spin labeling sites, i.e. all nucleotides, on a SOMAmer is necessary. While distance changes are only relevant in the presence of NV centers, rotational mobility changes can be measured using solution-state electron paramagnetic resonance (EPR) spectroscopy, a technique sensitive to molecular rotation rates on a time scale between 0.1 ns and 100 ns.[17]

In this work, we present a solution protein binding assay based on immobilized spin-labeled SOMAmers. We use a nitroxide-based spin label, since nitroxides are well-studied in solution EPR experiments and are sensitive reporters of molecular rotational motion.[41,61] The spin label

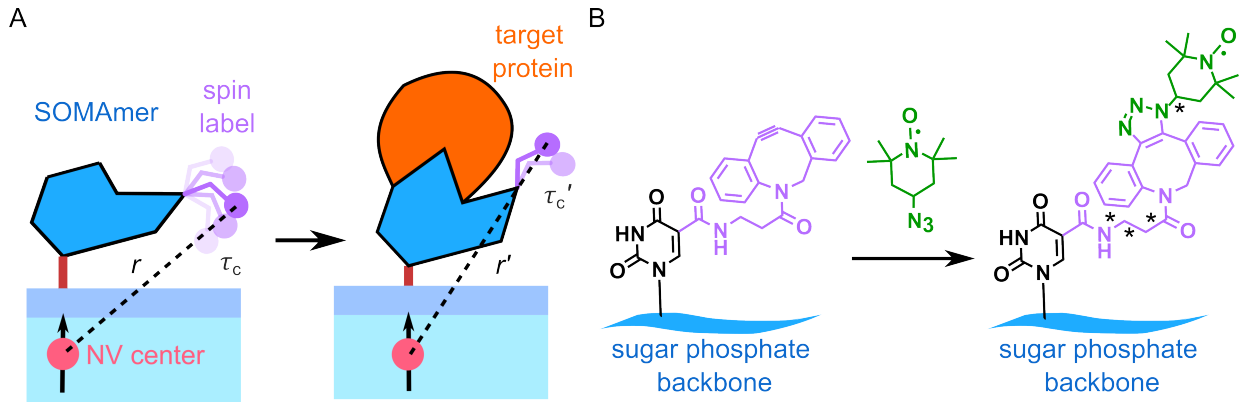

Figure 2.1: Schematic representation of NV-detected protein binding using spin-labeled SOMAmers. A. The apo and holo states of a SOMAmer covalently attached to the surface of a functionalized diamond via a linker (red). A spin label at distance r from the NV center is rotating with rate constant τ_c with little restriction. Protein binding potentially restricts and slows the rotational mobility and changes the distance from the spin label to the NV center. B. Chemical structures of uracil (black) modified with dibenzocyclooctyne (DBCO, purple) and nitroxide spin label (green). The asterisks indicate rotatable bonds. The spin label is incorporated via catalyst-free azide–alkyne cycloaddition.

is incorporated into a SOMAmer via site-specific azide–alkyne cycloaddition as shown in Fig. 2.1B.[2,71] A model system was used for optimizing the spin labeling procedure and demonstrating the workflow for selecting labeling sites using two criteria: a small dissociation constant (K_d) and a large change in rotational mobility in response to protein binding, quantified by the rotational correlation time constant (τ_c) of a fitted Brownian rotational diffusion model. The model system consists of a SOMAmer named SL5 and its target protein, platelet-derived growth factor B (PDGF-BB dimer).[26] We performed binding affinity assays for all labeling sites on SL5 and identified 19 non-disruptive sites. The associated constructs were immobilized on agarose beads via streptavidin-biotin linkers. The rotational mobility changes were then evaluated using solution-state EPR spectroscopy combined with spectral simulations to obtain τ_c before and after addition of PDGF. Several sites show a significant change τ_c, demonstrating the feasibility of this magnetically detected assay. Using the experimentally determined τ_c, we also model the impact of τ_c on NV center T_1 relaxation and discuss the effect of the NV center–spin label geometry on the overall robustness of a T_1 relaxometry-based detection mechanism.

2.2 Preparation and characterization of spin-labeled SOMAmers

2.2.1 Spin-labeled SOMAmer preparation

An ABI 3900 automated DNA synthesizer (Applied Biosystems) was used with conventional phosphoramidite methods with minor changes to the coupling conditions for modified phosphoramidites. Modified phosphoramidites were used in 0.1 M solutions using acetonitrile with 0-40% dichloromethane and 0-20% sulfolane as the solvent. Solid support was an ABI-style fritted column packed with controlled pore glass (CPG, LGC Biosearch Technologies) loaded with 3'-DMT-dT succinate with 1000 Å pore size. All syntheses were performed at the 50 nmol scale and the 5' end of each sequence was modified with a hexaethylene glycol (HEG) spacer and biotin group for support attachment. Introduction of a DBCO-modified nucleotide variant was done as a single-base replacement at selected sites within the DNA strand using phosphoramidites synthesized by SomaLogic, Inc. Deprotection was accomplished by treatment with concentrated ammonium hydroxide at 55 °C for 4-6 hours, after which the product mixtures were filtered and residual solvents removed in a Genevac HT-12 evaporator. Identity and percent full-length product were determined using an Agilent 1290 Infinity LC system with an Agilent 6130B single quadrupole mass spectrometry detector using an Acquity C18 column 1.7 µM 2.1x100mm (Waters).

The resulting crude DBCO-modified SOMAmer residues were then redissolved in water for injection (WFI, HyPure WFI Quality Water, HyClone Laboratories, or equivalent) to 0.17 mM concentration (based on synthesis scale). A 100 mM solution of commercially sourced 4-azido-2,2,6,6-tetramethyl-piperidinyl-1-oxyl (TEMPO) azide (Glen Research 50-2007-92) was prepared in dimethyl sulfoxide. Each oligonucleotide mixture received an aliquot of the azide solution at a 4:1 ratio of azide to SOMAmer (based on synthesis scale) and the resulting mixture was mixed at room temperature for 24 to 65 hours, at which time analysis by LC/MS (Agilent 1290 Infinity, configured as above) confirmed that each cycloaddition reaction had reached completion as indicated Fig. 2.2. Each reaction mixture was then centrifugally filtered (Millipore Amicon Ultra-15 3K), washed three times with 5 mL WFI per wash for removal of small molecule impu-

rities. Product was collected in approximately 500 µL WFI without further purification.

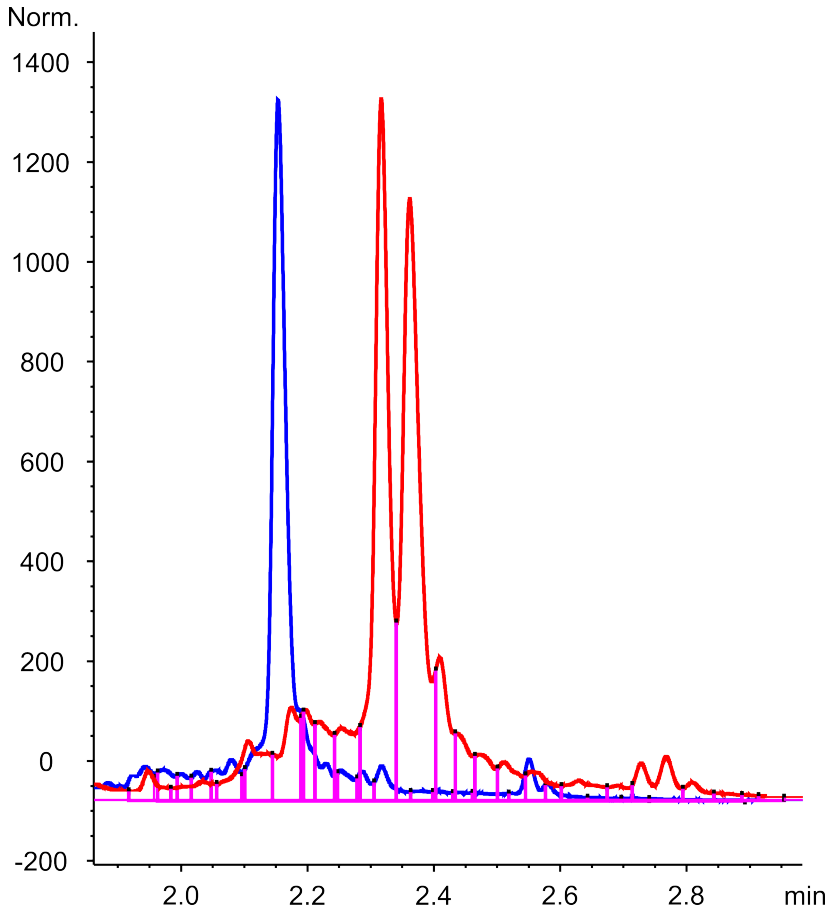

Figure 2.2: Liquid chromatography mass spectrometry analysis of azide-alkyne cycloaddition. Blue: DBCO-modified SOMAmers. Red: TEMPO-labeled SOMAmers. The dual peaks were observed from two stereoisomers of the cycloaddition. Purple: fragmentation patterns from mass spectrometry analysis. This figure was produced by staff at SomaLogic. Inc.

To spin label residues 1-4 and 11-29, we used the SL5 parent construct that contains a HEG linker in place of residues 5-10. To spin label residues 5-10, we used SL5 with the sequence GACZAC in place of the HEG linker, where Z is the modified nucleotide 5-benzylaminocarbonyl.[26] In this paper, the numbering is based on the 29-residue length.

2.2.2 Binding affinity measurements

To determine the K_d of modified aptamers, filter binding assays were performed using the SB18T binding buffer (40 mM HEPES, 102 mM NaCl, 5 mM KCl, 5 mM $MgCl_2$ and 0.01% Tween-20, pH 7.4). Modified aptamers were 5' end labelled using T4 polynucleotide kinase (New England Biolabs) and γ-[^{32}P]ATP (Perkin-Elmer). Radiolabeled aptamers (~20,000 cpm) were mixed with PDGF-BB (Creative BioMart) at concentrations ranging from 10^{-7} to 10^{-12} M and incubated at 37 °C for 40 minutes. Following incubation, 5.5 mL of 400 mg/mL silica-based microspheres (5 µM Zorbax PSM 300A, Cat. No. 899999-555, Agilent Technologies) was added, and bound complexes were captured on Durapore filter plates (EMD Millipore). The fraction of bound aptamer was quantified with a phosphoimager (Typhoon, GE Healthcare) and data were analyzed in ImageQuant (GE Healthcare).

2.2.3 Sample preparation for EPR measurements

The SOMAmer constructs used in EPR measurements were biotinylated[76] at the 5' end to facilitate immobilization on agarose beads coated with immobilized recombinant streptavidin protein (Pierce Streptavidin Plus UltraLink #53117; ThermoFisher Scientific). The bead diameter varies from 50 to 80 µm. SOMAmer concentration was determined by measuring the absorbance at 260 nm. Resin (0.5 mL of 50% slurry) was buffer exchanged into SB18T buffer, the supernatant was removed and 20 nmol of SOMAmer was applied to the resin. The reaction was incubated, with end-over-end rotation, at 37 °C for 1 hour. Resin was pelleted and supernatant was removed and discarded. Unbound streptavidin was quenched with 0.9 mL reaction buffer containing biotin. SOMAmer-loaded resin was washed thrice with 1 mL reaction buffer and resuspended in a final volume of 0.5 mL for a final concentration of 40 µM SOMAmer in 50% slurry. SOMAmer-loaded resin was stored at 4 °C. The PDGF-BB protein was stored at -80 °C then dissolved before use.

2.2.4 EPR measurements

Continuous-wave (CW) EPR experiments were performed with 40 μM SOMAmers in SB18T buffer. For the protein binding experiments, protein targets with concentration of 45-50 μM were added. For each sample, 12-15 μL were transferred into quartz capillaries (1.0 mm O.D. and 0.7 mm I.D.; Sutter Instrument). Solution-state EPR spectra were collected at room temperature (23 °C) using an X-band continuous-wave (CW) Bruker EMX spectrometer equipped with a ER 4123D dielectric resonator with a resonance frequency of 9.77 GHz. All spectra were obtained with a peak-to-peak modulation amplitude of 0.1 mT and a sweep rate of 0.24 mT/s and were collected under non-saturating conditions at 0.64 mW. Power saturation experiments are presented in Fig. 2.3 performed to ensure all spectra were taken in the unsaturated regime.

2.2.5 EPR spectral simulations

All spectra were aligned to the same magnetic field range and scaled by number of scans, receiver gain, and square root of power. Then, background was removed by subtracting the spectrum of buffer solution only. The spectra were integrated and normalized to obtain absorption spectra for simulation and comparison. An isotropic rigid-body Brownian rotational diffusion model[101,115] without motional restriction was fitted to the measured spectral lineshapes. The isotropic rotational correlation time τ_c and the g-tensor principal values (g_x, g_y, g_z) were varied for each fit. The hyperfine tensor principal values ([A_x, A_y, A_z] = [21.79(3), 12.43(2), 103.01(2)] MHz) and the homogeneous broadening were simulated from a spectrum collected using a frozen solution of a free SOMAmer labeled at site 1 as shown in Fig. 2.4. Spectral simulations were performed using the open-source MATLAB toolbox EasySpin 6.0.0-dev.49.[132]

2.3 Evaluating binding assay and rotational mobility assay

2.3.1 Binding affinity assay

To identify non-disruptive labeling sites, the binding affinities for PDGF of all SL5 constructs spin-labelled at each of the 29 sites were measured. The determined values of K_d are shown in

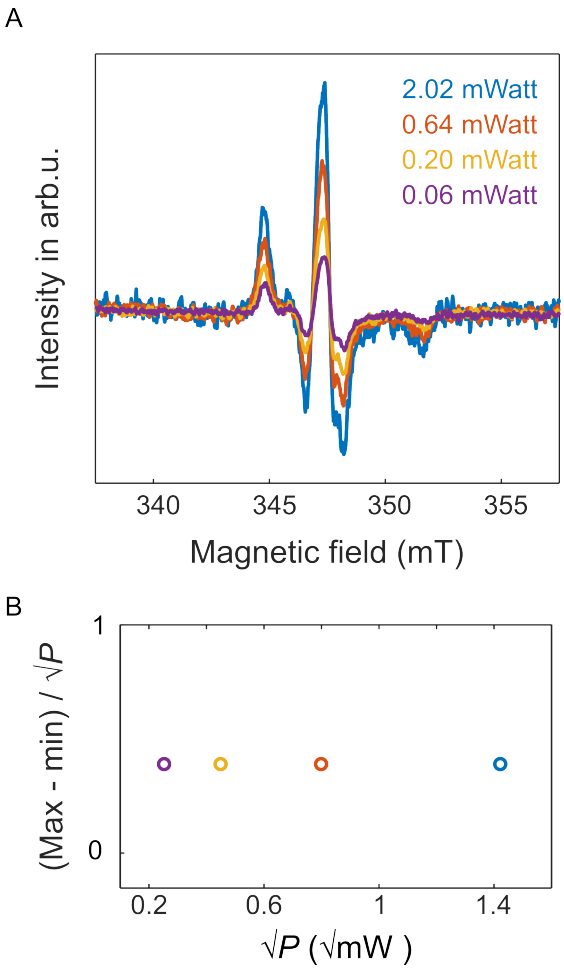

Figure 2.3: Microwave power saturation behavior of SL5 labeled at site 12. A. Spectra collected at different microwave power. B. Difference between the max-to-min intensity of each spectrum normalized to square-root of corresponding microwave power ($\sqrt{P}$).

Fig. 2.5. The measured K_d of the unlabeled SOMAmer is 6 pM (indicated on the left in Fig. 2.5). No spin-labeled construct binds to PDGF as tightly as the unlabeled parent SOMAmer. Based on a previously obtained crystal structure of SL5–PDGF complex, the labeling sites structurally fall into three domains: a direct binding domain, an indirect binding domain and a non-binding domain.[26] Incorporation of a spin label into any site in the non-binding domain (yellow) does not significantly disrupt the interaction since all K_d values in this region are under 100 pM. For the direct and indirect binding domains (purple and blue, respectively), no clear correlation

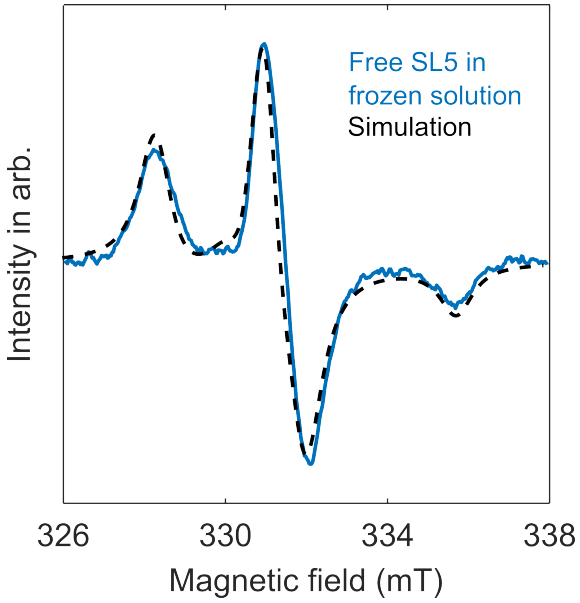

Figure 2.4: Frozen-solution CW spectrum of site 1 labeled-SOMAmer. Microwave frequency: 9.29649 GHz. Experimental temperature: 175 K. Simulation parameters: g = [2.0068(3) 2.0085(2) 2.0023(1)], A = [21.79(3), 12.43(2) , 103.01(2)] MHz, Gaussian and Lorentzian peak-to-peak linewidths = [0.05 0.02] mT.

between the physical location and the magnitude of K_d degradation is observed. Some sites are highly disruptive (e.g. 18 and 23), whereas others (12, 13, 16) have K_d values similar to those with labelled sites in the non-binding domain. For the purpose of selecting optimal labeling sites for NV center detection, any construct with a K_d larger than 6 nM (1000-fold reduction compared to parent construct) was deemed too disruptive and excluded from further analysis. Site 29 was excluded as well, as spin labeling at this site was unsuccessful.

2.3.2 EPR measurements and rotational mobility analysis

To magnetically detect protein binding with the spin-labelled SOMAmers in solution, room-temperature EPR spectra were recorded before and after protein binding as shown in Fig. 2.6. The change in spectral shape is significant and is due to a change in the overall molecular size. This demonstrates the feasibility of this EPR-based solution binding assay. To mimic a diamond surface for potential optical readout of this assay, 19 biotinylated constructs that passed the

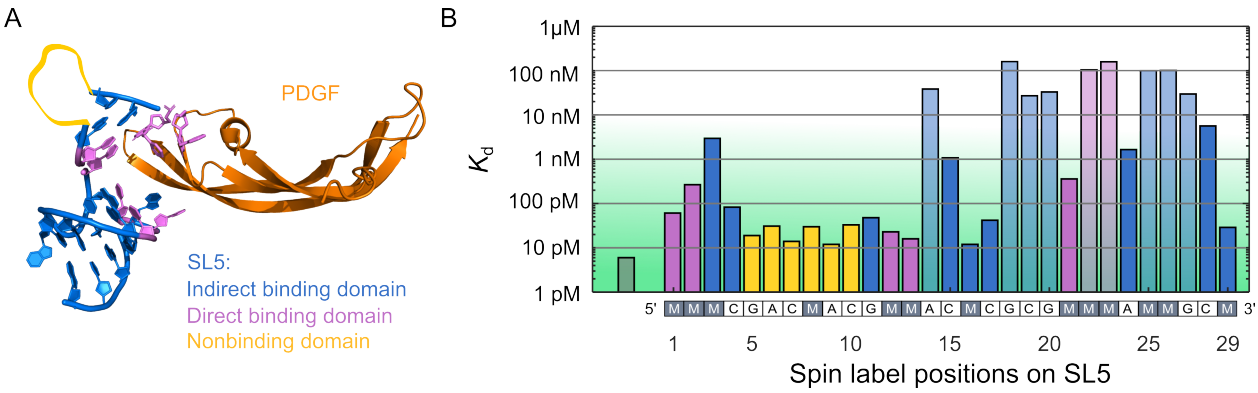

Figure 2.5: Evaluation of the binding affinity of spin-labeled SL5. A. A single SL5–PDGF-B complex from the crystal structure (PDBID 4hqu)[26] B. Binding affinity assay of SL5 spin-labeled at all nucleotides. The bottom row indicates the nucleotide sequence in the unlabeled construct, where "M" represents any non-canonical nucleotide. The K_d of unlabeled construct is 6 pM, indicated on the left in gray. The typical error in $\log_{10}(K_d)$ is about ±0.15, i.e. an overall uncertainty for K_d is a factor of 2. The green shaded region represents the acceptable range (under 6 nM) with opacity representing tightness of binding. Sites with low affinity (paler color bars) were excluded from subsequent EPR measurements.

binding affinity screening were ligated to streptavidin-coated agarose beads. This suppresses the global tumbling of the entire SOMAmer or SOMAmer–protein complex and isolates the rotational motion of the spin label as indicated in Fig. 2.7. Again, spectra were recorded in the absence and presence of target protein as presented in Fig. 2.6. All spectra were analyzed as described above, and rotational correlation times τ_c were determined for all sites and reported in Table A.2). Figure 2.8A shows an example using the construct labeled at site 12. Spin label rotational diffusion slows down after addition of the target protein PDGF as indicated by the broadening of the spectral lineshape in the low-field region around 346 mT (indicated by an arrow). This region of the spectrum corresponds to the $m_I = +1$ manifold of the ^{14}N nucleus of the nitroxide. Additionally, the high-field edge of the spectrum at about 351 mT sharpens slightly. Least-squares fits of simulated spectra to the experimental data reveal a significant increase in τ_c. The results for all sites, shown in Fig. 2.8C, indicate that significant changes in τ_c are observed for many sites.

To evaluate the possible change in τ_c from non-specific bindings, control experiments were

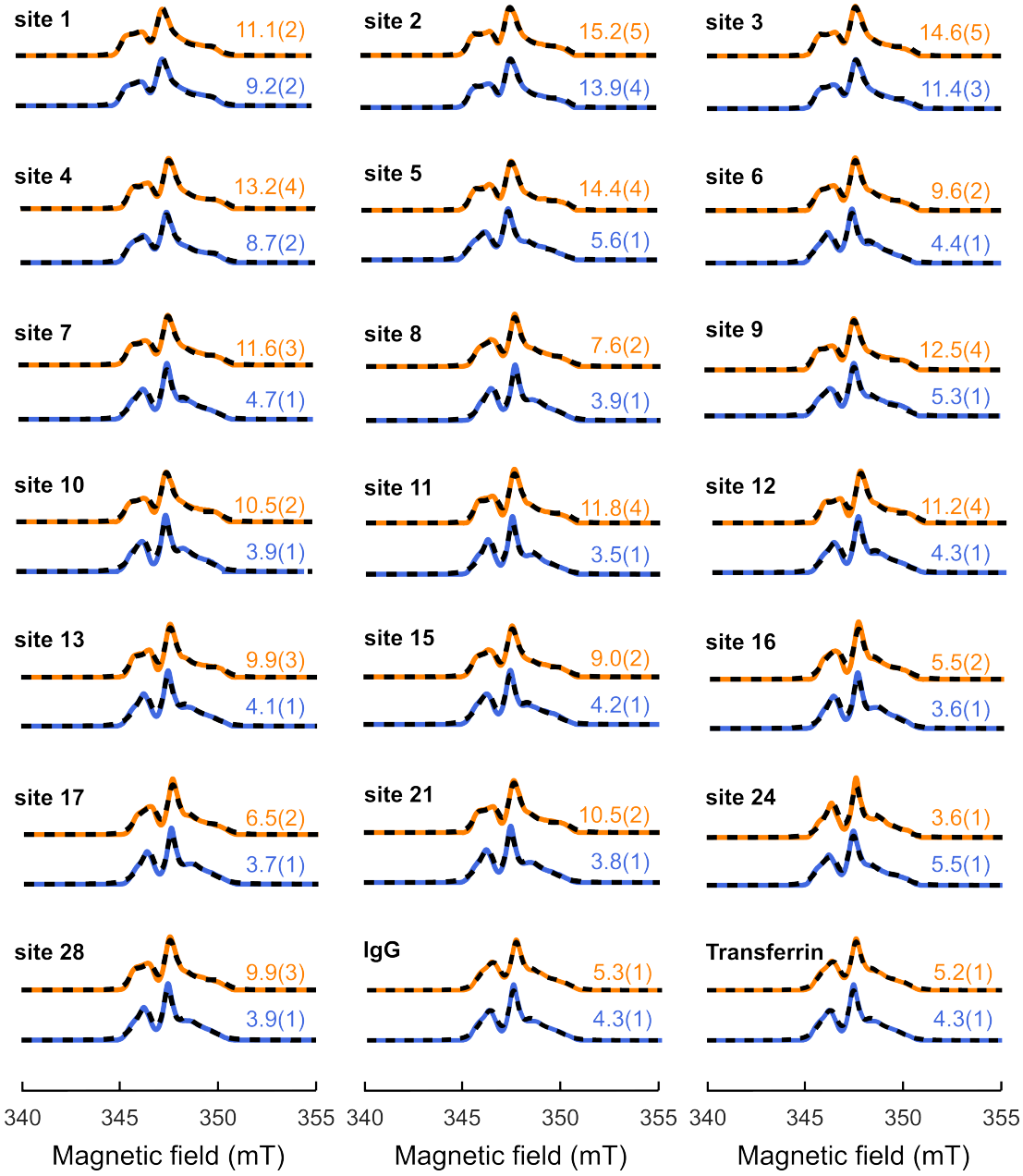

Figure 2.6: Integrated EPR spectra of all spin-labeled constructs of SL5. The simulations (dotted black line) are overlaid with the experimental apo (orange) and holo (blue) spectra. The corresponding fitted τ_c values are listed with the associated uncertainties.

performed using the SOMAmer construct labeled at site 12 and two different non-target proteins: immunoglobulin G (IgG) and transferrin. The two non-target proteins were chosen for

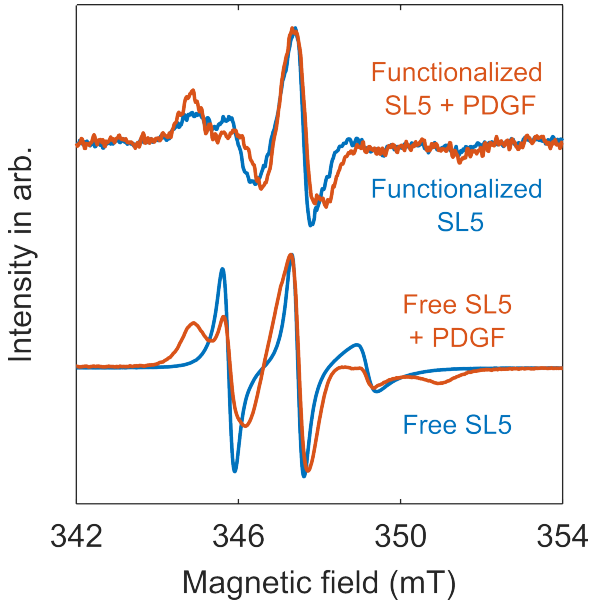

Figure 2.7: EPR spectra of SOMAmer SL5 in different motional regimes. A. EPR spectra of bead-attached streptavidin-functionalized (top) and free (bottom) SL5 labeled at site 12. The sharper peaks in the spectra of free SL5 (bottom) are indicative of global tumbling of the SOMAmer or SOMAmer–protein complex. The functionalized SOMAmer spectrum is noisier due to lower spin concentration, limited by the loading capacity of agarose beads.

their high abundance in human blood plasma.[7] The results shown in Fig. 2.8B indicate that the addition of non-target proteins do not significantly change τ_c. Small shifts are observed at the maxima of the holo spectra of PDGF and non-target proteins, possibly indicating changes in the g-tensor of the electron spin. The shifts could be attributed to the changes in the hydrogen-bonding environment around the nitroxide group of the spin label.[18] The slight increase in fitted τ_c from the apo to the holo state of the control experiments may be a result of the simple model used in the fitting.

To compare both binding affinity and mobility changes observed from all sites, Fig. 2.9 plots the values of τ_c before and after protein binding for all constructs along with their K_d as measured by the binding affinity assays. The experimentally determined τ_c are indicated by the corresponding markers, and the length of the arrow represents the magnitude of change in τ_c (denoted as $\Delta\tau_c$) after addition of protein. For the experiments using the target protein PDGF,

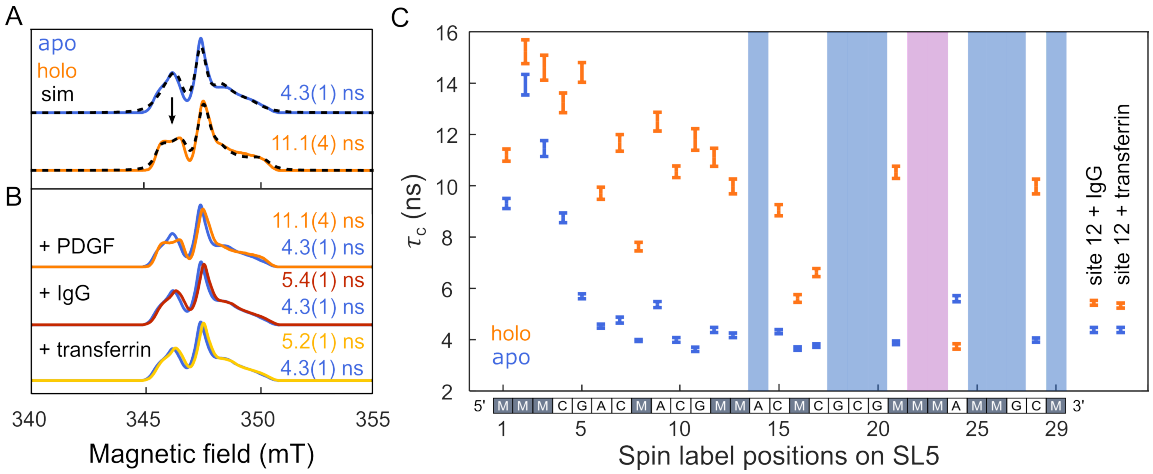

Figure 2.8: Evaluation of the mobility change of spin-labeled SL5 upon protein binding. A. An example of the integrated spectra for the apo (blue) and holo (orange) states of SL5 labeled at site 12 with simulated lineshapes obtained by fitting a rotational diffusion model. Fitted τ_c values are given in corresponding colors. The black arrow marks the feature that is most indicative of the mobility change. B. Control experiments using site 12 with non-target proteins IgG (red) and transferrin (yellow). C. Fitted τ_c values of for the apo and holo states of all EPR-evaluated constructs and for two non-target protein controls. The excluded sites are indicated by shaded columns with colors corresponding to Fig. 2.5.

sites 1, 2, 3 and 16 have the smallest $\Delta\tau_c$, whereas sites 5, 7, 9 and 11 have the largest. Site 24 is the only one that shows a decrease of rotational mobility upon binding; nonetheless, the difference is relatively small. Optimal labeling sites should have a large $\Delta\tau_c$ and a small K_d. Sites 5, 7, 9 and 12 best fit these criteria. Similar to the binding affinity screening results, there is no obvious correlation between the magnitude of rotational mobility change and the physical location of the labeling site since sites 5, 7 and 9 are all in the non-binding domain, and sites 12 and 13 are in the direct binding domain.

Overall, the results indicate that spin labels can be used as reporters of SOMAmer–protein binding and can therefore form the basis of protein sensors with high sensitivity and specificity.

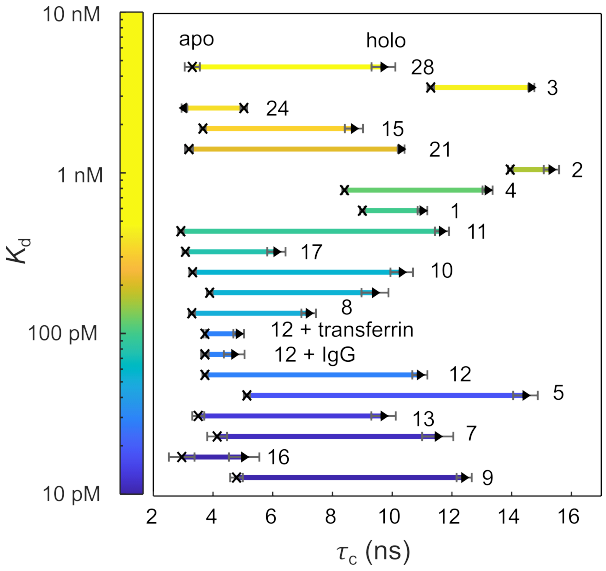

Figure 2.9: Evaluation of the performance of all spin-labeled SOMAmer constructs based on K_d (vertical axis) and τ_c (horizontal axis). The magnitude of the difference in τ_c between the apo (×) and holo (▶) states is indicated by arrow length, and the corresponding K_d values are indicated by arrow color according to the color bar on the left.

2.4 Extending the solution-based protein assay to NV center applications

Next, we explore how the EPR-detected SOMAmer protein binding assay demonstrated above can be combined with fluorescence detection via diamond NV centers. Having experimentally determined the rotational correlation times τ_c, we can estimate the effect of protein binding on the T_1 relaxation time of an NV center in proximity to the spin-labeled SOMAmer using a previously published model.[80,140] In this model, the total T_1 relaxation rate of an NV center in proximity to a spin label is a sum of three independent contributions:

$$\frac{1}{T_1} = \frac{1}{T_1^0} + \frac{1}{T_1^{\mathrm{rot}}} + \frac{1}{T_1^{\mathrm{rlx}}}. \tag{2.1}$$

Here, $1/T_1^0$ is the NV center's intrinsic spin–lattice relaxation rate in the absence of the spin label, $1/T_1^{\mathrm{rot}}$ is the contribution from the rotational dynamics of the spin label, and $1/T_1^{\mathrm{rlx}}$ is the contribution from the spin label's own intrinsic spin relaxation dynamics.

The first term depends on temperature,[27,64] diamond surface quality,[45,93,109] depth of NV center from surface,[16,99] and the spin environment,[92] especially the ^{13}C concentration in the diamond lattice.[10,91] For a single NV center implanted in a ^{12}C isotopically purified diamond, T_1^0 can be as long as several milliseconds[16,23,107] at room temperature, whereas bulk NV centers in nanodiamonds may have T_1^0 as short as hundreds of µs at room temperature.[27,80,98]

The second term represents the effect of a fluctuating magnetic field at the NV center due to the rotational diffusion dynamics of the spin label, mediated by the dipolar coupling between spin label and NV center. At the appropriate frequency, this fluctuating field induces transitions at the NV center. The associated transition rate is given by

$$\frac{1}{T_1^{\text{rot}}} = 3\gamma_{\text{NV}}^2 B_{\perp,\text{rot}}^2 J_{\tau_c}(\omega_{\text{NV}}), \tag{2.2}$$

where γ_{NV} is the gyromagnetic ratio of the NV center, $B_{\perp,\text{rot}}$ is the averaged magnetic field generated by the spin label in the plane perpendicular to the magnetization direction of the NV center, and $J_{\tau_c}(\omega_{\text{NV}})$ is the spectral density of the rotating spin label evaluated at ω_{NV}, the angular frequency for the $m_S = 0 \leftrightarrow \pm 1$ transition of the NV center. The full derivation of this relation is given in Appendix A.3.

$B_{\perp,\text{rot}}^2$ is given by

$$B_{\perp,\text{rot}}^2 = \frac{1}{4}\left(\frac{\mu_0}{4\pi}\hbar\gamma_{\text{SL}}\right)^2 \frac{2+3\sin^2\theta}{r^6}, \tag{2.3}$$

where μ_0 is the vacuum magnetic permeability, γ_{SL} is the gyromagnetic ratio of the spin label, r is the distance between the spin label and the NV center, and θ is the angle between the magnetization direction of the NV center in a weak external magnetic field and the NV–spin label direction. Via r and θ, $B_{\perp,\text{rot}}^2$ contains the geometry dependence of $1/T_1$: the rate drops off rapidly with increasing distance, but is only mildly orientation dependent as the θ term varies beween 2 for $\theta = 0$ and 5 for $\theta = \pi/2$.

The spectral density in Eq. 2.2 is given by

$$J_{\tau_c}(\omega) = \frac{\tau_c}{1+\tau_c^2\omega^2}, \tag{2.4}$$

and represents the fluctuating field amplitude as a function of frequency ω. Its value at $\omega = \omega_{NV}$ is used in Eq. 2.2.

The third term in Eq. 2.1 is the contribution from the relaxation dynamics of the spin label, which is relayed to the NV center by the same mechanisms as the second term. It contains several separate contributions:[51,58]

$$\frac{1}{T_1^{rlx}} = \left(\frac{\mu_0}{4\pi}\right)^2 \gamma_{NV}^2 \gamma_{SL}^2 \hbar^2 \frac{1}{r^6}\left(\frac{1}{6}B + 3C + \frac{3}{2}E\right), \tag{2.5}$$

$$B = \frac{T_{2,SL}}{1+(\omega_{NV}-\omega_{SL})^2 T_{2,SL}^2}(1-3\cos^2\theta)^2, \tag{2.6}$$

$$C = \frac{T_{1,SL}}{1+\omega_{NV}^2 T_{1,SL}^2}\sin^2\theta\cos^2\theta, \tag{2.7}$$

$$E = \frac{T_{2,SL}}{1+(\omega_{NV}+\omega_{SL})^2 T_{2,SL}^2}\sin^4\theta, \tag{2.8}$$

where ω_{SL} is the (angular) transition frequency of the spin label electron, and $T_{1,SL}$ and $T_{2,SL}$ are the spin–lattice and spin–spin relaxation times of the spin label, respectively. Each of the three terms B, C and E is a product of a spectral density (depending on $T_{1,SL}$ or $T_{2,SL}$) and an angular term. Given a reasonable NV–spin label geometry (r = 6 nm and $\theta = 45°$) and typical ranges of relaxation times of nitroxides, 0.3 to 3 µs for T_1 and 0.1 to 1 µs for T_2,[34,117] values for $1/T_1^{rlx}$ are significantly smaller than the T_1^0 relaxation rate (details are discussed in Appendix A.2). Therefore, the $1/T_1^{rlx}$ term is negligible and is dropped from now on.

Figure 2.10 elaborates on the dynamic and geometric aspects of $1/T_1^{rot}$. Figure 2.10A illustrates the effect of τ_c for a fixed NV–spin label geometry (r and θ). The top panel shows estimated NV T_1 as a function of spin label τ_c from 0.01 ns to 50 ns, using the first two terms in Eq. 2.1 with T_1^0 = 3.5 ms, r = 6 nm and $\theta = 45°$. The bottom panel shows the spectral density from Eq. 2.4 as a function of τ_c. The spectral density can be used to infer the magnitude of

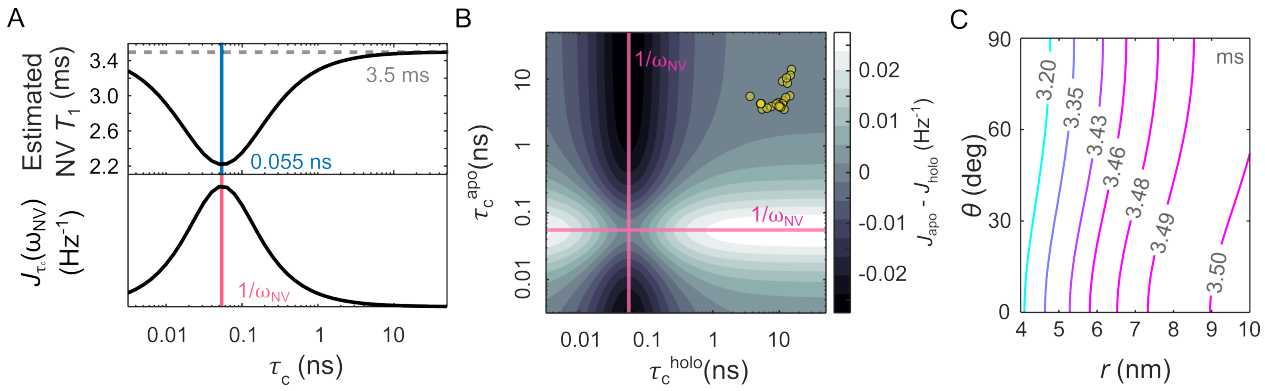

Figure 2.10: The predicted dependence of NV center T_1 on measured τ_c. A. Simulating the T_1 of the NV center as a function of τ_c. Top: estimated T_1 of an NV center 6 nm from the spin label, with a fixed angle $\theta = 45°$. Blue solid line: the minimum T_1 at $\tau_c = 0.055$ ns. Gray dotted line: the intrinsic T_1 of the NV center in the absence of a spin label, T_1^0. Bottom: the spectral density evaluated at ω_{NV}. Pink solid line: the maximum of the spectral density at $\tau_c = 1/\omega_{NV}$. B. The change in spectral density at ω_{NV} as a function of and apo and holo τ_c. The color bar indicates the differences between density amplitudes at two τ_c values. Yellow dots: τ_c values of apo and holo states of SL5 constructs. Pink solid line indicates $1/\omega_{NV}$. C. T_1 (ms) of the NV center a function of NV center–spin label distance and orientation. The contour lines represent NV center T_1 in the presence of a mobile spin label with $T_1^0 = 3.5$ ms and $\tau_c = 4$ ns at a location specified by distance r and angle θ.

T_1 reduction. The density amplitude quantifies the transition rate at the NV center due spin label reorienting at different rates. To isolate the dynamics of the spin label from the geometric factors, Fig. 2.10B illustrates the effect of the τ_c values for the apo and the holo states on the change in spectral density (which is proportional to the change in relaxation rate). A large change in spectral density will enhance T_1 contrast. The largest spectral density changes occur if one of τ_c^{apo} and τ_c^{holo} is close to $1/\omega_{NV}$ and the other is at least an order of magnitude slower or faster (white and black regions in Fig. 2.10B). The apo/holo τ_c values for SL5–PDGF are shown by the cluster of yellow dots. The τ_c values of apo and holo state range from 2.5-5 ns and 6-16 ns, respectively. They do not fall within the most sensitive range. One approach to improve upon this is to build more flexible linkers into the structure by exploring a wider range of spin label structures and coupling chemistries.

Figure 2.10C visualizes the dependence of T_1 on the relative position of the NV center spin

and the nitroxide spin for a fixed τ_c. According to Eq. 2.3, T_1^{rot} contains an angular dependence and a factor of $1/r^6$, and the relaxation enhancement is most pronounced if the spin–spin distance is short and the angle θ perpendicular. The contour plot shows T_1 using $T_1^0 = 3.5$ ms and $\tau_c = 4$ ns. The reduction in T_1 increases as the angle θ approaches 90° and decreases with increasing distance. This is an important aspect for combining the spin-labeled SOMAmer assay with a diamond sensor since both orientation and distance affect the sensitivity of the T_1 relaxation-based sensing mechanism.

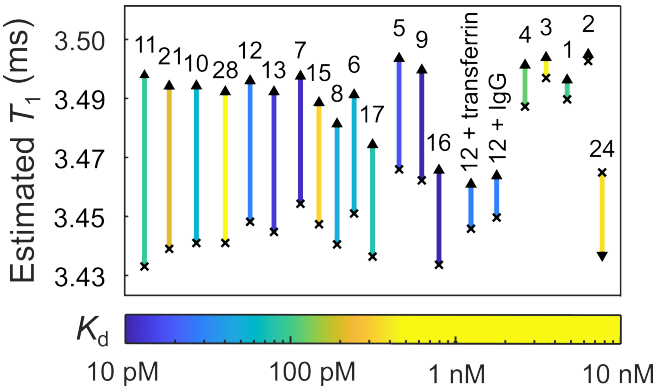

Figure 2.11: Evaluating the estimated $T_{1,\mathrm{NV}}$ for all tested sites, assuming $r = 6$ nm and $\theta = 45°$. The magnitude of the difference in $T_{1,\mathrm{NV}}$ between the apo (×) and holo (▲) states is indicated by arrow length, and the corresponding K_d is indicated by arrow color with a reference in Fig. 2.9.

To evaluate the reduction of T_1 relaxation rate due to the protein binding-induced changes in rotational mobility for spin-labelled SL5, T_1 values are estimated for all sites using the same geometry ($r = 6$ nm and $\theta = 45°$) as used in Fig. 2.10A. The calculated results are ranked from the largest to the smallest binding-induced T_1 change from left to right in Fig. 2.11. In this geometry, the construct labelled at site 11 produces the largest contrast in T_1, followed by sites 21 and 10. However, sites 5, 7, 9 and 12, which yield the largest differences in τ_c, are not among the highest-ranked sites in terms of T_1 contrast. This is because the apo state τ_c of these constructs are longer than those of sites 11, 21 and 10 (Fig. 2.9), resulting in a shorter window of $\Delta\tau_c$ as illustrated by Fig. 2.10A.

The estimated ΔT_1 ranges from 0.05 ms (site 11) to less than 0.01 ms (site 1 through 4). Recent work has demonstrated a reliable resolution of 100 µs using nanodiamonds.[122] Several publications also managed to distinguish ΔT_1 values of hundreds of ms to tens of µs.[14,42,53,98] The SL5-PDGF binding-induced reduction of the estimated NV center ΔT_1 falls in a range that can be detected by current NV center sensor devices.[80,81,130,140,151,153] Nevertheless, several strategies can be applied to increase T_1 contrast and therefore the overall sensitivity of the NV center relaxometry.

NV center T_1 relaxometry detection sensitivity is strongly limited by the NV–spin label distance due to the steep $1/r^6$ dependence in Eq. 2.3. Therefore, keeping r as short as possible is crucial. The depth of the NV center below the diamond surface can be engineered via tuning the energy of ion implantation.[4,43] The caveat is that shallow NV centers are often susceptible to magnetic noise from surface spins.[93,107,109] Another approach to potentially increase ΔT_1 is to shorten the spin label linker length by using alternative labeling chemistries such as coupling of azide-functionalized spin labels with terminal alkynes[146] or strained cycloalkynes,[78] or by ligation to the phosphate group,[104] the sugar[36] and the base.[60,77,86,142] A series of rigid spin labels that can be covalently conjugated to the base were designed for measuring the flexibility of DNA;[52,69,85,86,89,95] however, these labels are less useful in this context, as their rigidity prevents the detection of spin label mobility changes. The τ_c screening protocol reported in this work relies on the built-in mobility from the rotatable bonds in the linker (Fig. 2.1B). In addition to linker length and rigidity, linker size is another critical aspect. An inflexible and bulky linker may have greater potential to disrupt binding interactions in comparison to a small and compact structure. The ideal linker would be short but flexible so that the spin label is close to the SOMAmer and responsive to protein binding, but can still span a wide dynamic range of rotational motion.

The affinity of SOMAmer–protein binding may affect the overall sensitivity of the NV center detection. This effect is difficult to isolate and must be evaluated with the changes in spin label mobility upon protein binding. However, the SOMAmers may undergo conformational changes when binding to target proteins, potentially leading to distance changes. According to

Eq. 2.3, the effect from a distance change can be as dramatic as the effect from a change in τ_c. The distance change may counteract or enhance the effect of the τ_c change on T_1. Further investigations of SOMAmer structure and conformational landscapes, also in the context of their attachment to a diamond surface,[148] will provide more information on probable distance effect.

2.5 Conclusions and future direction

We developed a novel protocol for sensing proteins using immobilized site-specifically spin-labeled SOMAmers in combination with CW EPR spectroscopy to detect changes in spin label rotational mobility upon protein binding. A full site scan on the benchmark SOMAmer SL5 and its target protein PDGF-BB revealed a number of suitable sites where (a) the binding-induced change in rotational mobility is significant and (b) the reduction in binding affinity due to the presence of the spin label is small. The approach presented here is general and can be extended to other SOMAmer–protein pairs.

In addition, we modeled the detection of the observed rotational mobility changes via T_1 relaxometry of a proximal diamond NV center, which provides a platform for increased sensitivity and multiplexing. The results indicate several strategies for maximizing contrast in NV T_1. First, minimize T_1 in the unbound state by shortening the rotational correlation time to approach the inverse angular transition frequency of the NV center. Second, maximize the slow-down of τ_c experienced by the spin label upon protein binding. Both strategies can be pursued by varying the nature of the spin label and scanning across labeling sites. Also, the NV–spin label distance needs to be carefully controlled in order to maximize T_1 contrast.

Chapter 3

PROBING MILLISECONDS RESOLUTION OF PROTEIN DYNAMICS USING RAPID FREEZE-QUENCH AND EPR SPECTROSCOPY

Resolving the reaction mechanisms of macrobiomolecules often requires structural information before the molecular interaction reaches the equilibrium state. A sample preparation technique known as rapid freeze-quench (RFQ) can be used along side with EPR spectroscopy for obtaining time-resolution of the structural conversion of protein–ligand interaction. This chapter is focused on the instrumentation of a home-built RFQ device. The following sections begin with an introduction to RFQ (Section 3.1), followed by a review of selected literature with discussions of design criteria (Section 3.2). The home-built RFQ instrument was constructed (Section 3.3) and calibrated using a well-studied reaction (Section 3.4) and then used for probing the dynamics of the conformational change of maltose binding protein (MBP) (Section 3.5).

3.1 Background and motivation of RFQ technique

Understanding the mechanism of protein binding interactions often requires kinetic and structural information; however, direct measurement of such a process remains challenging. Experimental techniques such as stopped-flow absorption[88] and pulse-labeling mass spectrometry[59,72,75] have been used for kinetic analysis and studying protein folding mechanisms. In principle, these experiments monitor the change of population over time, but the structural information of participating chemical species may not be resolved.

An alternative strategy is to quench and preserve the state of a reaction at different time points before it reaches equilibrium. A technique known as rapid-freeze quench (RFQ) prepares samples by freeze-trapping an on-going chemical reaction as illustrated by Fig. 3.1A and B. The frozen samples capture the fraction of populations at the moment of quenching and

therefore can be used for determining the rate constant (Fig. 3.1C). In addition, the frozen samples can be used for further structural analysis, using the a variety of spectroscopic methods. The RFQ technique has been used in combination with X-ray,[133] Raman,[37,82] NMR,[66] and EPR[24,70,127,129,131,150] spectroscopy. The molecular systems that have been examined by such methods include cytochrome c,[22,56,129,135,150] peroxidase[40,74,136] and catalytic intermediates.[28,70,74,97,127,131,145]

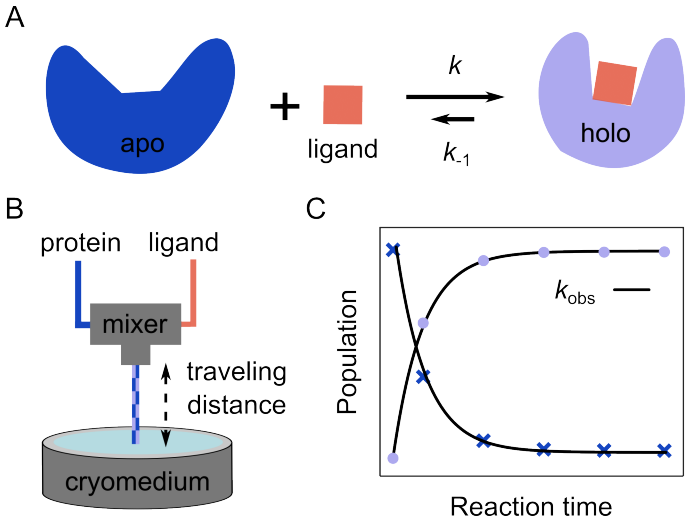

Figure 3.1: An overview of the RFQ technique. A. A two-state protein–ligand interaction with a rate constant k. B. A simplified diagram of a RFQ instrument. C. Schematic of kinetic analysis of using RFQ-samples prepared at different reaction time.

Early RFQ-EPR studies were mostly focused on metalloproteins since such proteins often have a paramagnetic metal center and therefore native unpaired electron spins. The scope of protein molecules that can be studied by this method is expanded by combining RFQ, SDSL and DEER spectroscopy, and several recent publications[49,57,113,114] have achieved obtaining information about protein conformational dynamics with temporal and structural resolution.

3.2 Existing RFQ designs

In order to perform the RFQ technique, a specialized instrument is required. A RFQ instrument usually has three components: a pump for driving the reagents, a mixer for initializing

the reaction, and a cryomedium for stopping the process by freezing the reacting solution. An ideal RFQ device should have a short instrumental dead time and a large window of accessible reaction times so that both the early stages and the end point of reactions can be captured. As illustrated in Fig. 3.1B, the reaction time is often adjusted by changing the traveling distance between the ejection nozzle of the mixer and the cryomedium where samples are frozen. The operational time ranges from hundreds of μs to ms, and the sample volume may range from 50-200 μL,[57,66] depending on the choice of implementation.

Two commercial RFQ devices, one from Update Instrument[84,94,111] and another from BioLogic,[32,100] have been reported in literature, and numerous papers featuring customized devices have been published. A home-built RFQ instrument gives the practitioners more freedom to mininize the instrumental dead time, maximize the operational range, and optimize the sample volume. These specifications depend on the downstream experimental setup, such as the microwave frequency of the EPR spectrometer and the resonator type. Several commonly used options for each component have been reported and discussed in literature and are summarized in Table 3.1. The rest of this section is focused on discussing the advantages and caveats of each reported design.

Table 3.1: A summary of different components used in customized RFQ devices reported in published work.

publication	**pump type**	**mixer type**	**cryofixation**	**reported deadtime**	**time axis calibration**
Bray(1961) [20]	mechanical hydraulic ram	Y-shaped plastic mixer	plunging	30 ms	unclear
Ballou(1974) and Palmer(1978) [11, 12]	mechanical hydraulic ram	four-way metal mixer	plunging	5 ms [11]	myoglobin–azide
Lin et al.(2003) [82]	syringe pump	nanofabricated silicon mixer	two rotating copper wheels	50 µs	myoglobin–azide
Tanaka et al.(2003) [136]	syringe pump	T-shaped metal mixer	two rotating copper wheels	120 µs	myoglobin–azide
Cherepanov and de Vries(2004) [24]	HPLC pump	four-way metal mixer [105]	plunging	137±18 µs	myoglobin–azide
Egawa et al. (2009) [37]	syringe pump	nanofabricated silicon mixer	two rotating copper wheels	50 µs	myoglobin–azide
Manzerova et al. (2011) [84]	commercial RFQ (Update Instrument)	Wiskind-type metal mixer [56]	two rotating copper wheels	5 ms	myoglobin–azide
Schmidt et al. (2011) [111]	commercial RFQ (Update Instrument)	silicon wafer mixer	plunging	unclear	unclear
Potapov and Goldfarb(2009), [102] Collauto et al. (2017) [25]	syringe pump	nanofabricated plastic mixer [25]	rotating cryo disc	10 ms, [102] 9 ms [25]	TEMPOL–dithionite +Mn(II) standard
Jeon et al.(2019) [66]	HPLC pump	Y-shaped HPLC mixer	rotating cryo disc	2.2 ms	calculated
Hett el al.(2021) [57]	HPLC pump	four-way tangetial metal mixer	plunging	68 µs	myoglobin–azide
Schroeter el al.(2022) [116]	commercial RFQ (Update Instrument)	commercial mixer	two rotating aluminum wheels	unclear	$Cu(Im)_4$–Cu(EDTA)

The pumps used on RFQ devices have evolved over the past decades. The earliest reported RFQ apparatus[20] was driven by a motorized linear ram. Syringe pumps (Figure 3.2) have been widely used in the past; however, such pumps are ultimately limited by the lack of a pressure control module and therefore the precise control of flow rate. Instead, HPLC pumps are the preferred choice since they are designed for pumping solutions through narrow tubings at a steady and precise flow rate.

Mixer performance is a popular area of interest in RFQ instrumentation. The design of a mixer usually aims to achieve fast and complete mixing by avoiding laminar flow. Microfluidic devices with twisted channel patterns are common choices. Such mixers are made out of silicon[37,82,111] or polymers[102] via photolithography. An alternative design is the all-metal four-way tangential mixer.[24,57] The four-way tangential mixer directs the two solutions into four opposite channels that lead to a central chamber with some placement offset for inducing more turbulence. A diagram of a typical tangential mixer is shown in Fig. 3.3A. The most accessible option is a T-shaped or Y-shaped mixer, which can be easily purchased from HPLC accessory vendors. To avoid insufficient mixing, due to fast laminar flow, Jeon et al.[66] packed stainless steel beads (O.D. = 40 μm) at the ejection port of the mixer to introduce turbulent flow.

In summary, the combination of the appropriate pump and mixing setup should result in a high-pressure high-speed solution jet of chemicals. To achieve this condition, the diameter of the mixer ejection port and the tubing connecting mixer to pump is usually tenth to hundreds of μm wide. A thinner ejecting solution jet is more likely to achieve homogeneous freezing times once the solution is deposited on/in a cryogenic environment. In almost all RFQ designs, the reaction time is varied by changing the distance between the mixer and the cryofixation medium.

Cryofixation and sample packing are sometimes overlooked but are critical aspects for obtaining high-quality data. The success and consistency of samples requires instant and uniform freezing rate so that water does not crystallize but vitrifies to an amorphous solid instead. The easiest approach to freeze a reaction is to plunge the solution jet directly into a liquid cryo bath of nitrogen, isopentane or ethane, which is also the cryofixation method implemented by the commercial RFQ devices; however, such a method may result in crystallization and splashing,

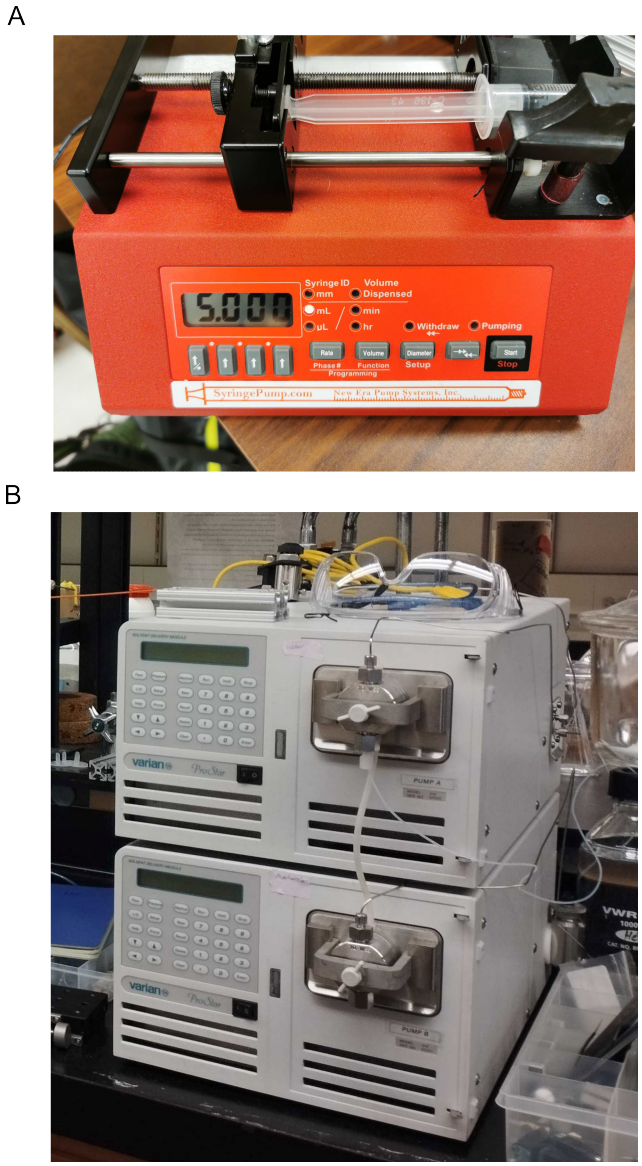

Figure 3.2: Common options of RFQ pumps. A. Syringe pump purchased from New Era Pump Systems Inc. B. Varian ProStar 210 HPLC pump.

which then lead to inhomogeneous freezing rates.[24] In addition, it is challenging to use this method with small sample volumes. Another popular approach is to eject the reaction solution in between two rotating metal wheels submerged in a cryo bath. The rotating wheels grind the frozen solution to fine powder as it freezes on the metal surface, creating a more homogeneous sample. A schematic of this design is shown in Fig. 3.4. To create a thin layer of uniform vitri-

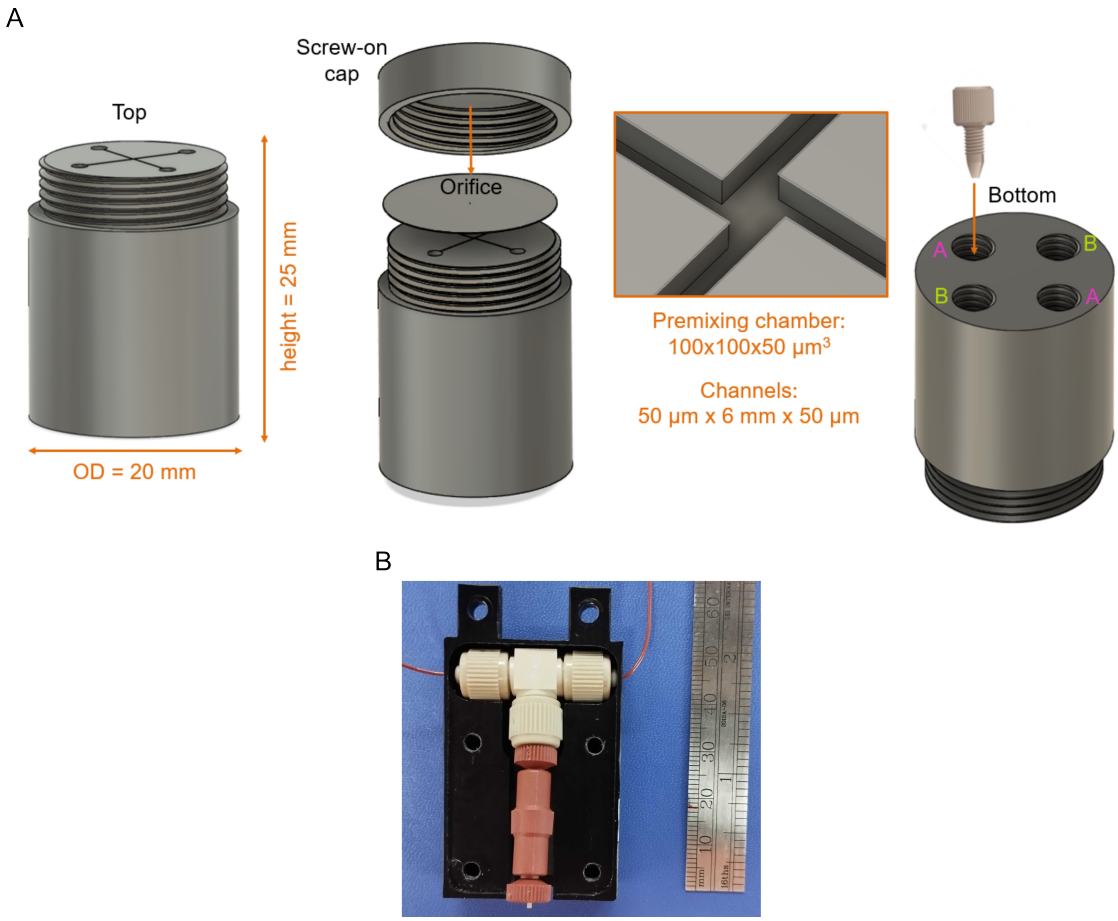

Figure 3.3: Two examples of RFQ mixers. A. A design diagram of a four-way tangential mixer. The design was replaced by using a commer T-shaped mixer. B. A commercial T-shaped mixer with auxiliary components. The details of this setup is further explained in Fig. 3.5 and Fig. B.1.

fied solution, another option is to deposit sample on a pre-cooled rotating disc. This method is usually accompanied with a electric motor,[25,66,102] which sweeps the sample mixer across the entire plate to use the entire surface of the disc.

3.3 Construction and operation of the home-built RFQ instrument

Considering the overall cost, feasibility and ease of operation, a home-built RFQ device based on the model presented in Jeon et al.[66] was constructed with several additional modifications. An schematic flow diagram is shown in Fig. 3.5. Figure 3.5A shows the fluidic sys-

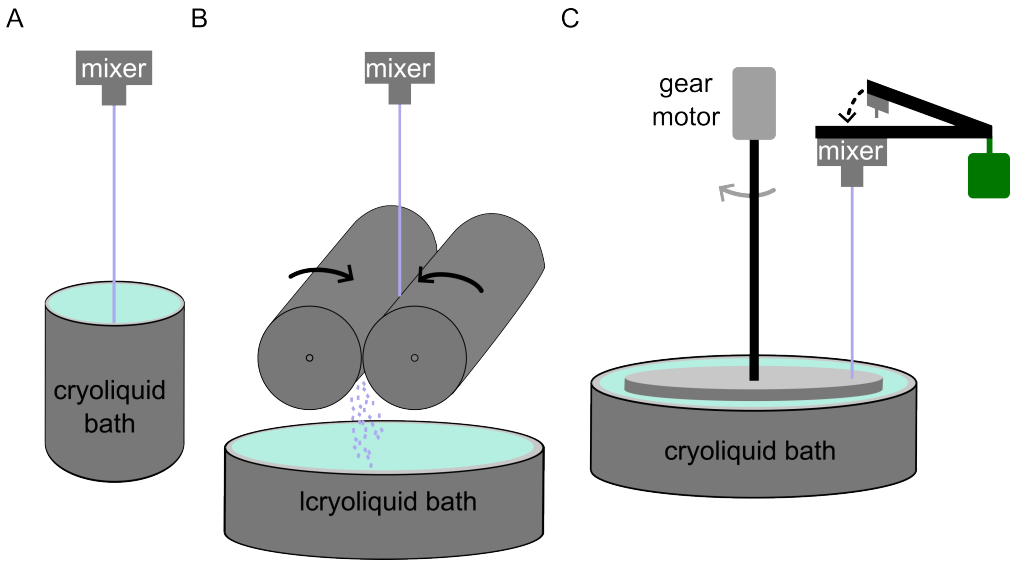

Figure 3.4: Schematic diagrams of cryofixation methods. A. Direct plunging. B. Grinding frozen samples by rotating wheels. C. Depositing sample across a rotating cryo disc. This method is implemented in the home-built instrument (Fig. 3.5).

tem. The HPLC pump (Varian, ProStar 210) pumps buffer solution through the gray tubings and supplies steady pressure to the rest of the fluidic system. The buffer solution enters the injector (Rheodyne, 7010). The injector switches between two modes: standby and injection. The standby mode directs buffer solution to a T-shaped mixer and then to waste. The standby mode tubing connection is built to mimic the injection mode tubing connection to maintain stable and similar pressure between the two modes, which intends to maintain a steady flow rate when switching between two modes. The injection mode is connected to the 200 μL sample loops (IDEX Health Science, 9055-025), one for ligand (Figure 3.5B, red) and one for protein (Figure 3.5B blue). The loading loops are connected to filters (IDEX Health Science, A-431) to remove particulates in the sample solutions. The filters are then connected to tubings with an inner diameter of 127 μm and outer diameter of 1/32"(IDEX Health Science, A-431). Switching the 1/16" sample loop tubing to the 1/32" tubings increases the fluid pressure and therefore the linear flow rate, and the latter is compatible with a T-shaped mixer (IDEX Health Science, P-885) designed to handle up to 5000 psi pressure. The pump and sample loops are kept on a

lab bench at room temperature. A photo of the entire setup is shown in Figure B.2.

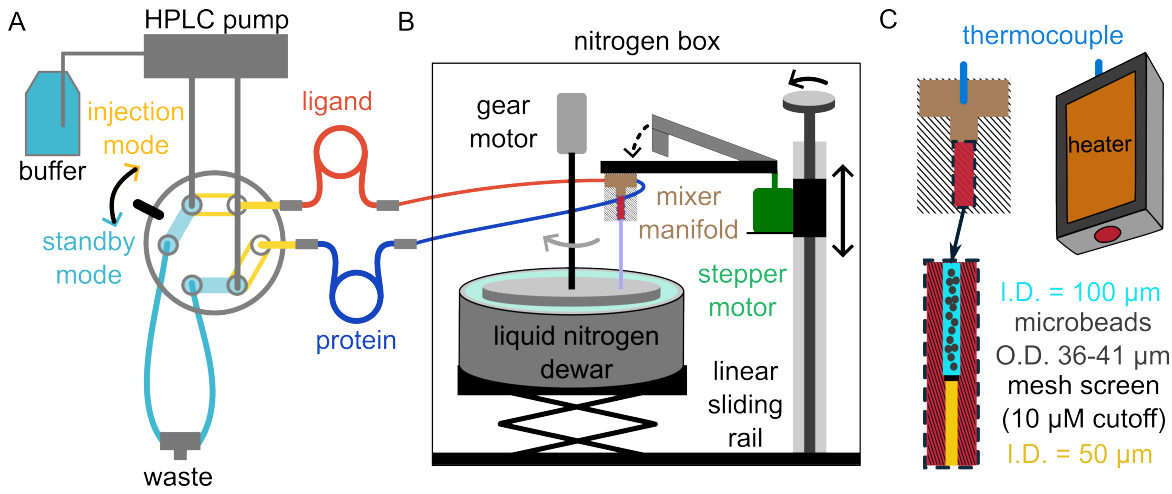

Figure 3.5: Flow diagram of the home-built RFQ instrument. A. The fluidic system. B. Components housed in a temperature-regulated dry nitrogen box. C. Details of the mixer and temperature-controlled mixer manifold.

The 1/32" tubings lead to the mixer and cryomedium setup housed in a acrylic box as shown in Figure 3.5B. The acrylic box is purged with dry nitrogen gas during operation to reduce the humidity to avoid water condensation on the sample collection surface. When the setup is in operation, the reaction solution comes out the mixer as a jet and is sprayed on an aluminum wheel rotating at 300 rpm. A gear motor (Greartisan, 24 V DC motor) and a customized pulse width modulation unit (XY-LPWM) were used together to maintain specific speed of the rotating wheel if needed. To avoid inhomogeneous freezing rates, the mixer sweeps across the aluminum wheel during sample deposition, creating a thin layer of solid sample (Figure 3.4). The total sample deposition time may be varied depending on the volumetric flow rate set by the HPLC pump and is approximated by equation:

$$\frac{\text{protein sample volume} + \text{ligand sample volume}}{\text{deposition time}} = \text{volumetric flow rate.} \tag{3.1}$$

For example, the calculated sample deposition time is 12 seconds if 200 μL protein solution and 200 μL ligand solution are mixed by a 2 mL/min volumetric flow rate. In operation, the sweep

time of the stepper motor (StepperOnline, 17HM19-2004S) is usually shorter than the calculated total sample deposition time to avoid spraying buffer on cyromedium, which would dilute the spin concentration and reduce sensitivity. The aluminum wheel is pre-cooled in a liquid nitrogen bath on a lab jack stand. The wheel remains cold during the entire sample collection packing period, which last around 2-3 minutes on average. The stepper motor is controlled by a digital stepper drive (StepperOnline, DM542T), an Arduino Uno R3 board. As mentioned in previous discussion, the RFQ device should be able to quench reaction at different time points. The reaction time is varied by changing the distance between the mixer and the aluminum wheel. The stepper motor that controls the mixer sweeping motion is mounted on a ball screw linear sliding rail, which moves vertically by a hand wheel on top.

Following by the method presented in Jeon et al.,[66] stainless steel micro beads with diameters ranging from 37 to 41 μm (Cospheric, SSMMS-7.8 35-41um) were packed into the mixer to ensure sufficient mixing between the two solutions. The details of the setup are schematically shown in Figure 3.5C, where the beads are hosted in the mixing region and blocked by a 10 μm mesh screen (Valco Instruments, 10SR.5-10). A photo of the mixer and mixer manifold is presented in Figure B.1. The temperature of the mixer is regulated to match the room temperature outside the nitrogen box where the samples are stored before mixing. The temperature inside the nitrogen box is difficult to control and stabilize because of nitrogen boiling. A heat gun is used during operation to prevent severe differences between the box air temperature and the mixer temperature.

3.4 Calibrating the time axis of the home-built RFQ device

To obtain reliable kinetic data from RFQ-prepared samples, it is good practice to experimentally determine the absolute reaction time and operational time range of the instrument. This section is focused on using the aforementioned (Table 3.1) myoglobin–azide reaction to calibrate the home-built RFQ device.

The binding interaction between myoglobin–azide is well-characterized[24] and is the most widely used calibration reaction for X-band EPR applications.[57,94,100] The reaction converts the

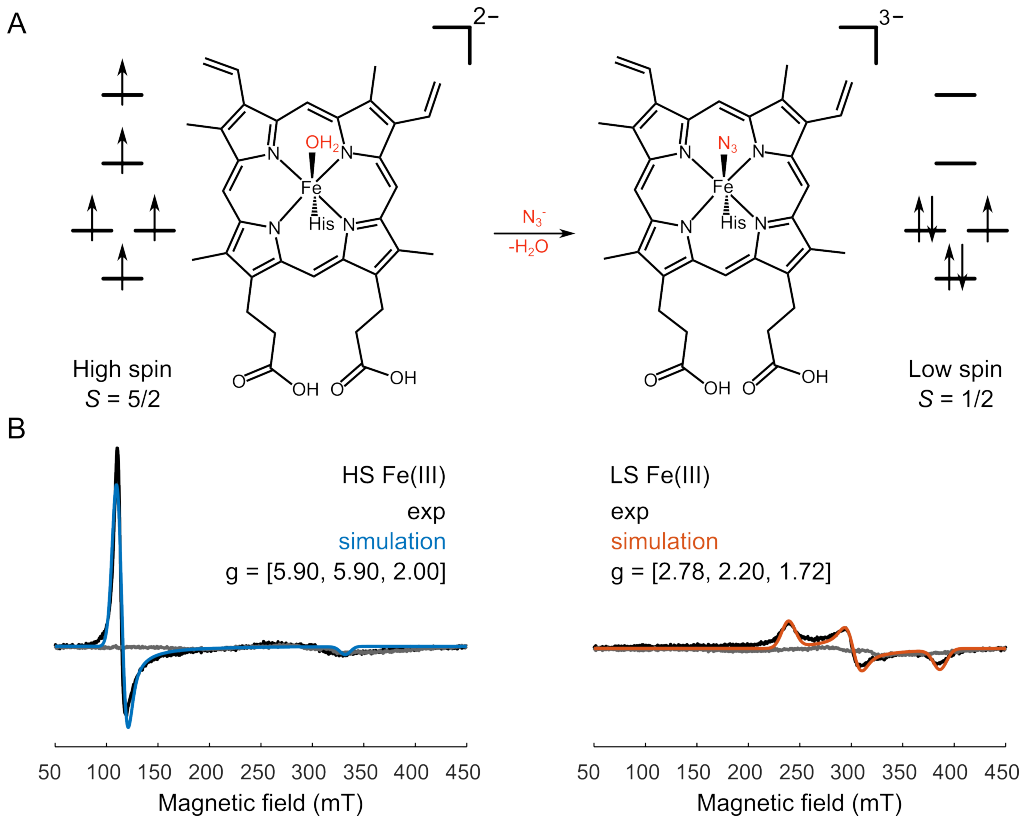

Figure 3.6: The conversion of spin states in myoglobin–azide binding interaction. A. Electron configurations of $S = 5/2$ Fe(III)(left) and $S = 1/2$ Fe(III)(right). B. Corresponding X-band EPR spectra. The gray line is the background signal measured under the same experimental condition.

heme center from a high spin (HS) $S = 5/2$ Fe(III) to a low spin (LS) $S = 1/2$ Fe(III) as shown in Fig. 3.6A. The shift of the spin states exhibits distinctive features in X-band EPR spectra. Figure 3.6B shows the unbound HS myoglobin spectrum and the azide-bound LS myoglobin spectrum. The zero-field splitting in the Fe(III) $S = 5/2$ system is too large to be observed at X-band frequency experiments,[124] therefore the HS spectrum is treated as an effective $S = 1/2$ species with an axial effective $\boldsymbol{g}$-tensor, featuring a sharp peak at $g = 5.9$ and a dip at $g = 2.0$. The LS Fe(III) has a rhombic $\boldsymbol{g}$ ($g = [2.78, 2.20, 1.72]$) at higher magnetic field. In the presence

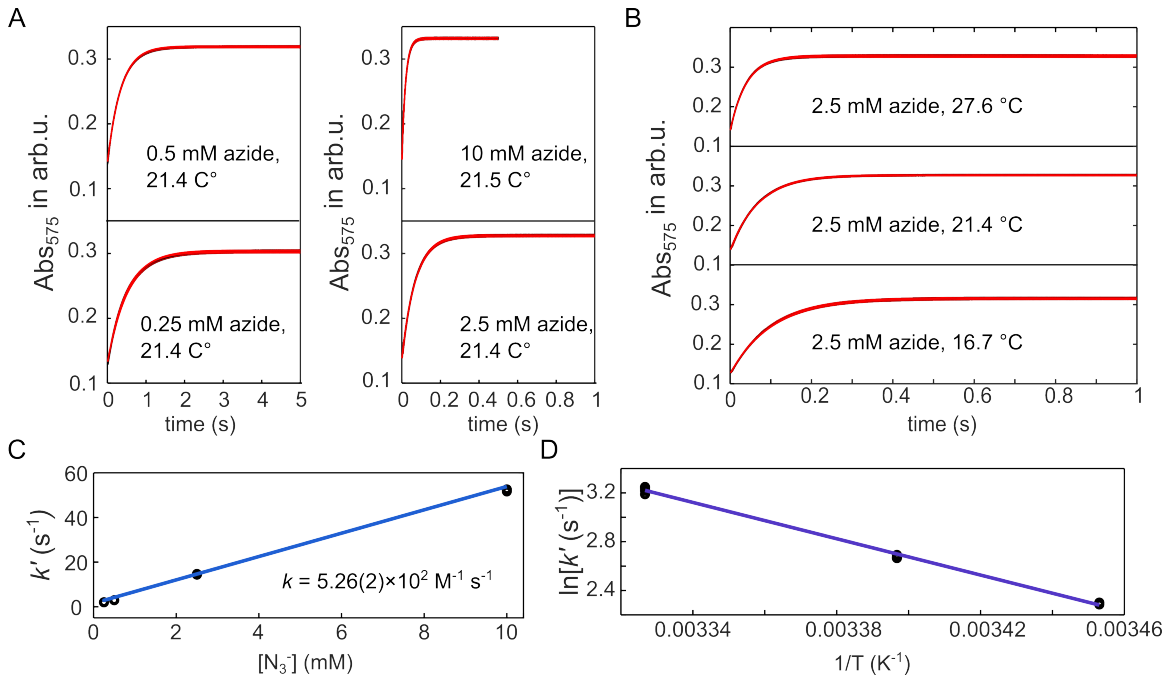

Figure 3.7: Stopped-flow absorption of myoglobin–azide monitored at 575 nM. A. The time traces using 50 μM myoglobin and 0.25 mM(×5), 0.5 mM (×10), 2.5 mM(×50) and 10 mM (×200) NaN_3 solutions prepared in 50 mM TRIS buffer (pH = 7.5). B. Temperature profile using 2.5 mM NaN_3. C. Linear fit of the rate constant k. D. Linear fit of the $\ln(k')$ and 1/T. The fitting model is adapted using Arrhenius equation: $\ln(k') = \frac{C_1}{R}(\frac{1}{T}) + C_2$, with $R = 8.3145$ J mol^{-1}K^{-1}, $C_1 = 159(2)$ J mol^{-1}, and $C_2 = 0.0722(9)$.

of excessive NaN_3, the kinetic of the myoglobin–azide binding interaction is treated as pseudo

first-order kinetics:

$$\mathrm{HS} + \mathrm{N_3^-} \rightarrow \mathrm{LS} \tag{3.2}$$

$$\frac{\mathrm{d[HS]}}{\mathrm{d}t} = -k' \times [\mathrm{HS}] \tag{3.3}$$

$$k' = k \times [\mathrm{N_3^-}], \tag{3.4}$$

and the integrated rate equation is

$$R_{\mathrm{HS}}(t) = \frac{[\mathrm{HS}]_t}{[\mathrm{HS}]_0} = \frac{[\mathrm{HS}]_t}{[\mathrm{HS}]_t + [\mathrm{LS}]_t} = \exp[-k't] \tag{3.5}$$

where R_{HS} is the fraction of HS, measurable via EPR, and t is the unknown reaction time. As described in Section 3.3, the reaction time is varied by changing the reaction distance (d) between mixer and the cryomedium. The conversion from $R_{\mathrm{HS}}(d)$ to $R_{\mathrm{HS}}(t)$ requires a known rate constant k, which is measured using stopped-flow absorption at 575 nm of the LS state.[100]

The stopped-flow absorption data was measured using 50 μM myoglobin and different concentrations of NaN_3 to extrapolate the rate constant k. All time traces are shown in Fig. 3.7A. The apparent rate constant k' increases with increasing concentration of azide as expected. The rate constant k is then obtained by fitting all k' using Eq. (3.4). This yielded $k = 5266(\pm 23)\ \mathrm{M^{-1}s^{-1}}$, which is slightly smaller than the reported value of $6504(\pm 49)\ \mathrm{M^{-1}s^{-1}}$.[100] The discrepancies are attributed to variations in chemicals, pipetting errors and temperature drifts. To assess the effect of temperature drifts, additional calibrations (Fig 3.7B) using 50 μM myogloblin and 2.5 mM NaN_3 were performed. The relation between temperature and the apparent kinetic rate k' is fitted (Fig. 3.7D) and can be used for correction if the device were to operate at different temperatures.

Having obtained a rate constant $k = 5266(\pm 23)\ \mathrm{M^{-1}s^{-1}}$, the time axis can be calculated using the change of fraction of HS over a range of reaction time. To prepare such EPR samples quenched at different times, solutions of 1mM myoglobin and 10 mM NaN_3 were prepared in 50 mM TRIS buffer (pH = 7.5) with 5%(v/v) glycerol. The addition of glycerol is a compromise

to suppress a background signal that is possibly caused by aggregation of protein during freezing (Fig. B.5). The addition of glycerol increases the viscosity of buffer solution and therefore alters the mixing efficiency. This effect is further demonstrated in Fig B.5 as well. In the future, stopped-flow absorption data should be collected using the appropriate amount of glycerol to account for its effect on rate constant. The sample solutions are prepared before injecting to the loading tubes that are maintained at 22(1) °C. The mixer chamber was regulated to maintain the same temperature range during sample deposition. To quench the reaction at different times, a total of 7 samples were collected using different mixer–cryomedium distances of 1, 4, 6, 8, and 11 cm. All frozen samples were collected and packed into 4 mm outer-diameter X-band EPR tubes before melting. The sample preparation and EPR experiments are described with more details in Appendix B.2.

Representative spectra of RFQ-prepared myoglobin–azide samples with different reaction times are plotted in Fig. 3.8A. The intensity of the HS spectrum does not decrease linearly as the reaction time increases. This is because the packing efficiency and therefore the spin concentration and signal intensity varies from tube to tube. Nevertheless, by visual inspection, the LS features emerge with increasing reaction time. Since the packing efficiency varies from sample to sample, the reaction progress is evaluated by the fraction of HS, as defined in Eq. (3.5). Conventionally, spin concentration is proportional to the double integral of the EPR spectrum; however, this quantification method is susceptible to baseline effect. Therefore, instead of using double integral, peak-to-peak intensity from the $g = 5.9$ feature of HS spectrum and from $g = 2.20$ of the LS spectrum are used for quantitative analysis. Figure 3.8B shows the fraction of HS calculateed from each spectrum as a function of reaction distance, which monotonously decreases as expected. The reaction time is calculated using equation

$$t = -\frac{\ln[R_{\mathrm{HS}}(d)]}{k[\mathrm{N}_3^-]} \tag{3.6}$$

where $k = 5266(\pm 23)\mathrm{M}^{-1}\mathrm{s}^{-}1$ is obtained from the stopped-flow data () and N_3^- is 10 mM. The calculated time values were plotted against reaction distance in Fig. 3.8C, and the data was

fitted using a linear model to convert any reaction distance to an estimated reaction time. The errors in R_{HS} are attributed to noise in spectra(< 0.2 %) and concentration. The time values are calculated using $\ln[R_{HS}]$ so that the errors are small and not included in Fig. 3.8B and C. The error propagated from k is less than 0.5%, and the ranges of calculated t are listed in Table B.1.

The experimentally determined operational range of the RFQ instrument has an instrumental dead time of 15.29 ms as a collective result of sample mixing time and freezing time. The operational range of the RFQ setup is 18.22 ms to 26.72 ms, covering 8.50 ms between 1 cm and 11 cm. The slope of the fit in Fig. 3.8C can be interpreted as the experimentally determined linear flow rate, which is equivalent to 17 ms^{-1}. Using a simple equation

$$\text{linear velocity} = \frac{\text{volumetric velocity}}{\text{cross section area}} \tag{3.7}$$

the linear flow rate of the system setup is 16.98 m s^{-1}, given 2 mL/min volumetric flow rate and 50 μM mixer nozzle O.D., which is in agreement with the experimentally determined flow rate. Using the current setup, the operational range of the RFQ is limited; however, the width of the reaction time window is reasonable.

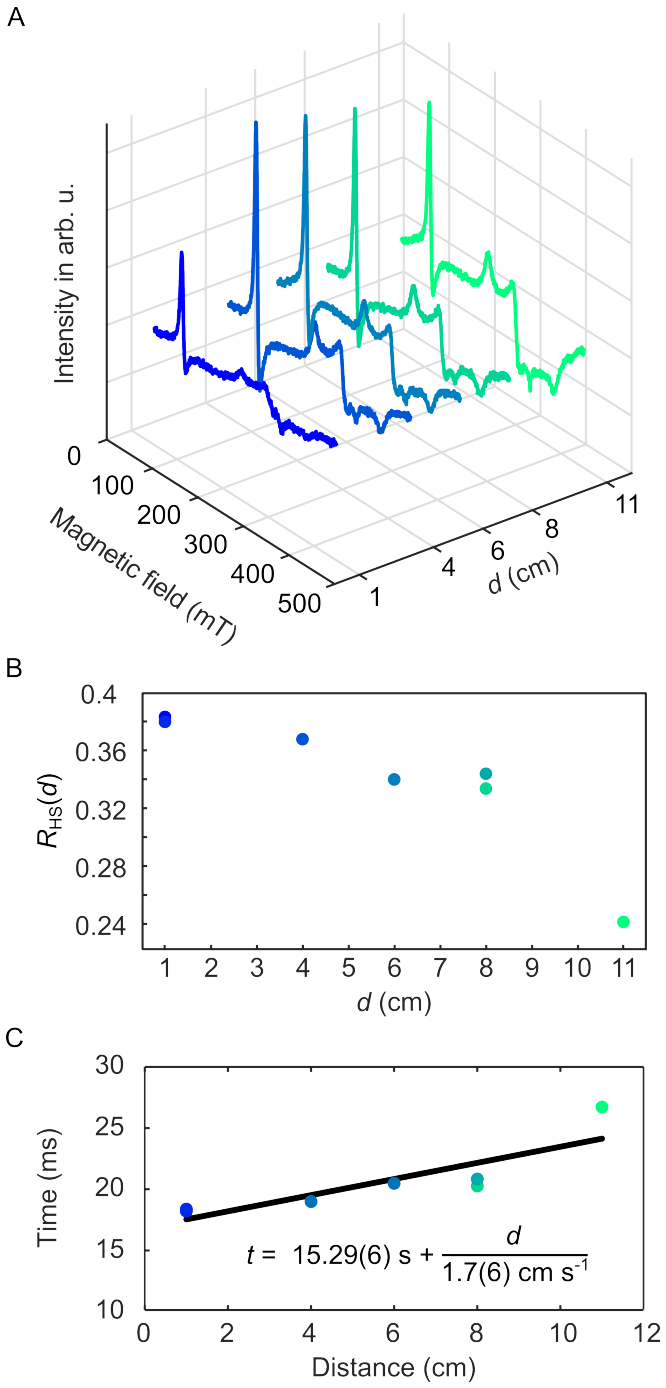

Figure 3.8: Determining the operational range of the home-built RFQ apparatus. A. Representative X-band EPR spectra of the myoglobin–azide binding interaction at 120 K. B. The fraction of the HS (R_{HS}) population in samples quenched at different reaction distances. C. The relation between reaction distance and reaction time calculated using R_{HS} and Eq. 3.6.

3.5 The dynamics of MBP open-to-close conversion

As discussed in Section 3.1, the advantage of RFQ is to preserve the state of a reaction for structural analysis. To validate the home-built RFQ apparatus, it was used for measuring the dynamics of conformational change of a model protein, maltose binding protein (MBP), upon ligand binding. MBP is a bacterial periplasmic binding protein involved in uptaking maltose sugars.[88,128] The conversion between the apo (PDBID: 1omp) and the holo (PDBID: 1anf) state is a well-studied hinge motion and can be characterized by monitoring the distance changes between two spin labels attached at two carefully chosen amino acid residues using DEER spectroscopy.[138]

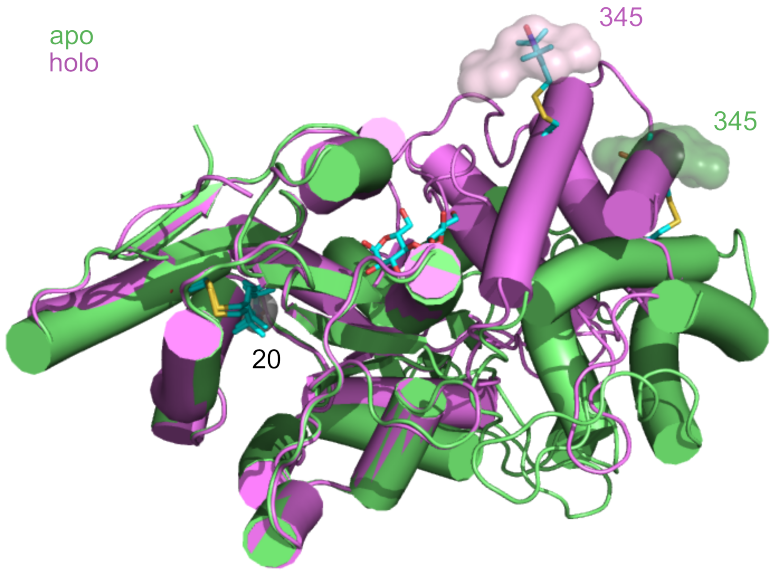

Figure 3.9: Crystal structure of MBP, with spin labels attached via in silico modeling. Residues L20/T345 are spin labeled with MTSSL. The spin label rotamer distributions are represented by the surface around the label. The spin labels and rotamers are attached to MBP *in silico* using chiLife.[139]

In spite of the well-characterized structural conversion of the MBP–maltose binding interaction, detailed information about the kinetics of this reaction is lacking. Miller et al.[88] reported stopped-flow measurements using cyclic maltoheptaose (β-dextrin), which suggests the

equal molar of MBP and ligand binding reaction reaches equilibrium around 25 ms. To reveal whether the MBP–maltose binding interaction is in a similar time range, the reaction should be quenched using the shortest time captured by the RFQ instrument, which is limited to 20.0 ms. Since the instrument is limited to capture reaction time between 20.0-27.6 ms, which is unlikely to cover the entire kinetic range of the MBP–maltose binding interaction, a time-fixed titration may reveal some kinetic information.

An MBP construct with R1 spin labels at sites L20 and T345 was chosen for two reasons: 1. a clear predicted distance shift upon binding to maltose, and 2. a relative short distance that compensates for the loss of spin concentration due to low packing efficiency.[138] The construct was purified by Maxx H. Tessmer from frozen cell culture.[138] All samples were prepared using 50 μM MBP, reacting with different concentrations of maltose at different reactions. The instrumental setup remained the same as calibration condition, and the reaction time distance was set to 1 cm, equivalent to 20 ms reaction time. To minimize the usage of MBP, the apo and holo states of were not prepared by RFQ and were instead slowly frozen in liquid nitrogen. More information regarding the sample preparation and DEER experiments are described in detail in Appendix B.2.

Figure 3.10A presents the DEER traces, and Fig. 3.10 B shows the associated distance distributions extracted from Tikhonov regularization and compactness regularization via an one-step implemented by DeerLab. The Tikhonov regularization parameter and the compactness regularization were selected based on Akaike information criterion (AIC) and informational complexity criterion (ICC), respectively. The apo and holo states have defined sharp distance peaks at 4.0 nm and 3.5 nm, respectively, which is in agreement with the data presented in the previous publication.[139] The RFQ sample using 5 mM maltose reaches equilibrium at 20 ms since the distance distribution only reveals a peak at the holo state distance of 3.5 nm. The RFQ sample using 50 μM shows that some population of the apo state with a shoulder peak at 4.0 nm. The differences in distance distribution between the two RFQ samples suggests a decreasing of reaction rate using less concentrated maltose as expected. The result shows the possibility of applying the current RFQ setup to reveal kinetic information from structural shift, measured by

DEER experiments.

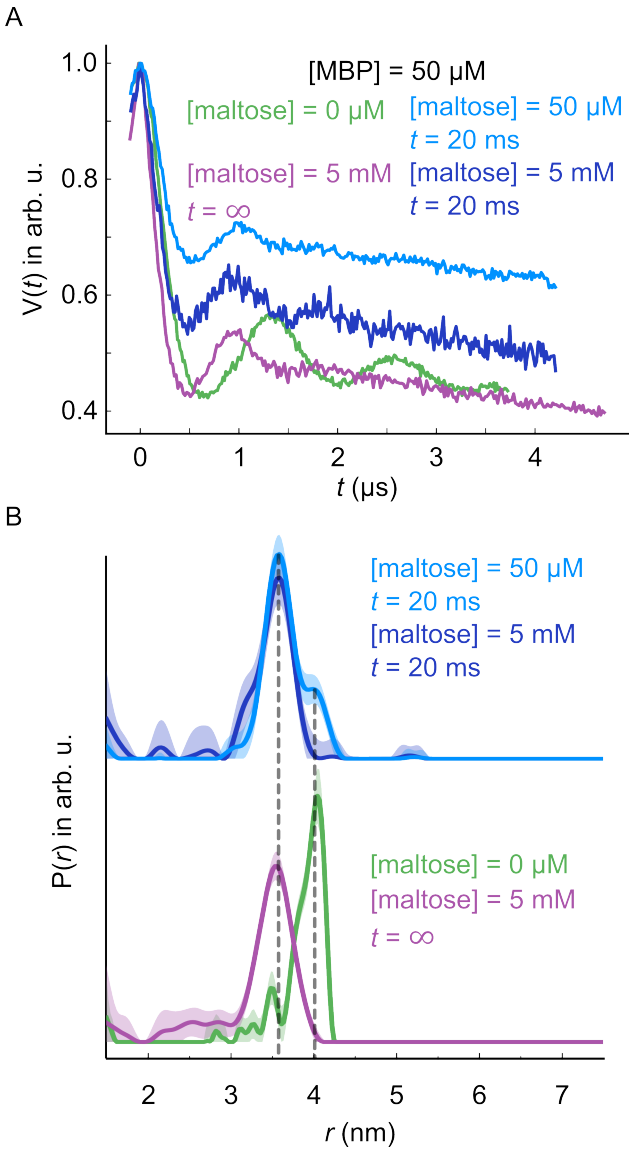

Figure 3.10: DEER data of MBP–maltose binding reaction. The concentration of MBP is 50 µM. A. Time-domain traces shifted to the same starting amplitude. B. Distance distributions generated using DeerLab.[44] Gray dotted line: center of the peaks at 4.0 nm and 3.5 nm. The shaded region on each $P(r)$ represents the 95% confidence interval.

3.6 Conclusion and future work

3.6.1 Conclusion

A home-built RFQ apparatus was designed and built. Using the myoglobin–azide reaction at X-band EPR spectroscopy, its dead time (15.29 ms) and operational range (18.22-26.72 ms) were determined. Using the calibrated setup, a fixed time point pseudo-titration of MBP–maltose binding interaction was assessed using equal molar and excessive maltose. The DEER results show that the current setup is capable of capturing the non-equilibrium state of the MBP–maltose binding interaction by adjusting the reaction rate via changing the ligand concentration.

3.6.2 Improving the performance of RFQ

The two main limitations of the current RFQ apparatus are the longer dead time and the small operational range. It is difficult to attribute the limitations to specific components. To improve the performance, the following strategies for alternative engineering and bench-marking experiments can be pursued:

1. Verify the mixing efficiency in the mixer by repeating the calibration with a range of NaN_3 concentrations. If the mixing efficiency is consistent, the calibrated time should remain the same regardless of the concentration of NaN_3 if analyzed using the method discussed in Section 3.4.

2. Repeat the stopped-flow measurements with buffer solution containing glycerol. The rate constant used in Section 3.4 was obtained by using aqueous buffer solution, whereas the RFQ samples were all prepared with glycerol.

3. Improve the sample deposition method on the cryomedium. In the current setup, the mixer sweeps through the round disc at a constant angular velocity, resulting in uneven distribution of depositing at different radii and possible elongated freezing rate.

4. Regulate the temperature within the nitrogen box. For longer reaction distance, the thin jet of mixed solution travels longer between the temperature regulated mixer manifold and the cryomedium. As it is exposed to the dry and cold air from liquid nitrogen boil-off, the probability of nonuniform reaction rate increases.

5. A new instrument implemented with a vacuum chamber is worth considering. The vacuum space minimize the air resistance and may increase the flow rate and therefore a shorter instrumental distance.

Appendix A

THEORY OF NV CENTER T_1 RELAXATION ENHANCEMENT

A.1 Definition of NV center T_1

This section discusses the theory for the dependence of the NV center T_1 on the nitroxide rotational correlation time.[140] In a weak external magnetic field, the $S = 1$ triplet ground state of the NV center splits into three energetically distinct states, $m_S = 0$, $m_S = -1$ and $m_S = +1$. The microscopic relaxation rates k_{01} across the two transitions $m_s = 0 \leftrightarrow -1$ and $0 \leftrightarrow +1$ are considered equal. The (effective) T_1 longitudinal relaxation time for the NV center is defined such that $1/T_1$ is the rate constant for the return of the $m_s = 0$ population to is thermal equilibrium population of $1/3$:

$$n_0(t) = \frac{1}{3} + \left(n_0(0) - \frac{1}{3}\right) e^{-t/T_1} \qquad 1/T_1 = 3k_{01} \tag{A.1}$$

Non-thermal populations are obtained by optical pumping using a laser pulse, which overpopulates the $m_s = 0$ state ($n_0(0) > 1/3$). After this polarization step, the recovery towards equilibrium is experimentally monitored via the spin-dependent photoluminescence intensity of the NV center, which is essentially proportional to n_0. The relaxation rate T_1 is obtained by fitting the decay of the photoluminescence intensity.

A.2 Effects from the spin label rotational motion

There are three contributions to T_1, as described by Eq. 2.1, and the contribution due to spin label rotational diffusion is indicated by T_1^{rot}. As in Eq. (A.1), this equals $1/T_1^{\text{rot}} = 3k_{01}^{\text{rot}}$, where k_{01}^{rot} is the microscopic rate constant for this process. It can be calculated using Fermi's golden

rule (,[9] Eqs. A5.12 and A5.14):

$$k_{01}^{\mathrm{rot}} = \left| -\frac{\mathrm{i}}{\hbar} \int_0^t \langle -1|\hat{H}(t)|0\rangle \exp\left(\mathrm{i}\omega_{\mathrm{NV}} t\right) dt \right|^2 . \tag{A.2}$$

where ω_{NV} is the (angular) transition frequency for $m_s = 0 \leftrightarrow -1$. The time dependence of the Hamiltonian comes from the rotational motion of the spin label and is a stochastic function $f(t)$. Factoring out the time dependence in the Hamiltonian as $H(t) = H \cdot f(t)$, we rewrite Eq. (A.2):

$$k_{01}^{\mathrm{rot}} = \frac{1}{\hbar^2} \left|\langle -1|\hat{H}|0\rangle\right|^2 \left| \int_0^t f(t) \exp\left(\mathrm{i}\omega_{\mathrm{NV}} t\right) dt \right|^2 \tag{A.3}$$

The integral in this expression is the spectral density $J(\omega)$, evaluated at $\omega = \omega_{\mathrm{NV}}$. In this specific model, the spectral density takes the form

$$J(\omega_{\mathrm{NV}}) = \frac{\tau_{\mathrm{c}}}{1 + \omega_{\mathrm{NV}}^2 \tau_{\mathrm{c}}^2}, \tag{A.4}$$

where τ_{c} is the rotational correlation time of the spin label.

Now we focus on the first term in Eq. (A.3) by writing out the elements in the time-independent Hamiltonian. The Hamiltonian takes the specific form

$$\hat{H} = g_{\mathrm{NV}} \mu_{\mathrm{B}} \boldsymbol{B}_{\mathrm{rot}} (\boldsymbol{u} \cdot \hat{\boldsymbol{S}}_{\mathrm{NV}}), \tag{A.5}$$

where $\boldsymbol{B}_{\mathrm{rot}}$ is the magnetic field at the NV center due to the spin label, $\hat{\boldsymbol{S}}_{\mathrm{NV}}$ is the spin vector operator of the NV center, and $\boldsymbol{u}$ is the unit vector $\boldsymbol{u} = \left[u_x, u_y, u_z\right] = \boldsymbol{r}/r^3$. Alternatively, these elements can be written as $\left[\sin\theta\cos\phi, \sin\theta\sin\phi, \cos\theta\right]$ in spherical coordinates. The dot product of the unit vector $\boldsymbol{u}$ and $\hat{\boldsymbol{S}}_{\mathrm{NV}}$ project the spin operator to the NV–spin label distance vector $\boldsymbol{r}$. Substituting the Hamiltonian back the first term of Eq. A.3, we obtain

$$\begin{aligned} \frac{1}{\hbar^2} \left|\langle -1|\hat{H}|0\rangle\right|^2 &= \frac{g_{\mathrm{NV}}^2 \mu_{\mathrm{B}}^2}{\hbar^2} \left|\langle -1|\boldsymbol{B}_{\mathrm{rot}} (\boldsymbol{u} \cdot \hat{\boldsymbol{S}}_{\mathrm{NV}})|0\rangle\right|^2 \\ &= \gamma_{\mathrm{NV}}^2 \left|\langle -1|\boldsymbol{B}_{\mathrm{rot}} (\boldsymbol{u} \cdot \hat{\boldsymbol{S}}_{\mathrm{NV}})|0\rangle\right|^2 , \end{aligned} \tag{A.6}$$

where γ_{NV} is the gyromagnetic ratio of the NV center spins.

Although $\boldsymbol{B}_{\mathrm{rot}}$ originates from a quantum system, the field is treated as a constant irradiation with variance caused by rotational motion. Since only the field perpendicular to the quantized magnetic field of the NV center spins will induce transition, only the averaged $B_{\perp,\mathrm{rot}}$ is needed for modeling purposes, and it can be calculated by averaging the x- and y-components of $\boldsymbol{B}_{\mathrm{rot}}$. As a result, we obtain

$$\begin{aligned}
&\gamma_{\mathrm{NV}}^2 \left|\langle -1|\boldsymbol{B}_{\mathrm{rot}}(\boldsymbol{u}\cdot\hat{\boldsymbol{S}}_{\mathrm{NV}})|0\rangle\right|^2 \\
=&\gamma_{\mathrm{NV}}^2 B_{\perp,\mathrm{rot}}^2 \left|\langle -1|\boldsymbol{u}\cdot\hat{\boldsymbol{S}}_{\mathrm{NV}}|0\rangle\right| \\
=&\gamma_{\mathrm{NV}}^2 \langle B_x^2 + B_y^2\rangle \left|\langle -1|\boldsymbol{u}\cdot\hat{\boldsymbol{S}}_{\mathrm{NV}}|0\rangle\right|^2 \\
=&\gamma_{\mathrm{NV}}^2 \mathrm{Tr}\{\hat{\rho}(B_x^2 + B_y^2)\} \left|\langle -1|\boldsymbol{u}\cdot\hat{\boldsymbol{S}}_{\mathrm{NV}}|0\rangle\right|^2,
\end{aligned} \tag{A.7}$$

where $\hat{\rho}$ is the density operator at thermal equilibrium, i.e. at room temperature approximately a 2-by-2 identity matrix with a prefactor $\frac{1}{2}$. The exact elements of $\boldsymbol{B}_{\mathrm{rot}}$ are obtained from

$$\boldsymbol{B}_{\mathrm{rot}} = \frac{\mu_0}{4\pi r^3}\hbar\gamma_{\mathrm{SL}}\left(\hat{\boldsymbol{S}}_{\mathrm{SL}} - 3(\hat{\boldsymbol{S}}_{\mathrm{SL}}\cdot\boldsymbol{u})\boldsymbol{u}\right), \tag{A.8}$$

where r is the scalar distance between the NV center and spin label, γ_{SL} is the gyromagnetic ratio of the spin label, and $\hat{\boldsymbol{S}}_{\mathrm{SL}}$ is the spin vector operator for the spin label. Equation A.8 can be written in the expanded form as

$$\begin{pmatrix} B_{x,\mathrm{rot}} \\ B_{y,\mathrm{rot}} \\ B_{z,\mathrm{rot}} \end{pmatrix} = c \begin{pmatrix} \hat{S}_{x,\mathrm{SL}}(1-3{u_x}^2) + \hat{S}_{y,\mathrm{SL}}(-3u_x u_y) + \hat{S}_{z,\mathrm{SL}}(-3u_x u_z) \\ \hat{S}_{x,\mathrm{SL}}(-3u_x u_y) + \hat{S}_{y,\mathrm{SL}}(1-3{u_y}^2) + \hat{S}_{z,\mathrm{SL}}(-3u_y u_z) \\ \hat{S}_{x,\mathrm{SL}}(-3u_x u_z) + \hat{S}_{y,\mathrm{SL}}(-3u_y u_z) + \hat{S}_{z,\mathrm{SL}}(1-3{u_z}^2) \end{pmatrix}, \tag{A.9}$$

where $c = (\mu_0/4\pi)\hbar\gamma_{\mathrm{SL}}/r^3$. Now we choose the coordinate system such that $\boldsymbol{r}$ lies in the xz plane, so that $u_y = 0$. Summing all the non-zero terms in B_x^2 and B_y^2, we obtain

$$B_{\perp,\mathrm{rot}}^2 = c^2\left[\left\langle\hat{S}_x^2\right\rangle(1-3{u_x}^2)^2 + \left\langle\hat{S}_x\hat{S}_z + \hat{S}_z\hat{S}_x\right\rangle(1-3u_x^2)(-3u_x u_z) + \left\langle\hat{S}_z^2\right\rangle(-3u_x u_z)^2 + \left\langle\hat{S}_y^2\right\rangle\right]. \tag{A.10}$$

The term $\langle \hat{S}_x \hat{S}_z + \hat{S}_z S_x \rangle$ vanishes, since the operators have only off-diagonal elements. The other expectation values are $\langle \hat{S}_x^2 \rangle = \langle \hat{S}_y^2 \rangle = \langle \hat{S}_z^2 \rangle = 1/4$. This gives

$$\begin{aligned} B_{\perp,\,\mathrm{rot}}^2 &= \frac{c^2}{4}\left[(1-3u_x^2)^2 + (-3u_x u_z)^2 + 1\right] \\ &= \frac{c^2}{4}\left[1 - 6u_x^2 + 9u_x^4 + 9u_x^2 u_z^2 + 1\right] \\ &= \frac{c^2}{4}\left[2 - 6u_x^2 + 9u_x^2(u_x^2 + u_z^2)\right] \\ &= \frac{c^2}{4}\left[2 + 3u_x^2\right] \end{aligned} \tag{A.11}$$

With $\boldsymbol{u} = [\sin\theta,\, 0,\, \cos\theta]$, this gives the result

$$B_{\perp,\mathrm{rot}}^2 = \frac{1}{4}\left(\frac{\mu_0}{4\pi}\gamma_{\mathrm{SL}}\hbar\right)^2 \frac{2 + 3\sin^2\theta}{r^6} \tag{A.12}$$

Finally, we obtain the exact elements in $|\langle -1|\boldsymbol{u}\cdot\boldsymbol{S}_{\mathrm{NV}}|0\rangle|^2$ by expanding the expression:

$$\begin{aligned} &|\langle -1|\boldsymbol{u}\cdot\boldsymbol{S}_{\mathrm{NV}}|0\rangle|^2 \\ &= \left| \left\langle -1 \right| \begin{bmatrix} \sin\theta & 0 & \cos\theta \end{bmatrix} \cdot \begin{bmatrix} \hat{S}_{x,\mathrm{NV}} \\ \hat{S}_{y,\mathrm{NV}} \\ \hat{S}_{z,\mathrm{NV}} \end{bmatrix} \left| 0 \right\rangle \right|^2 \\ &= \begin{pmatrix} |\langle -1|\sin\theta\hat{S}_{x,\mathrm{NV}}|0\rangle|^2 & 0 & |\langle -1|\cos\theta\hat{S}_{x,\mathrm{NV}}|0\rangle|^2 \\ |\langle -1|\sin\theta\hat{S}_{y,\mathrm{NV}}|0\rangle|^2 & 0 & |\langle -1|\cos\theta\hat{S}_{y,\mathrm{NV}}|0\rangle|^2 \\ |\langle -1|\sin\theta\hat{S}_{z,\mathrm{NV}}|0\rangle|^2 & 0 & |\langle -1|\cos\theta\hat{S}_{z,\mathrm{NV}}|0\rangle|^2 \end{pmatrix}. \end{aligned} \tag{A.13}$$

Then we utilize the relations

$$\begin{aligned} \langle m'|\hat{S}_x|m\rangle &= (\delta_{m',m+1} + \delta_{m'+1,m})\frac{1}{2}\sqrt{S(S+1) - m'm}, \\ \langle m'|\hat{S}_y|m\rangle &= (\delta_{m',m+1} - \delta_{m'+1,m})\frac{1}{2\mathrm{i}}\sqrt{S(S+1) - m'm}, \\ \langle m'|\hat{S}_z|m\rangle &= (\delta_{m',m})m, \end{aligned} \tag{A.14}$$

where $m' = -1$, $m = 1$ and $S = 1$. After eliminating the zero terms, we obtain

$$\left|\langle -1|\boldsymbol{u}\cdot\hat{\boldsymbol{S}}_{\mathrm{NV}}|0\rangle\right|^2 = 2(\sin^2\theta+\cos^2\theta)(\frac{1}{2}) = 1 \tag{A.15}$$

Now we collect all the elements from above equations and obtain the final expression

$$\frac{1}{T_1^{\mathrm{rot}}} = 3k_{01}^{\mathrm{rot}} = 3\left[\frac{1}{4}\gamma_{\mathrm{NV}}^2\left(\frac{\mu_0}{4\pi}\gamma_{\mathrm{SL}}\hbar\right)^2\left(\frac{2+3\sin^2\theta}{r^6}\right)\left(\frac{\tau_{\mathrm{c}}}{1+\omega_{\mathrm{NV}}^2\tau_{\mathrm{c}}^2}\right)\right] \tag{A.16}$$

A.3 Effects due to magnetic relaxation dynamics spin label

This section contains evaluation of the term $1/T_1^{\mathrm{rlx}}$ in Eq. 2.1. As discussed in Chapter 2, this term accounts for the magnetic relaxation dynamics of the spin label, which affects the NV center through dipolar interaction. Here we used a range of T_2 values for nitroxide spin labels based on a reference[34,117] to determine whether the contribution from this term is comparable to the effects from other two terms. The T_1 and T_2 ranges of the nitroxide spin labels are chosen to be 0.3 to 3 μs and 0.1 to 1 μs, respectively. A specific NV center–spin label geometry with a spin–spin distance of 4.5 nm and an angle of 45° away from $\boldsymbol{B}_{0,z}$ is used for evaluation. Using Eq. (4) through (7) from the main text, the range of $1/T_{\mathrm{rlx}}$ falls between 0.0566 s^{-1} 0.0057 s^{-1}, whereas the intrinsic $1/T_1^0$ is 285.7 s^{-1}. We therefore consider the effect of the spin label magnetic relaxation dynamics to be inconsequential in the discussion.

A.4 Addtional spectra and fitting results

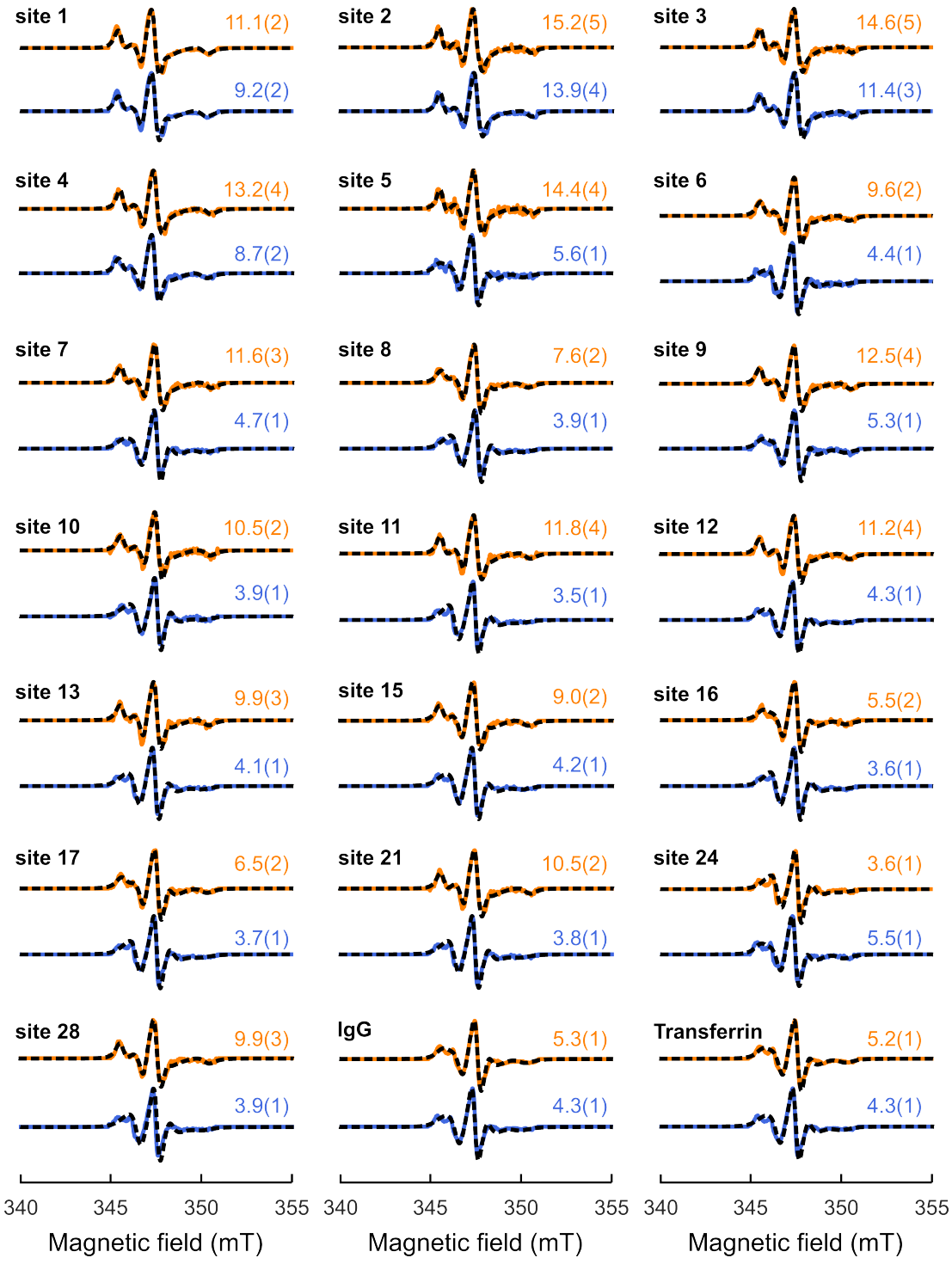

Figure A.1: All EPR spectra of spin-labeled SL5 and simulations in derivative lineshape.

Table A.1: The anisotropic g-tensors from simulations with fitting errors. All values are about 0.002-0.0025 units too high due to the lack of field calibration.

Site	$g_{x,\text{ apo}}$	$g_{y,\text{ apo}}$	$g_{z,\text{ apo}}$	$g_{x,\text{ holo}}$	$g_{y,\text{ holo}}$	$g_{z,\text{ holo}}$
1	2.0114(1)	2.0100(2)	2.0053(1)	2.0115(1)	2.0103(1)	2.0051(0)
2	2.0099(2)	2.0092(2)	2.0038(1)	2.0001(2)	2.0097(2)	2.0039(0)
3	2.0100(2)	2.0089(2)	2.0039(1)	2.0101(2)	2.0095(2)	2.0040(1)
4	2.0106(5)	2.0110(5)	2.0051(1)	2.0099(3)	2.0102(3)	2.0040(1)
5	2.0100(7)	2.0108(7)	2.0058(1)	2.0094(3)	2.0100(3)	2.0038(0)
6	2.0107(7)	2.0099(7)	2.0061(1)	2.0094(5)	2.0093(6)	2.0041(1)
7	2.0094(1)	2.0093(1)	2.0050(1)	2.0096(4)	2.0091(4)	2.0038(1)
8	2.0093(7)	2.0088(7)	2.0047(1)	2.0094(6)	2.0096(6)	2.0044(1)
9	2.0094(8)	2.0089(8)	2.0048(1)	2.0097(5)	2.0095(5)	2.0041(1)
10	2.0096(1)	2.0086(1)	2.0050(1)	2.0098(4)	2.0088(5)	2.0040(1)
11	2.0103(1)	2.0099(1)	2.0057(2)	2.0097(6)	2.0099(6)	2.0040(1)
12	2.0103(1)	2.0099(1)	2.0060(1)	2.0097(6)	2.0096(7)	2.0043(1)
13	2.0103(1)	2.0102(1)	2.0058(1)	2.0096(6)	2.0100(6)	2.0043(1)
15	2.0102(8)	2.0103(8)	2.0059(1)	2.0096(6)	2.0103(6)	2.0043(1)
16	2.0098(9)	2.0091(9)	2.0053(1)	2.0093(1)	2.0092(1)	2.0046(1)
17	2.0098(9)	2.0094(9)	2.0055(1)	2.0092(7)	2.0095(8)	2.0045(1)
21	2.0104(1)	2.0101(1)	2.0060(1)	2.0093(5)	2.0095(5)	2.0039(1)
24	2.0105(5)	2.0102(5)	2.0056(1)	2.0094(2)	2.0089(2)	2.0050(2)
28	2.0102(1)	2.0100(1)	2.0059(1)	2.0096(5)	2.0098(5)	2.0042(1)
12 + IgG	2.0103(1)	2.0099(1)	2.0060(1)	2.0105(1)	2.0073(1)	2.0047(1)
12 +trans-ferrin	2.0103(1)	2.0099(1)	2.0060(1)	2.0098(1)	2.0087(1)	2.0046(1)

Table A.2: Fitted τ_c and T_1 values using $T_{1,0} = 3.5$ ms, $r = 6$ nm, and $\theta = 45°$ (the same geometry and $T_{1,0}$ used for Fig. 2.10). The errors in T_1 are propagated from fitting errors of τ_c.

Site	$\tau_{c,\text{apo}}$ (ns)	$\tau_{c,\text{holo}}$ (ns)	$T_{1,\text{apo}}$ (ms)	$T_{1,\text{holo}}$ (ms)
1	9.2(2)	11.1(2)	3.476(1)	3.480(0)
2	13.9(4)	15.2(5)	3.484(0)	3.485(0)
3	11.4(3)	14.6(5)	3.480(1)	3.485(1)
4	8.7(2)	13.2(4)	3.474(1)	3.483(0)
5	5.6(1)	14.4(4)	3.460(1)	3.484(0)
6	4.4(1)	9.7(2)	3.450(1)	3.477(1)
7	4.7(1)	11.6(3)	3.452(1)	3.481(1)
8	3.9(0)	7.6(2)	3.442(1)	3.470(1)
9	5.3(1)	12.5(4)	3.458(1)	3.482(1)
10	3.9(1)	10.5(2)	3.443(1)	3.479(0)
11	3.5(1)	11.8(4)	3.437(2)	3.481(1)
12	4.3(1)	11.1(4)	3.448(1)	3.480(1)
13	4.1(1)	9.9(3)	3.445(1)	3.477(1)
15	4.2(1)	9.0(2)	3.447(1)	3.475(1)
16	3.6(1)	5.5(2)	3.437(1)	3.459(1)
17	3.7(1)	6.5(2)	3.439(1)	3.466(1)
21	3.8(1)	10.5(2)	3.441(1)	3.478(0)
24	5.5(1)	3.6(1)	3.459(1)	3.439(2)
28	3.9(1)	9.9(3)	3.443(1)	3.477(1)
12 + IgG	4.3(1)	5.3(1)	3.448(1)	3.457(1)
12+ transferrin	4.3(1)	5.2(1)	3.448(0)	3.458(1)

Appendix B

DETAILS OF RFQ DESIGN AND EPR EXPERIMENTS

B.1 Figures of miscellaneous RFQ components

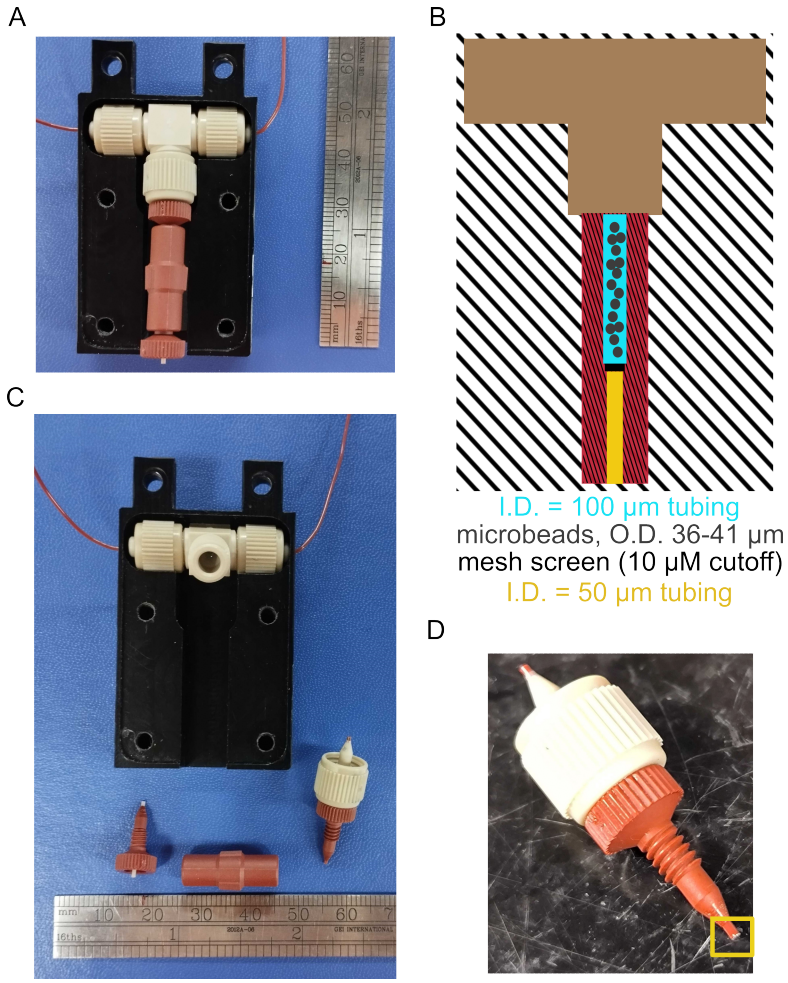

Figure B.1: The mixer and mixer manifold. A. Placement of the T-shaped mixer and the union in a customized manifold. B. An abstract diagram of the packed beads inside the 100 μm tubing. C. The same setup with disassembled fittings. D. A close-up photo of the mesh screen placed at the end of the tubing.

A

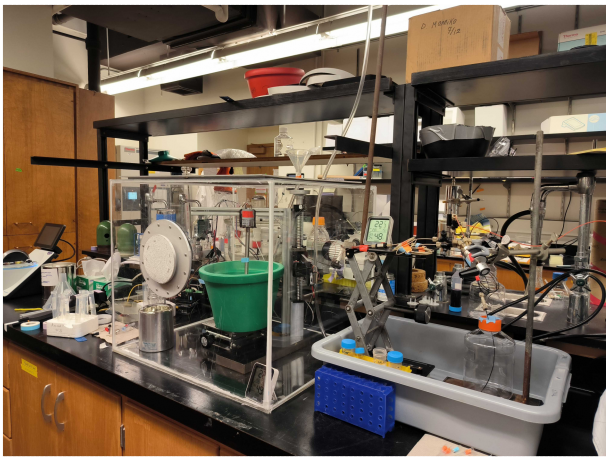

Figure B.2: Photos of the home-built RFQ instrument.
A. The RFQ setup on lab bench.

B

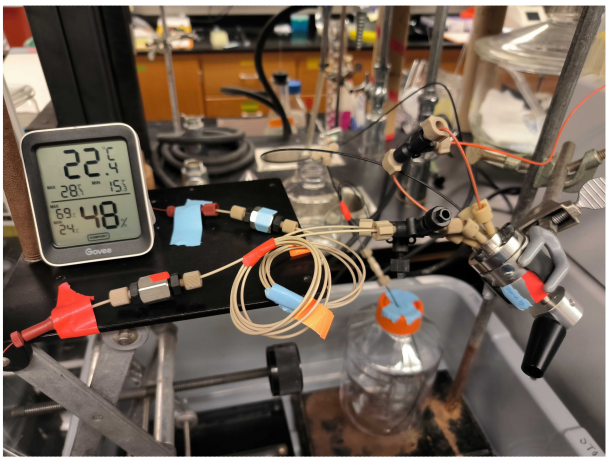

B. The tubing connections. From right to left: injector (Rheodyne 7725) to sample loading loops (Rheodyne 9725i, 200µL) to inline filters (IDEX A-431) to unions (IDEX P-881).

C

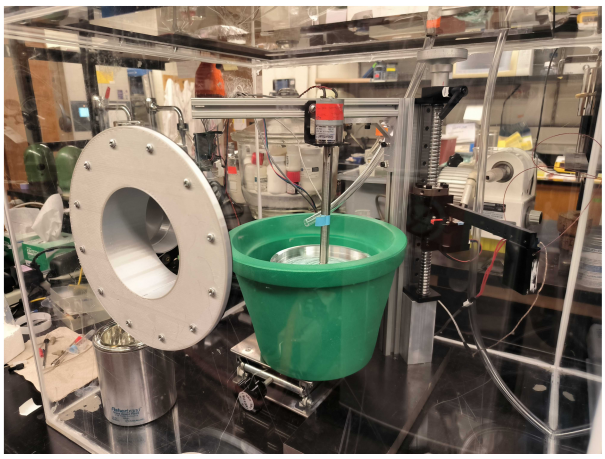

C. The sample collection setup inside the nitrogen box. The cryomedium will be submerged into the green ice bucket for cooling and will be spinning as the sample deposits.

Figure B.3: Packing myoglobin–azide sample.

B.2 Extended information of EPR experiments

For all of the RFQ-prepared samples, the volume of solution doubles as the protein and ligand mix; therefore, the initial concentrations are **twice** as the resulting concentration. This section only reports the **initial concentration**.

B.2.1 Stopped-flow experiments for determining the rate constant of Myoglobin–azide reaction

The stopped-flow absorption data set was measured using Applied Photophysics SX 18 MV. Myoglobin (MilliporeSigma M0630) and sodium azide (MilliporeSigma 1066880100) were prepared in 100 mM TRIS buffer (pH = 7.5). The concentrations of NaN_3 solution are 0.5 mM, 1 mM, 5 mM and 20 mM, resulting a ratio 5, 10, 50, and 200 folds excess. All time traces were analyzed under the pseudo 1^{st}-order assumption and were fitted using equation

$$A(t) = C \times \exp(-k' \times t) \tag{B.1}$$

The temperature series was performed using 2.5 mM NaN_3 at 16.7 C°, 21.4 C°, and 27.6 C°. An equation based off the Arrhenius equation was used for fitting:

$$\ln(k') = \frac{C_1}{R}(\frac{1}{T}) + C_2 \tag{B.2}$$

The physical interpretation of the C_1 and C_2 is neglected since the purpose of this data set will only be used for correcting the effect from drifting room temperature.

B.2.2 Myoglobin–azide calibration reaction and X-band EPR experiments

Stock solutions of 2 mM myoglobin and 20 mM NaN_3 were prepared in 50 mM TRIS buffer (pH = 7.5) with 5% glycerol(v/v). A total of 200 μL of each solution is loaded to the sample loops using a Hamilton gas-tight syringe for each sample. The flow rate of the HPLC was set to 2 mL/min.

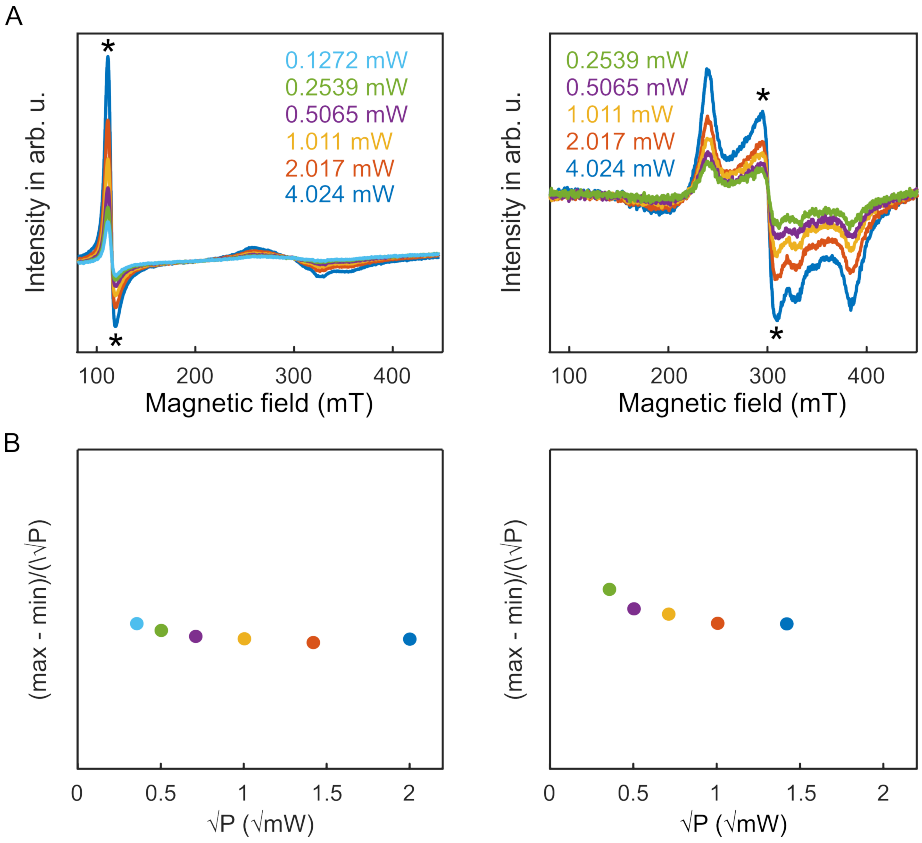

Figure B.4: Microwave power saturation behavior of the HS ($S = 5/2$) and LS ($S = 1/2$) state of myoglobin. A. Spectra of HS (500 μM) and LS (500 μM) myglobin collected at different microwave power. Right: HS. Left: LS. B. Difference between the max-to-min intensity of each spectrum normalized to square-root of the corresponding microwave power ($\sqrt{P}$). Right: HS. Left: LS.

All spectra in Fig. 3.8 were measured using Bruker EMX and SHQE resonator with a resonator frequency of 9.30(1) GHz. The cavity temperature ranges from 120-125 K. All spectra were obtained with a peak-to-peak modulation amplitude of 1 mT and a sweep rate of 4 mT/s and were collected at 0.5(0) mW. The HS and LS signals are slightly saturated as shown in Fig. B.4. This is addressed by using a normalizing factor R_0, which is described in details in Appendix B.3 in quantitative analysis of spin population.

Figure B.5 shows the differences in data quality of representative spectra, using samples prepared with different glycerol content. The data shown in this figure are not baseline corrected.

All samples were prepared using 1mM myoglobin and 5 mM NaN_3. Aqueous buffer has the worst baseline problem overall. Using 20% glycerol mitigates the issue but also affect the mixing efficiency by visual inspection. The artifact baseline shape obscures the certainty of quantitative analysis, and to make a compromise, 5% of glycerol was used in the dataset used for quantitative analysis in Section 3.4. Noticeably, the spectra collected from long reaction/longer distance tend to have worse baseline problem. The physical reason is unclear.

B.2.3 MBP–maltose DEER measurements

All samples were prepared in deuterated MBP binding buffer (20 mM TRIS, 20 mM imidazole, 150 mM NaCl, pH 7.5). The non-RFQ samples were made prepared in buffer with 20% glycerol and transferred to 1.5 mm O.D., 1.1 mm I.D. quartz capillaries (Sutter Instrument) and then flash frozen in liquid nitrogen. The non-RFQ samples were measured using a Bruker MD2 dielectric resonator. The RFQ samples were prepared using buffer with 5% glycerol to match with the RFQ calibration conditions. The frozen solution was packed from the cryomedium to a 3 mm O.D. quartz tube (Wilmad-Labglass, 705-SQ-250). The RFQ samples were measured using a Bruker QT2 cavity resonator.

All DEER experiments were performed using Bruker EleXsys E580 EPR spectrometer equipped with SpinJet AWG and a 390 W TWT amplifier (Applied Systems Engineering) at Q-band frequencies. The experiment pulse sequence is the standard four-pulse DEER sequence $(\pi/2)_{\text{probe}} - \tau_1 - (\pi)_{\text{probe}} - (\tau_1 + t) - (\pi)_{\text{pump}} - (\tau_2 - t) - (\pi)_{\text{probe}} - \tau_2 -$ echo. All probe pulses were 60 ns Gaussian pulses centered at the maximum of the nitroxide spectrum with corresponding flip angles. All pump pulses were 150 ns sech/tahn ($\beta = 10$) pulses 40-120 MHz above the probe frequency. The resonator temperature was set to 50 K. All time-domain traces were analyzed with DeerLab.[44] The time domain data was transformed to distance distribution with a modal constructed using non-parametric distribution and a homogeneous background. .

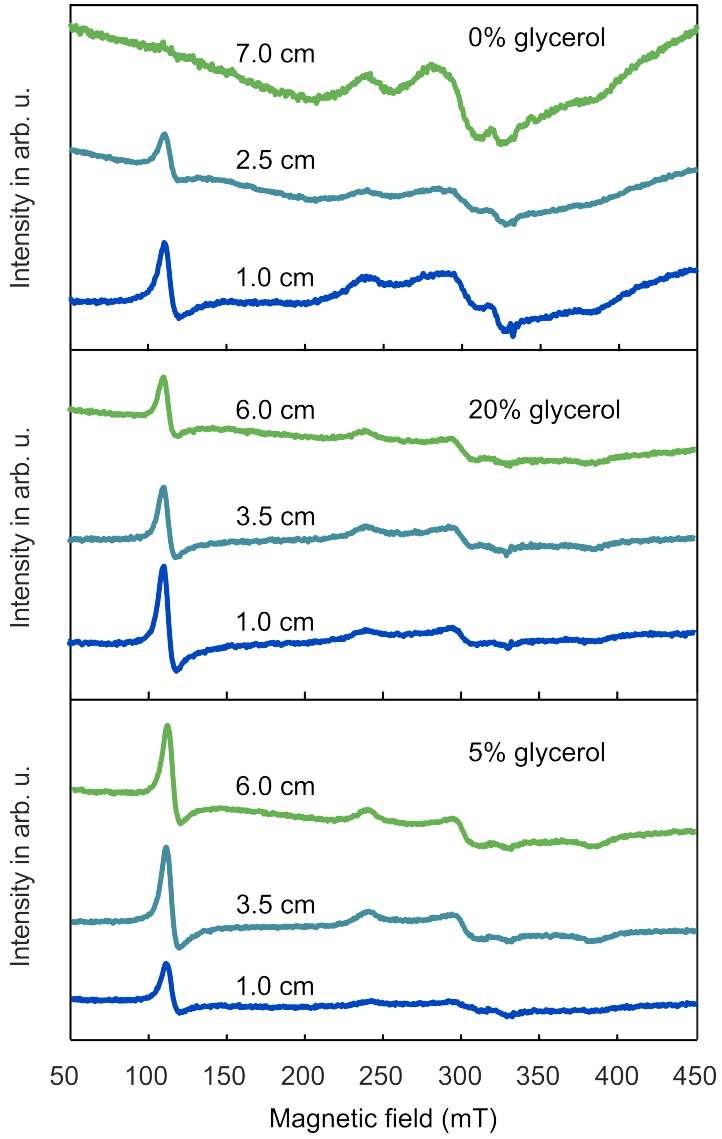

Figure B.5: Representative spectra collected using 0%(top), 20%(middle) and 5%(bottom) glycerol in buffer solution. The reaction time is indicated by reaction distance.

B.3 Derivation of $R_{HS}(t)$ for time axis calibration

This section is focused on the derivation of $R_{HS}(t)$. The mathematical treatment is based on the derivation in Pievo et al.[100] and Hett et al.[57] with several modifications.

As stated in Eq. 3.5, $R_{HS}(t)$ is defined as the ratio of the concentration at HS a given reac-

tion time t to the initial concentration of HS-state myoglobin. At 120 K and under dilute spin concentration (< 2mM), it is assumed that the peak-to-peak intensity of each spectrum is proportional to spin concentration, and this relation is described as

$$I_{\mathrm{HS}} = c_{\mathrm{HS}}[\mathrm{HS}] \tag{B.3}$$

$$I_{\mathrm{LS}} = c_{\mathrm{LS}}[\mathrm{LS}] \tag{B.4}$$

where I is defined as the peak-to-peak intensity. Equation 3.5 can therefore be restated as

$$R_{\mathrm{HS}}(t) = \frac{(I_{\mathrm{HS}})_t}{(I_{\mathrm{HS}})_0} = C \times \exp[-\mathrm{k't}] \tag{B.5}$$

where C is a scaling factor. As mentioned in Section 3.4, the signal intensity varies from sample to sample due to inconsistency in packing efficiency (Fig. 3.8A). Therefore, a simple division between the $(I_{\mathrm{HS}})_t$ and $I_{\mathrm{HS}})_0$ (not prepared by RFQ) is incorrect. To bypass this problem, assuming the total myoglobin population is the combined HS and LS population, Eq. 3.5 is rewritten as

$$R_{\mathrm{HS}}(t) = \frac{[\mathrm{HS}]_t}{[\mathrm{HS}]_t + [\mathrm{LS}]_t} = C \times \exp[-\mathrm{k't}] \tag{B.6}$$

$$[\mathrm{HS}]_t + [\mathrm{LS}]_t = [\mathrm{HS}]_0 = [\mathrm{LS}]_\infty \tag{B.7}$$

Using the relation in Eq. B.4,

$$R_{\mathrm{HS}}(t) = \frac{(I_{\mathrm{HS}})_t}{(I_{\mathrm{HS}})_t + R_0(I_{\mathrm{LS}})_t} = C \times \exp[-\mathrm{k't}] \tag{B.8}$$

$$R_0 = \frac{c_{\mathrm{HS}}}{c_{\mathrm{LS}}} \tag{B.9}$$

Having obtained R_{HS}, the time points associated with reaction distances can be solved using Eq. 3.6. The errors from k are propagated to the calculated t values and are listed in Table B.1.

Table B.1: The ranges of calculated t.

distance (cm)	t_{min} (ms)	t_{mean} (ms)	t_{max} (ms)
1	18.14	18.22	18.30
1	18.30	18.38	18.46
4	18.91	19.00	19.08
6	20.40	20.49	20.58
8	20.18	20.26	20.36
8	20.76	20.85	20.94
11	26.61	26.72	26.84

BIBLIOGRAPHY

[1] N. J. Agard, J. A. Prescher, and C. R. Bertozzi. A strain-promoted [3 + 2] azide-alkyne cycloaddition for covalent modification of biomolecules in living systems. *J. Am. Chem. Soc.*, 126(46):15046–15047, 2004.

[2] N. J. Agard, J. A. Prescher, and C. R. Bertozzi. A strain-promoted [3 + 2] azide-alkyne cycloaddition for covalent modification of biomolecules in living systems. *J. Am. Chem. Soc.*, 126(46):15046–15047, 2004.

[3] R. D. Akiel, X. Zhang, C. Abeywardana, V. Stepanov, P. Z. Qin, and S. Takahashi. Investigating functional DNA grafted on nanodiamond surface using site-directed spin labeling and electron paramagnetic resonance spectroscopy. *J. Phys. Chem. B*, 120(17):4003–4008, 2016.

[4] F. Alghannam and P. Hemmer. Engineering of Shallow Layers of Nitrogen Vacancy Colour Centres in Diamond Using Plasma Immersion Ion Implantation. *Sci. Rep.*, 9(1):5870, 2019.

[5] M. M. Aljohani, D. Cialla-May, J. Popp, R. Chinnappan, K. Al-Kattan, and M. Zourob. Aptamers: Potential Diagnostic and Therapeutic Agents for Blood Diseases. *Molecules*, 27(2):383, 2022.

[6] R. D. Allert, K. D. Briegel, and D. B. Bucher. Advances in nano- and microscale NMR spectroscopy using diamond quantum sensors. *Chem. Commun.*, 58:8165–8181, 2022.

[7] N. L. Anderson and N. G. Anderson. The Human Plasma Proteome: History, Character, and Diagnostic Prospects. *Mol. Cell Proteomics*, 1(11):845–867, 2002.

[8] A. Ariyaratne, D. Bluvstein, B. A. Myers, and A. C. B. Jayich. Nanoscale electrical conductivity imaging using a nitrogen-vacancy center in diamond. *Nat. Commun.*, 9(1):1–7, 2018.

[9] N. M. Atherton. *Principles of Electron Spin Resonance*. Ellis Horwood PTR Prenticie Hall, 1993.

[10] G. Balasubramanian, P. Neumann, D. Twitchen, M. Markham, R. Kolesov, N. Mizuochi, J. Isoya, J. Achard, J. Beck, J. Tissler, V. Jacques, P. R. Hemmer, F. Jelezko, and J. Wrachtrup. Ultralong spin coherence time in isotopically engineered diamond. *Nat. Mater.*, 8(5):383–387, 2009.

[11] D. P. Ballou. [7] Freeze-quench and chemical-quench techniques. In *Methods in Enzymology*, volume 54, pages 85–93. Elsevier, 1978.

[12] D. P. Ballou and G. A. Palmer. Practical Rapid Quenching Instrument for the Study of Reaction Mechanisms by Electron Paramagnetic Resonance Spectroscopy. *Anal. Chem.*, 46(9):1248–1253, 1974.

[13] J. F. Barry, J. M. Schloss, E. Bauch, M. J. Turner, C. A. Hart, L. M. Pham, and R. L. Walsworth. Sensitivity optimization for NV-diamond magnetometry. *Rev. Mod. Phys.*, 92(1):015004, 2020.

[14] J. Barton, M. Gulka, J. Tarabek, Y. Mindarava, Z. Wang, J. Schimer, H. Raabova, J. Bednar, M. B. Plenio, F. Jelezko, M. Nesladek, and P. Cigler. Nanoscale dynamic readout of a chemical redox process using radicals coupled with nitrogen-vacancy centers in nanodiamonds. *ACS Nano*, 14(10):12938–12950, 2020.

[15] M. Bennati. *EPR Interactions–Hyperfine Coupling*. John Wiley & Sons, Ltd, Chichester, UK, 2017.

[16] D. Bluvstein, Z. Zhang, and A. C. B. Jayich. Identifying and Mitigating Charge Instabilities in Shallow Diamond Nitrogen-Vacancy Centers. *Phys. Rev. Lett.*, 122(7):76101, 2019.

[17] E. Bordignon. *EPR Spectroscopy of Nitroxide Spin Probes*. John Wiley & Sons, Ltd, Chichester, UK, 2017.

[18] E. Bordignon, H. Brutlach, L. Urban, K. Hideg, A. Savitsky, A. Schnegg, P. Gast, M. Engelhard, E. J. J. Groenen, K. Möbius, and H.-J. Steinhoff. Heterogeneity in the Nitroxide Micro-Environment: Polarity and Proticity Effects in Spin-Labeled Proteins Studied by Multi-Frequency EPR. *Appl. Magn. Reson.*, 37(1-4):391–403, 2010.

[19] S. Brandon, A. H. Beth, and E. J. Hustedt. The global analysis of DEER data. *Journal of Magnetic Resonance*, 218:93–104, May 2012.

[20] R. C. Bray. Sudden freezing as a technique for the study of rapid reactions. *Biochem. J.*, 81(1):189–193, 1961.

[21] D. E. Budil. CW-EPR Spectral Simulations. In *Methods in Enzymolog*, volume 563, pages 143–170. Elsevier, 2015.

[22] C.-K. Chan, Y. Hu, S. Takahashi, D. L. Rousseau, W. A. Eaton, and J. Hofrichter. Submillisecond protein folding kinetics studied by ultrarapid mixing. *Proc. Natl. Acad. Sci. U.S.A.*, 94(5):1779–1784, 1997.

[23] J. Chen, O. Y. Chen, and H. C. Chang. Relaxation of a dense ensemble of spins in diamond under a continuous microwave driving field. *Sci. Rep.*, 11:16278, 2021.

[24] A. V. Cherepanov and S. de Vries. Microsecond freeze-hyperquenching: Development of a new ultrafast micro-mixing and sampling technology and application to enzyme catalysis. *Biochim. Biophys. Acta - Bioenerg.*, 1656(1):1–31, 2004.

[25] A. Collauto, H. A. DeBerg, R. Kaufmann, W. N. Zagotta, S. Stoll, and D. Goldfarb. Rates and equilibrium constants of the ligand-induced conformational transition of an HCN ion channel protein domain determined by DEER spectroscopy. *Phys. Chem. Chem. Phys.*, 19(23):15324–15334, 2017.

[26] D. R. Davies, A. D. Gelinas, C. Zhang, J. C. Rohloff, J. D. Carter, D. O'Connell, S. M. Waugh, S. K. Wolk, W. S. Mayfield, A. B. Burgin, T. E. Edwards, L. J. Stewart, L. Gold, N. Janjic, and T. C. Jarvis. Unique motifs and hydrophobic interactions shape the binding of modified DNA ligands to protein targets. *Proc. Natl. Acad. Sci. U.S.A.*, 109(49):19971–19976, 2012.

[27] T. de Guillebon, B. Vindolet, J.-F. Roch, V. Jacques, and L. Rondin. Temperature dependence of the longitudinal spin relaxation time t_1 of single nitrogen-vacancy centers in nanodiamonds. *Phys. Rev. B*, 102(16):165427, 2020.

[28] S. de Vries. The role of the conserved tryptophan272 of the Paracoccus denitrificans cytochrome c oxidase in proton pumping. *Biochim. Biophys. Acta - Bioenerg.*, 1777(7):925–928, 2008.

[29] C. L. Degen, F. Reinhard, and P. Cappellaro. Quantum sensing. *Rev. Mod. Phys.*, 89(3):1–39, 2017.

[30] E. W. Deutsch, G. S. Omenn, Z. Sun, M. Maes, M. Pernemalm, K. K. Palaniappan, N. Letunica, Y. Vandenbrouck, V. Brun, S.-C. Tao, X. Yu, P. E. Geyer, V. Ignjatovic, R. L. Moritz, and J. M. Schwenk. Advances and Utility of the Human Plasma Proteome. *J. Proteome Res.*, 20(12):5241–5263, 2021.

[31] S. J. DeVience, L. M. Pham, I. Lovchinsky, A. O. Sushkov, N. Bar-Gill, C. Belthangady, F. Casola, M. Corbett, H. Zhang, M. Lukin, H. Park, A. Yacoby, and R. L. Walsworth. Nanoscale NMR spectroscopy and imaging of multiple nuclear species. *Nat. Nanotechnol.*, 10(2):129–134, 2015.

[32] C. Dockter, A. Volkov, C. Bauer, Y. Polyhach, Z. Joly-Lopez, G. Jeschke, and H. Paulsen. Refolding of the integral membrane protein light-harvesting complex II monitored by pulse EPR. *Proc. Natl. Acad. Sci. U.S.A.*, 106(44):18485–18490, Nov. 2009.

[33] J. Duo, C. Chiriac, R. Y. Huang, J. Mehl, G. Chen, A. Tymiak, P. Sabbatini, R. Pillutla, and Y. Zhang. Slow Off-Rate Modified Aptamer (SOMAmer) as a Novel Reagent in Immunoassay Development for Accurate Soluble Glypican-3 Quantification in Clinical Samples. *Anal. Chem.*, 90(8):5162–5170, 2018.

[34] G. R. Eaton and S. S. Eaton. Distance measurements in biological systems by epr. *Biological Magnetic Resonance*, 19:29–129, 2000.

[35] G. R. Eaton, S. S. Eaton, D. P. Barr, and R. T. Weber. Springer Vienna, 2010.

[36] T. E. Edwards, T. M. Okonogi, B. H. Robinson, and S. T. Sigurdsson. Site-Specific Incorporation of Nitroxide Spin Labels into Internal Sites of the TAR-RNA Structure Dependent Dynamics of RNA by EPR Spectroscopy. *J. Am. Chem. Soc.*, 123(7):1527–1528, 2001.

[37] T. Egawa, J. L. Durand, E. Y. Hayden, D. L. Rousseau, and S.-R. Yeh. Design and Evaluation of a Passive Alcove-Based Microfluidic Mixer. *Anal. Chem.*, 81(4):1622–1627, 2009.

[38] C. Eid, J. W. Palko, E. Katilius, and J. G. Santiago. Rapid Slow Off-Rate Modified Aptamer (SOMAmer)-Based Detection of C-Reactive Protein Using Isotachophoresis and an Ionic Spacer. *Anal. Chem.*, 87(13):6736–6743, 2015.

[39] J. P. Elskens, J. M. Elskens, and A. Madder. Chemical modification of aptamers for increased binding affinity in diagnostic applications: Current status and future prospects. *Int. J. Mol. Sci.*, 21(12):1–31, 2020.

[40] N. Fehr, I. García-Rubio, G. Jeschke, and H. Paulsen. Early folding events during light harvesting complex II assembly in vitro monitored by pulsed electron paramagnetic resonance. *Biochimica et Biophysica Acta (BBA) - Bioenergetics*, 1857(6):695–704, 2016.

[41] J. B. Feix and C. S. Klug. Site-directed spin labeling of membrane proteins and peptide membrane interactions. In L. J. Berliner, editor, *Biological magnetic resonance*, volume 14, pages 251–281. Springer US, Boston, MA, 2002.

[42] A. Finco, A. Haykal, R. Tanos, F. Fabre, S. Chouaieb, W. Akhtar, I. Robert-Philip, W. Legrand, F. Ajejas, K. Bouzehouane, N. Reyren, T. Devolder, J.-P. Adam, J.-V. Kim, V. Cros, and V. Jacques. Imaging non-collinear antiferromagnetic textures via single spin relaxometry. *Nat. Commun.*, 12(767):1–6, 2021.

[43] R. Fukuda, P. Balasubramanian, I. Higashimata, G. Koike, T. Okada, R. Kagami, T. Teraji, S. Onoda, M. Haruyama, K. Yamada, M. Inaba, H. Yamano, F. M. Stürner, S. Schmitt, L. P. McGuinness, F. Jelezko, T. Ohshima, T. Shinada, H. Kawarada, W. Kada, O. Hanaizumi, T. Tanii, and J. Isoya. Lithographically engineered shallow nitrogen-vacancy centers in diamond for external nuclear spin sensing. *New J. Phys.*, 20(8):083029, 2018.

[44] L. Fábregas Ibáñez, G. Jeschke, and S. Stoll. DeerLab: a comprehensive software package for analyzing dipolar electron paramagnetic resonance spectroscopy data. *Magn. Reson.*, 1(2):209–224, 2020.

[45] F. Fávaro de Oliveira, D. Antonov, Y. Wang, P. Neumann, S. A. Momenzadeh, T. Häußermann, A. Pasquarelli, A. Denisenko, and J. Wrachtrup. Tailoring spin defects in diamond by lattice charging. *Nat. Commun.*, 8(1):15409, 2017.

[46] A. Ganguly, K. C. Lin, S. Muthukumar, and S. Prasad. Autonomous, Real-Time Monitoring Electrochemical Aptasensor for Circadian Tracking of Cortisol Hormone in Submicroliter Volumes of Passively Eluted Human Sweat. *ACS Sens.*, 6(1):63–72, 2021.

[47] A. D. Gelinas, D. R. Davies, T. E. Edwards, J. C. Rohloff, J. D. Carter, C. Zhang, S. Gupta, Y. Ishikawa, M. Hirota, Y. Nakaishi, T. C. Jarvis, and N. Janjic. Crystal Structure of Interleukin-6 in Complex with a Modified Nucleic Acid Ligand. *J. Biol. Chem.*, 289(12):8720–8734, 2014.

[48] A. D. Gelinas, D. R. Davies, T. E. Edwards, J. C. Rohloff, J. D. Carter, C. Zhang, S. Gupta, Y. Ishikawa, M. Hirota, Y. Nakaishi, T. C. Jarvis, and N. Janjic. Crystal structure of interleukin-6 in complex with a modified nucleic acid ligand. *J. Biol. Chem.*, 289(12):8720–8734, 2014.

[49] E. R. Georgieva, A. S. Roy, V. M. Grigoryants, P. P. Borbat, K. A. Earle, C. P. Scholes, and J. H. Freed. Effect of freezing conditions on distances and their distributions derived from Double Electron Electron Resonance (DEER): A study of doubly-spin-labeled T4 lysozyme. *Journal of Magnetic Resonance*, 216:69–77, 2012.

[50] L. Gold, D. Ayers, J. Bertino, C. Bock, A. Bock, E. N. Brody, J. Carter, A. B. Dalby, B. E. Eaton, T. Fitzwater, D. Flather, A. Forbes, T. Foreman, C. Fowler, B. Gawande, M. Goss, M. Gunn, S. Gupta, D. Halladay, J. Heil, J. Heilig, B. Hicke, G. Husar, N. Janjic, T. Jarvis, S. Jennings, E. Katilius, T. R. Keeney, N. Kim, T. H. Koch, S. Kraemer, L. Kroiss, N. Le, D. Levine, W. Lindsey, B. Lollo, W. Mayfield, M. Mehan, R. Mehler, S. K. Nelson, M. Nelson, D. Nieuwlandt, M. Nikrad, U. Ochsner, R. M. Ostroff, M. Otis, T. Parker, S. Pietrasiewicz, D. I. Resnicow, J. Rohloff, G. Sanders, S. Sattin, D. Schneider, B. Singer, M. Stanton, A. Sterkel, A. Stewart, S. Stratford, J. D. Vaught, M. Vrkljan, J. J. Walker, M. Watrobka, S. Waugh, A. Weiss, S. K. Wilcox, A. Wolfson, S. K. Wolk, C. Zhang, and D. Zichi. Aptamer-based multiplexed proteomic technology for biomarker discovery. *PLoS ONE*, 5:e15004, 2010.

[51] G. Goodman and J. S. Leigh. Distance between the electron paramagnetic resonance-visible copper and cytochrome a in bovine heart cytochrome oxidase. *Biochemistry*, 24(9):2310–2317, 1985.

[52] D. B. Gophane and S. T. Sigurdsson. Hydrogen-bonding controlled rigidity of an isoindoline-derived nitroxide spin label for nucleic acids. *Chem. Commun.*, 49(10):999–1001, 2013.

[53] F. Gorrini, R. Giri, C. E. Avalos, S. Tambalo, S. Mannucci, L. Basso, N. Bazzanella, C. Dorigoni, M. Cazzanelli, P. Marzola, A. Miotello, and A. Bifone. Fast and Sensitive Detection of Paramagnetic Species Using Coupled Charge and Spin Dynamics in Strongly Fluorescent Nanodiamonds. *ACS Appl. Mater. Interfaces*, 11(27):24412–24422, 2019.

[54] S. Gupta, M. Hirota, S. M. Waugh, I. Murakami, T. Suzuki, M. Muraguchi, M. Shibamori, Y. Ishikawa, T. C. Jarvis, J. D. Carter, C. Zhang, B. Gawande, M. Vrkljan, N. Janjic, and D. J. Schneider. Chemically Modified DNA Aptamers Bind Interleukin-6 with High Affinity and Inhibit Signaling by Blocking Its Interaction with Interleukin-6 Receptor. *J. Biol. Chem.*, 289(12):8706–8719, 2014.

[55] L. T. Hall, J. H. Cole, C. D. Hill, and L. C. L. Hollenberg. Sensing of fluctuating nanoscale magnetic fields using nitrogen–vacancy centers in diamond. *Phys. Rev. Lett.*, 103(22):220802, 2009.

[56] S. Han, Y. C. Ching, and D. L. Rousseau. Time evolution of the intermediates formed in the reaction of oxygen with mixed-valence cytochrome c oxidase. *J. Am. Chem. Soc.*, 112(26):9445–9451, 1990.

[57] T. Hett, T. Zbik, S. Mukherjee, H. Matsuoka, W. Bönigk, D. Klose, C. Rouillon, N. Brenner, S. Peuker, R. Klement, H.-J. Steinhoff, H. Grubmüller, R. Seifert, O. Schiemann, and U. B. Kaupp. Spatiotemporal Resolution of Conformational Changes in Biomolecules by Combining Pulsed Electron–Electron Double Resonance Spectroscopy with Microsecond Freeze-Hyperquenching. *J. Am. Chem. Soc.*, 143(18):6981–6989, 2021.

[58] D. J. Hirsh, W. F. Beck, J. B. Innes, and G. W. Brudvig. Using Saturation-Recovery EPR to Measure Distances in Proteins: Applications to Photosystem II. *Biochemistry*, 31(2):532–541, 1992.

[59] W. Hu, B. T. Walters, Z.-Y. Kan, L. Mayne, L. E. Rosen, S. Marqusee, and S. W. Englander. Stepwise protein folding at near amino acid resolution by hydrogen exchange and mass spectrometry. *Proc. Natl. Acad. Sci. U.S.A.*, 110(19):7684–7689, May 2013.

[60] Y. Hu, Y. Wang, J. Singh, R. Sun, L. Xu, X. Niu, K. Huang, G. Bai, G. Liu, X. Zuo, C. Chen, P. Z. Qin, and X. Fang. Phosphorothioate-Based Site-Specific Labeling of Large RNAs for Structural and Dynamic Studies. *ACS Chem. Biol.*, 17(9):2448–2460, 2022.

[61] W. L. Hubbell, D. S. Cafiso, and C. Altenbach. Identifying conformational changes with site-directed spin labeling. *Nat. Struct. Mol. Biol.*, 7(9):735–739, 2000.

[62] E. Janitz, K. Herb, L. A. Völker, W. S. Huxter, C. L. Degen, and J. M. Abendroth. Diamond surface engineering for molecular sensing with nitrogen—vacancy centers. *J. Mater. Chem. C.*, 10(37):13533–13569, 2022.

[63] W. Jankowski, H. A. D. Lagassé, W. C. Chang, J. McGill, K. I. Jankowska, A. D. Gelinas, N. Janjic, and Z. E. Sauna. Modified aptamers as reagents to characterize recombinant human erythropoietin products. *Sci. Rep.*, 10(1):18593, 2020.

[64] A. Jarmola, V. M. Acosta, K. Jensen, S. Chemerisov, and D. Budker. Temperature- and Magnetic Field Dependent Longitudinal Spin Relaxation in Nitrogen Vacancy Ensembles in Diamond. *Phys. Rev. Lett.*, 108(19):197601, 2012.

[65] T. C. Jarvis, D. R. Davies, A. Hisaminato, D. I. Resnicow, S. Gupta, S. M. Waugh, A. Nagabukuro, T. Wadatsu, H. Hishigaki, B. Gawande, C. Zhang, S. K. Wolk, W. S. Mayfield, Y. Nakaishi, A. B. Burgin, L. J. Stewart, T. E. Edwards, A. D. Gelinas, D. J. Schneider, and N. Janjic. Non-helical DNA Triplex Forms a Unique Aptamer Scaffold for High Affinity Recognition of Nerve Growth Factor. *Structure*, 23(7):1293–1304, 2015.

[66] J. Jeon, K. R. Thurber, R. Ghirlando, W. M. Yau, and R. Tycko. Application of millisecond time-resolved solid state NMR to the kinetics and mechanism of melittin self-assembly. *Proc. Natl. Acad. Sci. U.S.A.*, 116(34):16717–16722, 2019.

[67] J. Jeon, W.-M. Yau, and R. Tycko. Millisecond Time-Resolved Solid-State NMR Reveals a Two-Stage Molecular Mechanism for Formation of Complexes between Calmodulin and a Target Peptide from Myosin Light Chain Kinase. *J. Am. Chem. Soc.*, 142(50):21220–21232, 2020.

[68] G. Jeschke. Deer distance measurements on proteins. *Annu. Rev. Phys. Chem.*, 63(1):419–446, 2012.

[69] H. Y. Juliusson and S. T. Sigurdsson. Reduction Resistant and Rigid Nitroxide Spin-Labels for DNA and RNA. *J. Org. Chem.*, 85(6):4036–4046, 2020.

[70] C. Jung, V. Schünemann, and F. Lendzian. Freeze-quenched iron-oxo intermediates in cytochromes P450. *Biochem. Biophys. Res. Commun.*, 338(1):355–364, 2005.

[71] T. Kálai, W. L. Hubbell, and K. Hideg. Click reactions with nitroxides. *Synthesis*, (8):1336–1340, 2009.

[72] A. Khanal, Y. Pan, L. S. Brown, and L. Konermann. Pulsed hydrogen/deuterium exchange mass spectrometry for time-resolved membrane protein folding studies: Membrane protein folding studied by pulsed HDX. *J. Mass Spectrom.*, 47(12):1620–1626, Dec. 2012.

[73] E. Kim, S. Lee, A. Jeon, J. M. Choi, H.-S. Lee, S. Hohng, and H.-S. Kim. A single-molecule dissection of ligand binding to a protein with intrinsic dynamics. *Nat. Chem. Biol.*, 9(5):313–318, 2013.

[74] S. H. Kim, R. Perera, L. P. Hager, J. H. Dawson, and B. M. Hoffman. Rapid Freeze-Quench ENDOR Study of Chloroperoxidase Compound I: The Site of the Radical. *J. Am. Chem. Soc.*, 128(17):5598–5599, 2006.

[75] L. Konermann and D. A. Simmons. Protein-folding kinetics and mechanisms studied by pulse-labeling and mass spectrometry. *Mass Spectrom. Rev.*, 22:1–26, 2003.

[76] S. Kraemer, J. D. Vaught, C. Bock, L. Gold, E. Katilius, T. R. Keeney, N. Kim, N. A. Saccomano, S. K. Wilcox, D. Zichi, and G. M. Sanders. From SOMAmer-Based Biomarker Discovery to Diagnostic and Clinical Applications: A SOMAmer-Based, Streamlined Multiplex Proteomic Assay. *PLoS ONE*, 6(10):e26332, 2011.

[77] K. Krell, B. Pfeuffer, F. Rönicke, Z. S. Chinoy, C. Favre, F. Friscourt, and H.-A. Wagenknecht. Fast and efficient postsynthetic dna labeling in cells by means of strain-promoted sydnone-alkyne cycloadditions. *Chem. Eur. J.*, page 16093–1609, 2021.

[78] S. Kucher, S. Korneev, S. Tyagi, R. Apfelbaum, D. Grohmann, E. A. Lemke, J. P. Klare, H.-J. Steinhoff, and D. Klose. Orthogonal spin labeling using click chemistry for in vitro and in vivo applications. *J. Magn. Reson.*, 275:38–45, 2017.

[79] J. Lehner and S. Stoll. Modeling of motional EPR spectra using hindered brownian rotational diffusion and the stochastic liouville equation. *J. Chem. Phys.*, 152(9):094103, 2020.

[80] C. Li, M. Chen, D. Lyzwa, and P. Cappellaro. All-Optical Quantum Sensing of Rotational Brownian Motion of Magnetic Molecules. *Nano Lett.*, 19(10):7342–7348, 2019.

[81] C. Li, R. Soleyman, M. Kohandel, and P. Cappellaro. SARS-CoV-2 Quantum Sensor Based on Nitrogen-Vacancy Centers in Diamond. *Nano Lett.*, 22(1):43–49, 2022.

[82] Y. Lin, G. J. Gerfen, D. L. Rousseau, and S.-R. Yeh. Ultrafast Microfluidic Mixer and Freeze-Quenching Device. *Anal. Chem.*, 75(20):5381–5386, 2003.

[83] I. Lovchinsky, A. O. Sushkov, E. Urbach, N. P. de Leon, S. Choi, K. De Greve, R. Evans, R. Gertner, E. Bersin, C. Müller, L. McGuinness, F. Jelezko, R. L. Walsworth, H. Park, and M. D. Lukin. Nuclear magnetic resonance detection and spectroscopy of single proteins using quantum logic. *Science*, 351(6275):836–841, 2016.

[84] J. Manzerova, V. Krymov, and G. J. Gerfen. Investigating the intermediates in the reaction of ribonucleoside triphosphate reductase from Lactobacillus leichmannii: An application of HF EPR-RFQ technology. *J. Magn. Reson.*, 213(1):32–45, 2011.

[85] D. Margraf, P. Cekan, T. F. Prisner, S. T. Sigurdsson, and O. Schiemann. Ferro- and antiferromagnetic exchange coupling constants in PELDOR spectra. *Phys. Chem. Chem. Phys.*, 11(31):6708–6714, 2009.

[86] A. Marko, D. Margraf, P. Cekan, S. T. Sigurdsson, O. Schiemann, and T. F. Prisner. Analytical method to determine the orientation of rigid spin labels in DNA. *Phys. Rev. E*, 81(2):021911, 2010.

[87] B. S. Miller, L. Bezinge, H. D. Gliddon, D. Huang, G. Dold, E. R. Gray, J. Heaney, P. J. Dobson, E. Nastouli, J. J. Morton, and R. A. McKendry. Spin-enhanced nanodiamond biosensing for ultrasensitive diagnostics. *Nature*, 587(7835):588–593, 2020.

[88] D. M. Miller, J. S. Olson, J. W. Pflugrath, and F. A. Quiocho. Rates of ligand binding to periplasmic proteins involved in bacterial transport and chemotaxis. *J. Biol. Chem.*, 258(22):13665–13672, 1983.

[89] T. R. Miller, S. C. Alley, A. W. Reese, M. S. Solomon, W. V. McCallister, C. Mailer, B. H. Robinson, and P. B. Hopkins. A Probe for Sequence-Dependent Nucleic Acid Dynamics. *J. Am. Chem. Soc.*, 117(36):9377–9378, 1995.

[90] S. Mitic, J. W. van Nieuwkasteele, A. van den Berg, and S. de Vries. Design of turbulent tangential micro-mixers that mix liquids on the nanosecond time scale. *Anal. Biochem.*, 469:19–26, 2015.

[91] N. Mizuochi, P. Neumann, F. Rempp, J. Beck, V. Jacques, P. Siyushev, K. Nakamura, D. J. Twitchen, H. Watanabe, S. Yamasaki, F. Jelezko, and J. Wrachtrup. Coherence of single spins coupled to a nuclear spin bath of varying density. *Phys. Rev. B*, 80(4):041201, 2009.

[92] M. Mrózek, D. Rudnicki, P. Kehayias, A. Jarmola, D. Budker, and W. Gawlik. Longitudinal spin relaxation in nitrogen-vacancy ensembles in diamond. *EPJ Quantum Technol.*, 2(1), 2015.

[93] B. A. Myers, A. Das, M. C. Dartiailh, K. Ohno, D. D. Awschalom, and A. C. Bleszynski Jayich. Probing surface noise with depth-calibrated spins in diamond. *Phys. Rev. Lett.*, 113:027602, 2014.

[94] F. Nami, P. Gast, and E. J. Groenen. Rapid Freeze-Quench EPR Spectroscopy: Improved Collection of Frozen Particles. *Appl. Magn. Reson.*, 47(6):643–653, 2016.

[95] P. Nguyen, X. Shi, S. T. Sigurdsson, D. Herschlag, and P. Z. Qin. A single-stranded junction modulates nanosecond motional ordering of the substrate recognition duplex of a group i ribozyme. *ChemBioChem*, 14(14):1720–1723, 2013.

[96] E. G. Panarelli, H. van der Meer, P. Gast, and E. J. Groenen. Effective coupling of rapid freeze-quench to high-frequency electron paramagnetic resonance. *PLoS ONE*, 15(5):1–10, 2020.

[97] A. Paulus, C. Werner, B. Ludwig, and S. de Vries. The cytochrome ba3 oxidase from Thermus thermophilus does not generate a tryptophan radical during turnover: Implications for the mechanism of proton pumping. *Biochim. Biophys. Acta - Bioenerg.*, 1847(10):1093–1100, 2015.

[98] F. Perona Martínez, A. C. Nusantara, M. Chipaux, S. K. Padamati, and R. Schirhagl. Nanodiamond Relaxometry-Based Detection of Free-Radical Species When Produced in Chemical Reactions in Biologically Relevant Conditions. *ACS Sens.*, 5(12):3862–3869, 2020.

[99] L. M. Pham, S. J. DeVience, F. Casola, I. Lovchinsky, A. O. Sushkov, E. Bersin, J. Lee, E. Urbach, P. Cappellaro, H. Park, A. Yacoby, M. Lukin, and R. L. Walsworth. NMR technique for determining the depth of shallow nitrogen-vacancy centers in diamond. *Phys. Rev. B*, 93(4):045425, 2016.

[100] R. Pievo, B. Angerstein, A. J. Fielding, C. Koch, I. Feussner, and M. Bennati. A rapid freeze-quench setup for multi-frequency EPR spectroscopy of enzymatic reactions. *ChemPhysChem*, 14(18):4094–4101, 2013.

[101] C. F. Polnaszek, G. V. Bruno, and J. H. Freed. ESR line shapes in the slow-motional region: Anisotropic liquids. *J. Chem. Phys*, 58(8):3185–3199, 1973.

[102] A. Potapov and D. Goldfarb. A Calibration Reaction for Rapid Freeze-Quench W-Band EPR. *Appl. Magn. Reson.*, 37(1):845, 2009.

[103] T. F. Prisner. Shaping EPR: Phase and amplitude modulated microwave pulses. *J. Magn. Reson.*, 306:98–101, 2019.

[104] P. Z. Qin, S. E. Butcher, J. Feigon, and W. L. Hubbell. Quantitative analysis of the isolated GAAA tetraloop/receptor interaction in solution: A site-directed spin labeling study. *Biochemistry*, 40(23):6929–6936, 2001.

[105] P. Regenfuss, R. M. Clegg, M. J. Fulwyler, F. J. Barrantes, and T. M. Jovin. Mixing liquids in microseconds. *Rev. Sci. Instrum.*, 56(2):283–290, 1985.

[106] X. Ren, A. D. Gelinas, I. von Carlowitz, N. Janjic, and A. M. Pyle. Structural basis for IL-1α recognition by a modified DNA aptamer that specifically inhibits IL-1α signaling. *Nat. Commun.*, 8(1):810, 2017.

[107] T. Rosskopf, A. Dussaux, K. Ohashi, M. Loretz, R. Schirhagl, H. Watanabe, S. Shikata, K. M. Itoh, and C. L. Degen. Investigation of surface magnetic noise by shallow spins in diamond. *Phys. Rev. Lett.*, 112:147602, 2014.

[108] R. Rutter, L. P. Hager, H. Dhonau, M. Hendrich, M. Valentine, and P. Debrunner. Chloroperoxidase compound I: electron paramagnetic resonance and Moessbauer studies. *Biochemistry*, 23(26):6809–6816, 1984.

[109] S. Sangtawesin, B. L. Dwyer, S. Srinivasan, J. J. Allred, L. V. H. Rodgers, K. De Greve, A. Stacey, N. Dontschuk, K. M. O'Donnell, D. Hu, D. A. Evans, C. Jaye, D. A. Fischer, M. L. Markham, D. J. Twitchen, H. Park, M. D. Lukin, and N. P. de Leon. Origins of Diamond Surface Noise Probed by Correlating Single-Spin Measurements with Surface Spectroscopy. *Phys. Rev. X*, 9(3):031052, 2019.

[110] O. Schiemann, C. A. Heubach, D. Abdullin, K. Ackermann, M. Azarkh, E. G. Bagryanskaya, M. Drescher, B. Endeward, J. H. Freed, L. Galazzo, D. Goldfarb, T. Hett, L. Esteban Hofer, L. Fábregas Ibáñez, E. J. Hustedt, S. Kucher, I. Kuprov, J. E. Lovett, A. Meyer, S. Ruthstein, S. Saxena, S. Stoll, C. R. Timmel, M. Di Valentin, H. S. Mchaourab, T. F. Prisner, B. E. Bode, E. Bordignon, M. Bennati, and G. Jeschke. Benchmark test and guidelines for DEER/PELDOR experiments on nitroxide-labeled biomolecules. *J. Am. Chem. Soc.*, 143(43):17875–17890, 2021.

[111] B. Schmidt, G. Mahmud, S. Soh, S. H. Kim, T. Page, T. V. O'Halloran, B. A. Grzybowski, and B. M. Hoffman. Design, Implementation, Simulation, and Visualization of a Highly Efficient RIM Microfluidic Mixer for Rapid Freeze-Quench of Biological Samples. *Appl. Magn. Reson.*, 40(4):415–425, 2011.

[112] T. Schmidt and G. M. Clore. T m filtering by 1H-methyl labeling in a deuterated protein for pulsed double electron–electron resonance EPR. *Chem. Commun.*, 56(74):10890–10893, 2020.

[113] T. Schmidt, J. Jeon, Y. Okuno, S. C. Chiliveri, and G. M. Clore. Submillisecond Freezing Permits Cryoprotectant-Free EPR Double Electron–Electron Resonance Spectroscopy. *ChemPhysChem*, 21(12):1224–1229, 2020.

[114] T. Schmidt, D. Wang, J. Jeon, C. D. Schwieters, and G. M. Clore. Quantitative Agreement between Conformational Substates of Holo Calcium-Loaded Calmodulin Detected by Double Electron–Electron Resonance EPR and Predicted by Molecular Dynamics Simulations. *J. Am. Chem. Soc.*, 144(27):12043–12051, 2022.

[115] D. J. Schneider and J. H. Freed. Calculating Slow Motional Magnetic Resonance Spectra. In L. Berliner and J. Reuben, editors, *Spin Labeling: Theory and Applications*, volume 8, pages 1–76. Springer US, Boston, MA, 1989.

[116] A. L. Schroeter, H. Yang, C. D. James, B. M. Hoffman, and P. E. Doan. A New Reaction for Improved Calibration of EPR Rapid-Freeze Quench Times: Kinetics of Ethylene Diamine Tetraacetate (EDTA) Transfer from Calcium(II) to Copper(II). *Appl. Magn. Reson.*, 53(7-9):1195–1210, 2022.

[117] R. N. Schwartz, L. L. Jones, and M. K. Bowman. Electron spin echo studies of nitroxide free radicals in liquids. *J. Phys. Chem.*, 83(26):3429–3434, 1979.

[118] B. Senf, W. H. Yeo, and J. H. Kim. Recent Advances in Portable Biosensors for Biomarker Detection in Body Fluids. *Biosensors*, 10:127, 2020.

[119] S. A. Shelke and S. T. Sigurdsson. Site-Directed Spin Labelling of Nucleic Acids. *Eur. J. Org. Chem.*, 2012(12):2291–2301, 2012.

[120] F. Shi, F. Kong, P. Zhao, X. Zhang, M. Chen, S. Chen, Q. Zhang, M. Wang, X. Ye, Z. Wang, Z. Qin, X. Rong, J. Su, P. Wang, P. Z. Qin, and J. Du. Single-DNA electron spin resonance spectroscopy in aqueous solutions. *Nat. Methods*, 15(9):697–699, 2018.

[121] F. Shi, Q. Zhang, P. Wang, H. Sun, J. Wang, X. Rong, M. Chen, C. Ju, F. Reinhard, H. Chen, J. Wrachtrup, J. Wang, and J. Du. Single-protein spin resonance spectroscopy under ambient conditions. *Science*, 347(6226):1135–1138, 2015.

[122] A. Sigaeva, H. Shirzad, F. Perona Martinez, A. C. Nusantara, N. Mougios, M. Chipaux, and R. Schirhagl. Diamond-based nanoscale quantum relaxometry for sensing free radical production in cells. *Small*, 18:2105750–2105762, 2022.

[123] N. K. Singh, P. Jain, S. Das, and P. Goswami. Dye Coupled Aptamer-Captured Enzyme Catalyzed Reaction for Detection of Pan Malaria and P. falciparum Species in Laboratory Settings and Instrument-Free Paper-Based Platform. *Anal. Chem.*, 91(6):4213–4221, 2019.

[124] A. Solano-Peralta, J. P. Saucedo-Vázquez, R. Escudero, H. Höpfl, H. El-Mkami, G. M. Smith, and M. E. Sosa-Torres. Magnetic and high-frequency EPR studies of an octahedral Fe(III) compound with unusual zero-field splitting parameters. *Dalton Trans.*, (9):1668–1674, 2009.

[125] P. E. Spindler, P. Schöps, A. M. Bowen, B. Endeward, and T. Prisner. *EPR Interactions–Hyperfine Coupling*. John Wiley & Sons, Ltd, Chichester, UK, 2017.

[126] P. E. Spindler, P. Schöps, W. Kallies, S. J. Glaser, and T. F. Prisner. Perspectives of shaped pulses for EPR spectroscopy. *J. Magn. Reson.*, 280:30–45, 2017.

[127] T. Spolitak, J. H. Dawson, and D. P. Ballou. Rapid kinetics investigations of peracid oxidation of ferric cytochrome P450cam: Nature and possible function of compound ES. *J. Inorg. Biochem.*, 100(12):2034–2044, 2006.

[128] J. C. Spurlino, G. Y. Lu, and F. A. Quiocho. The 2.3-A resolution structure of the maltose- or maltodextrin-binding protein, a primary receptor of bacterial active transport and chemotaxis. *J. Biol. Chem.*, 266(8):5202–5219, 1991.

[129] B. Srour, M. J. Strampraad, W. R. Hagen, and P. L. Hagedoorn. Refolding kinetics of cytochrome c studied with microsecond timescale continuous-flow UV–vis spectroscopy and rapid freeze-quench EPR. *J. Inorg. Biochem.*, 184(March):42–49, 2018.

[130] S. Steinert, F. Ziem, L. T. Hall, A. Zappe, M. Schweikert, N. Götz, A. Aird, G. Balasubramanian, L. Hollenberg, and J. Wrachtrup. Magnetic spin imaging under ambient conditions with sub-cellular resolution. *Nat. Commun.*, 4(1):1607, 2013.

[131] S. Stoll, Y. NejatyJahromy, J. J. Woodward, A. Ozarowski, M. A. Marletta, and R. D. Britt. Nitric Oxide Synthase Stabilizes the Tetrahydrobiopterin Cofactor Radical by Controlling Its Protonation State. *J. Am. Chem. Soc.*, 132(33):11812–11823, 2010.

[132] S. Stoll and A. Schweiger. EasySpin, a comprehensive software package for spectral simulation and analysis in EPR. *J. Magn. Reson.*, 178(1):42–55, 2006.

[133] K. L. Stone, R. K. Behan, and M. T. Green. X-ray absorption spectroscopy of chloroperoxidase compound i: Insight into the reactive intermediate of p450 chemistry. *Proc. Natl. Acad. Sci. U.S.A.*, 102(46):16563–16565, 2005.

[134] A. O. Sushkov, I. Lovchinsky, N. Chisholm, R. L. Walsworth, H. Park, and M. D. Lukin. Magnetic resonance detection of individual proton spins using quantum reporters. *Phys. Rev. Lett.*, 113(19):1–5, 2014.

[135] S. Takahashi, Y.-c. Ching, J. Wang, and D. L. Rousseau. Microsecond Generation of Oxygen-bound Cytochrome c Oxidase by Rapid Solution Mixing. *J. Biol. Chem.*, 270(15):8405–8407, 1995.

[136] M. Tanaka, K. Matsuura, S. Yoshioka, S. Takahashi, K. Ishimori, H. Hori, and I. Morishima. Activation of Hydrogen Peroxide in Horseradish Peroxidase Occurs within ~200 μs Observed by a New Freeze-Quench Device. *Biophys. J.*, 84(3):1998–2004, 2003.

[137] C. Tang, C. D. Schwieters, and G. M. Clore. Open-to-closed transition in apo maltose-binding protein observed by paramagnetic NMR. *Nature*, 449(7165):1078–1082, 2007.

[138] M. H. Tessmer, E. R. Canarie, and S. Stoll. Comparative evaluation of spin-label modeling methods for protein structural studies. *Biophys. J.*, 121(18):3508–3519, 2022.

[139] M. H. Tessmer and S. Stoll. chiLife: An open-source Python package for in silico spin labeling and integrative protein modeling. *PLoS Comput. Biol.*, 19(3):e1010834, 2023.

[140] J. P. Tetienne, T. Hingant, L. Rondin, A. Cavaillès, L. Mayer, G. Dantelle, T. Gacoin, J. Wrachtrup, J. F. Roch, and V. Jacques. Spin relaxometry of single nitrogen-vacancy defects in diamond nanocrystals for magnetic noise sensing. *Phys. Rev. B*, 87(23):235436, 2013.

[141] A.-L. Tsai, V. Berka, R. J. Kulmacz, G. Wu, and G. Palmer. An Improved Sample Packing Device for Rapid Freeze-Trap Electron Paramagnetic Resonance Spectroscopy Kinetic Measurements. *Anal. Biochem.*, 264(2):165–171, 1998.

[142] Y. Wang, V. Kathiresan, Y. Chen, Y. Hu, W. Jiang, G. Bai, G. Liu, P. Z. Qin, and X. Fang. Posttranscriptional site-directed spin labeling of large RNAs with an unnatural base pair system under non-denaturing conditions. *Chem. Sci.*, 11(35):9655–9664, 2020.

[143] J. A. Weil and J. R. Bolton. *Electron Paramagnetic Resonance - Elementary Theory and Practical Application.* John Wiley & Sons, Ltd, 1995.

[144] F. G. Wiertz, O. M. H. Richter, A. V. Cherepanov, F. MacMillan, B. Ludwig, and S. de Vries. An oxo-ferryl tryptophan radical catalytic intermediate in cytochrome c and quinol oxidases trapped by microsecond freeze-hyperquenching (MHQ). *FEBS Lett.*, 575(1-3):127–130, 2004.

[145] F. G. M. Wiertz, O.-M. H. Richter, B. Ludwig, and S. d. Vries. Kinetic Resolution of a Tryptophan-radical Intermediate in the Reaction Cycle of Paracoccus denitrificans Cytochrome c Oxidase *. *J. Biol. Chem.*, 282(43):31580–31591, 2007.

[146] M.-L. Winz, E. C. Linder, T. André, J. Becker, and A. Jäschke. Nucleotidyl transferase assisted DNA labeling with different click chemistries. *Nucleic Acids Res.*, page e110, 2015.

[147] S. G. Worswick, J. A. Spencer, G. Jeschke, and I. Kuprov. Deep neural network processing of DEER data. *Sci. Adv.*, 4(8):eaat5218, Aug. 2018.

[148] M. Xie, X. Yu, L. V. H. Rodgers, D. Xu, I. Chi-Durán, A. Toros, N. Quack, N. P. de Leon, and P. C. Maurer. Biocompatible surface functionalization architecture for a diamond quantum sensor. *Proc. Natl. Acad. Sci. U.S.A.*, 119:e2114186119, 2022.

[149] X. Xu, C. Zhang, D. T. Denton, D. O'Connell, D. W. Drolet, and B. V. Geisbrecht. Inhibition of the Complement Alternative Pathway by Chemically Modified DNA Aptamers That Bind with Picomolar Affinity to Factor B. *J. Immunol.*, 206(4):861–873, 2021.

[150] M. A. Yu, T. Egawa, S.-R. Yeh, D. L. Rousseau, and G. J. Gerfen. EPR characterization of ascorbyl and sulfur dioxide anion radicals trapped during the reaction of bovine Cytochrome c Oxidase with molecular oxygen. *J. Magn. Reson.*, 203(2):213–219, 2010.

[151] T. Zhang, G. Pramanik, K. Zhang, M. Gulka, L. Wang, J. Jing, F. Xu, Z. Li, Q. Wei, P. Cigler, and Z. Chu. Toward Quantitative Bio-sensing with Nitrogen-Vacancy Center in Diamond. *ACS Sens.*, 6(6):2077–2107, 2021.

[152] W. Zhong, F. Edfors, A. Gummesson, G. Bergström, L. Fagerberg, and M. Uhlén. Next generation plasma proteome profiling to monitor health and disease. *Nat. Commun.*, 12:2493, 2021.

[153] F. C. Ziem, N. S. Götz, A. Zappe, S. Steinert, and J. Wrachtrup. Highly Sensitive Detection of Physiological Spins in a Microfluidic Device. *Nano Lett.*, 13(9):4093–4098, 2013.